



UNIVERSITÀ DEGLI STUDI DI NAPOLI FEDERICO II

Facoltà di Scienze Matematiche, Fisiche e Naturali

PHD THESIS IN FUNDAMENTAL AND APPLIED PHYSICS

Lithium Niobate: optical properties and applications

Supervisors

Ch.mo Prof. Pasqualino Maddalena

Dott. Pietro Ferraro

PhD Candidate

Francesco Merola

PhD cycle XXII

PhD Coordinator

Ch.mo Prof. Lorenzo Marrucci

December 2009

Index

Introduction.....	1
Chapter I : Lithium Niobate and its optical properties.....	5
Summary.....	5
1. General properties of lithium niobate.....	5
1.1 <i>Introduction</i>	5
1.2 <i>Structure and crystal growth</i>	6
1.3 <i>Optical properties</i>	9
2. Nonlinear optics.....	12
2.1 <i>The dielectric susceptibility</i>	12
2.2 <i>Second harmonic generation (SHG)</i>	17
3. Measurement of the LN nonlinear coefficients.....	21
3.1 <i>Maker's fringes technique</i>	21
3.2 <i>Experimental methods and results</i>	23
Conclusions.....	29
References.....	30
Chapter II : Super-resolution in digital holography.....	33
Summary.....	33
1. Interferometric digital holography.....	34
1.1 <i>From classical to digital holography</i>	34
1.2 <i>Theory and principle of operation of digital holography</i>	36
1.3 <i>Reconstruction methods</i>	39

1.4 <i>Digital holographic microscopy (DHM)</i>	42
2. Super-resolution in digital holographic microscopy.....	46
2.1 <i>Introduction</i>	46
2.2 <i>The experimental set-up and the diffraction grating</i>	50
2.3 <i>Registration of spatially multiplexed digital holograms</i>	53
2.4 <i>Numerical reconstruction of the multiplexed digital holograms</i>	55
2.5 <i>Experimental results demonstrating the achieved super-resolution</i>	57
2.6 <i>Influence of the diffraction efficiency flexibility on super-resolved images</i>	64
Conclusions.....	66
References.....	68
Chapter III : Solitonic waveguides in lithium niobate	71
Summary.....	71
1. Optical waveguides.....	71
2. Photorefractive soliton formation in a lithium niobate crystal.....	76
2.1 <i>Introduction: what is a soliton?</i>	76
2.2 <i>Experimental set-up and procedures</i>	81
2.3 <i>Steady-state features of the soliton formation process</i>	84
2.4 <i>Temporal evolution</i>	94
2.5 <i>Long time behaviour of the induced refractive index perturbation</i>	98
Conclusions.....	101
References.....	102
Chapter IV : Self-formation of PDMS microlens arrays on lithium niobate substrates	107
Summary.....	107
1. Introduction to microlenses.....	108
2. Fabrication of the samples.....	111
2.1 <i>Photolithography and electric field poling</i>	111

2.2 <i>Microlenses' formation</i>	114
3. <i>Microlenses' characterization by digital holography</i>	121
Conclusions.....	126
Appendix - <i>Periodic electric field poling</i>	126
References.....	130
General conclusions.....	135
List of abbreviations.....	139
Acknowledgements.....	141

Introduction

Lithium niobate (LiNbO_3 or LN) is one of the most widely used nonlinear materials in different fields of optics and optoelectronics, having as key properties large nonlinear and electro-optic coefficients, as well as pyroelectric, photorefractive, piezoelectric, acoustic and acousto-optic ones. This richness of large-magnitude physical effects has caused lithium niobate to become of considerable interest for applications such as acoustic wave devices, electro-optic modulators in telecommunications, Q-switching devices for lasers, second-harmonic generators, beam deflectors, memory elements, holographic data processing devices, sensors and more in general integrated optical devices. It is also an excellent material for manufacture of optical waveguides.

This thesis is focused on the study of the material, specially from an optical point of view, and on several novel applications arising from the exploitation of some of the properties mentioned above. In particular, the nonlinear, photorefractive and electro-optic properties are exploited for the fabrication of solitonic waveguides inside the medium and to enhance image resolution in digital holographic microscopy by means of a lithium niobate diffraction grating, whereas the pyroelectric effect is utilized for the formation of polymeric microlenses on a micro-patterned lithium niobate substrate.

The experimental measurements have been carried out at the “Istituto Nazionale di Ottica Applicata” (INOA) of the CNR, section of Pozzuoli (NA), with the group led by Dr. Pietro Ferraro, and in the “Laboratorio di Ottica dei Materiali” at the Physics Department of Naples under the guide of Prof. Pasqualino Maddalena.

Some of the obtained results have yielded the publication of articles in international journals, cited in the references at the end of each chapter.

The thesis is divided in four chapters.

In **Chapter I** some general information about lithium niobate are firstly given, describing its main properties, in particular the optical ones. Then second harmonic generation (SHG) is proposed as a technique to investigate the non-linearity of the medium. It is a typical nonlinear phenomenon: when an optical beam of frequency ω passes through a nonlinear medium, part of the radiation is converted into a radiation of frequency 2ω (i.e. with halved wavelength). This technique has the peculiarity of being non-invasive even allowing the study of the bulk of the material, thanks to the high penetration length of the optical radiation, and to possess high spatial resolution.

The study is exploited by means of the Maker's fringes technique, that allows one to obtain the non-null coefficients of the second order susceptibility tensor, characterizing in this way the material from a nonlinear point of view.

This non-linear analysis has been performed in order to complete the characterization of the material started by the group of Pozzuoli, that has studied and used lithium niobate for several years. Moreover, the nonlinear coefficients are closely related to the electro-optic ones and the electro-optic effect is largely used in the applications of the material discussed in the other chapters.

Chapter II describes a relevant experimental technique adopted for the studies described in this and in the sequent chapters: Digital Holography (DH). This is an interferometric technique that permits, starting from a digitally recorded interference fringe pattern, to numerically reconstruct the whole complex wavefield propagating through the sample under test. Digital holography is a flexible technique for the reconstruction of wavefronts, as it makes possible for example to compensate for aberrations by means of processes that are completely numerical.

In this chapter a short essay on the principle of operation and on the many applications of this technique is given, such as microscopic imaging and enhancement of resolution (“super-resolution”). In particular, a lithium niobate diffracting grating exploiting the electro-optic effect is suggested with the aim to get super-resolution in digital holographic microscopy. In fact, by means of a flexible hexagonal phase grating, it is possible to increase the numerical aperture of the imaging system, thus improving the spatial resolution of the images in two dimensions.

In **Chapter III** an overview about optical waveguides properties, techniques of fabrication and materials used is given. Then, taking advantage of the photorefractive and electro-optic qualities of lithium niobate, a particular technique used to generate an optical waveguide inside this material is presented. In this case the waveguide is self-written, thanks to the photorefractive effect, by means of a spatial photorefractive soliton, a self-reinforcing wave propagating inside the medium with constant diameter.

The guide is subsequently characterized both during its formation and after the end of the writing process by digital holography, the amplitude and phase of the soliton beam being recovered at the exit face of the crystal.

With respect to other fabrication techniques, many advantages can be identified in this case, making soliton waveguides very attractive for applications. First, the guiding structure can be written everywhere in the volume of the host material, giving a perfect 3-D structure. Second, the waveguide is symmetrical, allowing always at least one mode to propagate inside it, with very low propagation losses, being the refractive index profile self-written by a non-diffracting light beam. Third, solitons can live for long time after the end of the writing procedure, even without using any fixing technique, and the writing technology is very simple and low costly (the writing beam should have powers of the order of μW or mW).

Chapter IV describes, after a brief introduction about microlenses, how an opportunely functionalized polar dielectric lithium niobate crystal can be

suitable for the fabrication of an array of solid micrometric polymeric lenses. The fabrication process is obtained through the self-arrangement of a thin Polydimethylsiloxane (PDMS) liquid film onto a lithium niobate substrate; this process is based on the here called “Pyro-Electro-Wetting” (PEW) mechanism. In the experiment discussed in this chapter a LiNbO_3 z-cut wafer is micro-engineered with periodically poled ferroelectric domains by means of photolithographic and electric field poling processes, with the aim to provide a substrate for the fabrication process based on self-patterning of a Polydimethylsiloxane microlens array induced by thermal stimulus. Furthermore, a microscope interference method based on digital holography is adopted for microlenses’ characterization.

Chapter I

Lithium Niobate and its optical properties

Summary

In this chapter some general information about lithium niobate (LN) will be firstly given, describing its main properties, both chemical and physical. Then I will focus on the optical properties, in particular the nonlinear ones. There will be an outline on nonlinear optics in general and on the phenomenon of second harmonic generation (SHG), that is proposed as a technique to investigate the non-linearity of the medium. This study is exploited by means of the Maker's fringe technique, that allows one to obtain the non-null coefficients of the second order susceptibility tensor, characterizing in this way the material from a nonlinear point of view.

1. General properties of lithium niobate

1.1 Introduction

Lithium niobate (LN) - stoichiometric formula LiNbO_3 - is a compound of niobium, lithium and oxygen. It is a dielectric material, insoluble in water, and does not exist in nature (is a human-made compound). Its melting point is 1257°C and its density is 4.65 g/cm^3 .

LN was first discovered to be ferroelectric in 1949 [1] and it is now one of the most widely used nonlinear materials. In fact, it is characterized by large pyroelectric, piezoelectric, nonlinear and electro-optic (EO) coefficients and has also useful acoustic and acousto-optic properties. This richness of large-magnitude physical effects has caused LN to become widely used in applications such as acoustic wave devices, optical amplitude modulators, Q-switching devices for lasers, second-harmonic generators, beam deflectors, memory elements, holographic data processing devices and others [2]. It is also an excellent material for manufacture of optical waveguides, as it will be seen in Chapter III.

1.2 Structure and crystal growth

LN has a trigonal crystal system belonging to the $3m$ (C_{3v}) crystallographic point group (Fig.1), and lacks inversion symmetry. It consists of planar sheets of oxygen atoms in a distorted hexagonal close-packed configuration [3].

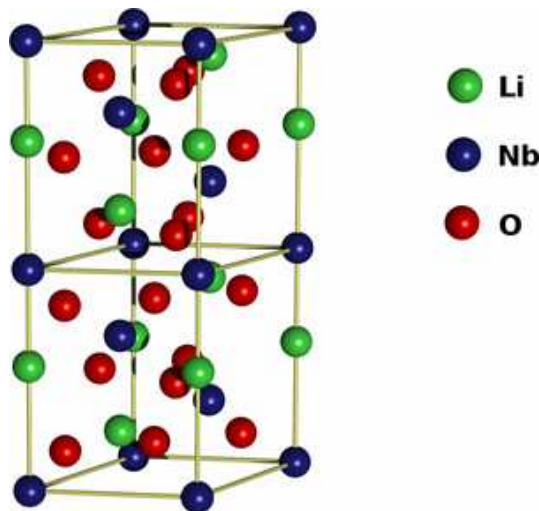


Fig. 1: Geometrical structure of lithium niobate.

Above the Curie temperature T_c (around 1210 °C) the phase is paraelectric (no spontaneous polarization) while in the ferroelectric phase below T_c LN exhibits spontaneous polarization. In the paraelectric phase Li atoms lie in an oxygen layer that is $c/4$ away from the Nb atom, while Nb atoms are centred between oxygen layers.

Conversely, in the ferroelectric phase the elastic forces of the crystal become dominant and force lithium and niobium ions into new positions.

Fig. 2 shows the conventional hexagonal unit cell for LN, where the c axis is defined as the axis about which the crystal exhibits three-fold rotation symmetry [3]. The three equivalent a axes (a_1, a_2, a_3) of the conventional hexagonal unit cell are 120° apart, lie in a plane normal to the c axis and are chosen to be perpendicular to the mirror planes of symmetry [3].

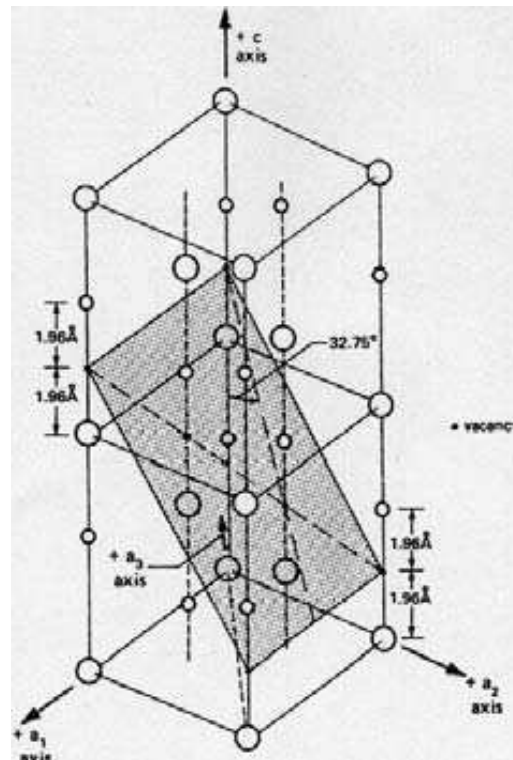


Fig. 2: Schematic view of the hexagonal unit cell of LiNbO_3 showing the hexagonal axes (c, a_1, a_2, a_3), where the large circles are Nb ions and small circles are Li atoms.

The ferroelectric dipole axis is aligned along the c axis, resulting in a $c+$ and a $c-$ face, both of which are normal to the c axis. The $c+$ face corresponds to the positive end of the dipole which becomes negative upon compression. This is due to the free charges that deposit on the c faces to compensate for the spontaneous polarization, so that negative charges deposit on the $c+$ face and positive charges on the $c-$ face.

A Cartesian coordinate system (x,y,z) is used to describe the physical properties of LN. Conventionally, the z axis is chosen to be parallel to the c axis, while the x axis is chosen to be parallel to one of the equivalent a axes. The y axis is then chosen so that a right handed system is formed, resulting in the y axis lying in one of the mirror symmetry planes (see Fig.2).

LN was first grown in the early 1960s using the Czochralski technique [4,5]. The pure compound of the material to be grown is melted in a crucible in the growth station and a seed crystal suspended from a rotating seed rod is lowered into a furnace cavity. Growth of a crystal can be initiated by starting to slowly withdraw the seed rod so that new crystal material attaches to the solid seed. The composition of a given crystal depends on the proportions used in the starting materials. For example, the congruent composition contains 48.45 %mol of Li_2O and 51.55 %mol of Nb_2O_5 [6].

Differences between stoichiometric and congruent composition LN are apparent at the unit cell level [7]. In stoichiometric LN (SLN), with $T = 1470$ K, the Li atom site is 100% occupied by Li and the Nb site is 100% occupied by Nb, as the O site is 100% occupied by O [7]. A SLN composition can be obtained by using a lithium rich melt or by adding K_2O during the growth process. Anyway, the growth of defect-free SLN crystals is quite difficult. Both mechanical twinning [8] and lithium excess micro-clusters are possible due to the composition variation in the melt-crystal interface during the growth of off-congruent LN crystals.

However, there is not enough experimental evidence that gives a thorough understanding of such defects. Lithium excess micro-clusters are generated

during the crystallization process. They are commonly present in a limited area close to the interface and come from the bottom of the crucible from which they are transported by natural convection currents. The clusters force the formation of lithium aggregates in the crystal lattice, generating micro-regions with a different lattice structure.

1.3 Optical properties

LN is classified as a negative uniaxial crystal, having two different refractive indices for ordinary and extraordinary polarized light, n_o and n_e respectively, with $n_e < n_o$, which depend slightly on the stoichiometry of the crystal and on temperature [9,10]. Tab.1 shows the refractive index values of congruent LN crystals measured at room temperature for 1064 and 532 nm radiation.

nm	n_o	n_e
1064	2.23	2.16
532	2.32	2.23

Tab.1: Refractive index values of congruent LN [9].

LN is transparent to wavelengths from around 350 nm to about 5.5 μm [11], as shown in Fig. 3, and has a bandgap of approximately 4 eV.

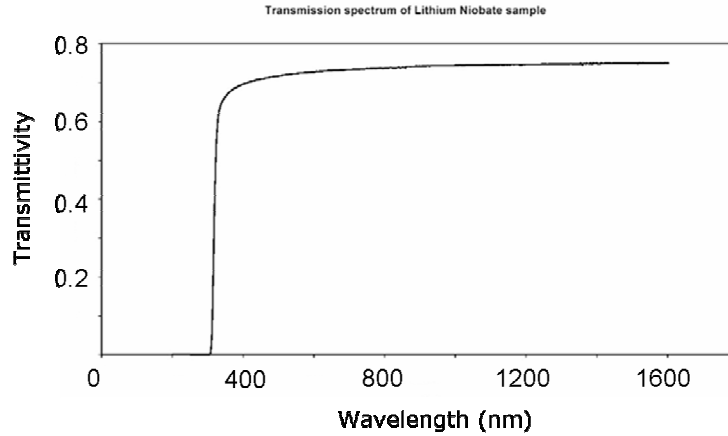


Fig. 3: Typical transmission spectrum of congruent LN [12].

It can be doped by magnesium oxide, which increases its resistance to optical damage (also known as photorefractive damage) when doped above the optical damage threshold. Other available dopants are Fe, Zn, Hf, Cu, Gd, Er, Y, Mn and B, creating optical sources that can be modulated by traveling-wave waveguide modulators.

As said above, LN is an electro-optic crystal. Linear EO effect, also known as *Pockels effect*, is a linear change in the refractive index ellipsoid induced by an applied electric field. This change is produced by the first power of the field, differently from the quadratic (or *Kerr*) EO effect. The change in the refractive index ellipsoid can be expressed as

$$\Delta\left(\frac{1}{n^2}\right)_{ij} = \sum_k r_{ijk} E_k \quad (1)$$

where E_k are the components of the electric field and r represents the EO tensor, whose nonzero independent elements are determined by the material symmetry. For example, in the case of LN, the extraordinary index change derived from (1) when the electric field is applied along the crystal symmetry axis (z -axis), is

$$\Delta n_e = -\frac{1}{2}n_e^3 r_{33} E_3 \quad (2)$$

where “3” represents the z-axis.

The structure of the EO tensor for LN is given below:

$$r_{ij} = \begin{pmatrix} 0 & -r_{22} & r_{13} \\ 0 & r_{22} & r_{13} \\ 0 & 0 & r_{33} \\ 0 & r_{42} & 0 \\ r_{42} & 0 & 0 \\ -r_{22} & 0 & 0 \end{pmatrix} \quad (3)$$

The non-vanishing EO tensor elements and their values for LN are listed in Tab.2, referring to room temperature, static electric field and light of 632.8 nm wavelength [13,14]:

r_{13}	10.0 pm/V
r_{22}	6.7 pm/V
r_{33}	32.2 pm/V
r_{42}	32.6 pm/V

Tab.2: Electro-optic tensor values for LN, from [13,14].

2. Nonlinear optics

2.1 *The dielectric susceptibility*

As said before, one of the most important properties of LN is the nonlinearity, that is, a high value of its nonlinear coefficients, and this is the reason why LN is so widely used in optoelectronics.

Second harmonic generation (SHG) is one of the best technique used for recovering the nonlinear coefficients of this material. SHG is a typical nonlinear optics phenomenon: when a laser beam of frequency ω impinges on a nonlinear material, because of the nonlinear interaction induced by the high intensity of the incident radiation, some of the radiation of frequency ω is converted in radiation of frequency 2ω .

Nonlinear optics [15] studies phenomena that originate as a consequence of the modification of the optical properties of a material in presence of light, i.e. of an electromagnetic radiation. Since only the laser light is strong enough to change the optical properties of a material, the birth of the nonlinear optics field has to be reconducted to the invention of laser (in 1960).

Nonlinear phenomena are “nonlinear” in the sense that they manifest themselves when the response of the medium to an applied optical field depends in a nonlinear way on the intensity of the field. For example, for SHG, the intensity of the generated radiation at frequency 2ω increases as the square of the intensity of the incident laser radiation.

Let's see how the dipole momentum per unit of volume of a material, or **polarization density** $P(t)$, depends on the intensity $E(t)$ of an applied electric field.

In linear optics the polarization depends in a linear manner on the electric field through the relation

$$P(t) = \chi^{(1)} E(t) \quad (4)$$

where the proportionality constant $\chi^{(1)}$ is known as linear **dielectric susceptibility**.

In nonlinear optics the polarization density vector is expressed as a power series of the field $E(t)$. For the α component we have

$$P_{\alpha}(\vec{r}, t) = P_{\alpha}^{(0)} + \sum_{\beta} \left(\frac{\partial P_{\alpha}}{\partial E_{\beta}} \right)_0 E_{\beta} + \frac{1}{2!} \sum_{\beta\gamma} \left(\frac{\partial^2 P_{\alpha}}{\partial E_{\beta} \partial E_{\gamma}} \right)_0 E_{\beta} E_{\gamma} + \dots \quad (5)$$

that can be written

$$P_{\alpha} = \sum_{\beta} \chi_{\alpha\beta}^{(1)} E_{\beta} + \sum_{\beta\gamma} \chi_{\alpha\beta\gamma}^{(2)} E_{\beta} E_{\gamma} + \dots \quad (6)$$

where $\chi_{\alpha\beta}^{(1)}$ is the linear dielectric susceptibility, $\chi_{\alpha\beta\gamma}^{(2)}$ is the second order susceptibility and $\alpha, \beta, \gamma = 1, 2, 3$.

For simplicity we assume that in the medium there are neither losses nor dispersions, that is, the polarization at time t only depends on the instantaneous value of the electric field (“instantaneous response of the medium”).

Let's write again the polarization density as

$$P_{\alpha}(\vec{r}, t) = P_{\alpha}^L(\vec{r}, t) + P_{\alpha}^{NL}(\vec{r}, t) \quad (7)$$

where

$$P_{\alpha}^L(\vec{r}, t) = \sum_{\beta} \chi_{\alpha\beta}^{(1)} E_{\beta}(\vec{r}, t) \quad (8)$$

is the linear part and

$$P_{\alpha}^{NL}(\vec{r}, t) = \sum_{\beta\gamma} \chi_{\alpha\beta\gamma}^{(2)} E_{\beta}(\vec{r}, t) E_{\gamma}(\vec{r}, t) + \dots \equiv P^{(2)} + P^{(3)} + \dots \quad (9)$$

is the nonlinear one.

Physical processes occurring as a consequence of the second order polarization $P^{(2)}$ are different from that occurring as result of the polarization $P^{(3)}$. For example, second order optical interactions happen only in **non-centrosymmetric** materials, i.e. materials not possessing inversion symmetry [15]: among these there is lithium niobate.

Now let's see what are the phenomena related with the second order susceptibility.

Suppose the field can be represented as the discrete sum of fields with frequencies ω_n

$$\vec{E}(\vec{r}, t) = \sum_n \vec{E}_n(\vec{r}, t) \quad (10)$$

where the sum is on the positive frequencies only. For the nth component:

$$\vec{E}_n(\vec{r}, t) = \vec{E}_n^{(+)}(\vec{r}, t) + \vec{E}_n^{(-)}(\vec{r}, t) = \vec{E}_n e^{-i\omega_n t} + \vec{E}_n^* e^{i\omega_n t} \quad (11)$$

where + and - refer to positive and negative frequencies respectively and we used the relation $\vec{E}_n^{(-)} = \vec{E}_n^{(+)*}$ that makes the field real.

Let's consider the case in which the incident field is made up of two components at different frequencies:

$$\begin{aligned} E(\vec{r}, t) &= E_1 e^{-i\omega_1 t} + E_1^* e^{i\omega_1 t} + E_2 e^{-i\omega_2 t} + E_2^* e^{i\omega_2 t} \\ &= E_1 e^{-i\omega_1 t} + E_2 e^{-i\omega_2 t} + c.c. \end{aligned} \quad (12)$$

From this expression we obtain the nonlinear polarization:

$$P^{(2)}(t) = \chi^{(2)} E^2(t) = \chi^{(2)} [E_1^2 e^{-2i\omega_1 t} + E_2^2 e^{-2i\omega_2 t} + 2E_1 E_2 e^{-i(\omega_1 + \omega_2)t} + 2E_1 E_2^* e^{-i(\omega_1 - \omega_2)t} + c.c.] + 2\chi^{(2)} [E_1 E_1^* + E_2 E_2^*] \quad (13)$$

For the different frequencies components we can identify the subsequent complex amplitudes:

$$P(2\omega_1) = \chi^{(2)} E_1^2 \quad \text{second harmonic generation (SHG)}$$

$$P(2\omega_2) = \chi^{(2)} E_2^2$$

$$P(\omega_1 + \omega_2) = 2\chi^{(2)} E_1 E_2 \quad \text{sum frequency generation (SFG)}$$

$$P(\omega_1 - \omega_2) = 2\chi^{(2)} E_1 E_2^* \quad \text{difference frequency generation (DFG)}$$

$$P(0) = 2\chi^{(2)} (E_1 E_1^* + E_2 E_2^*) \quad \text{optical rectification (OR)}$$

These processes can be schematized as in Fig.4:

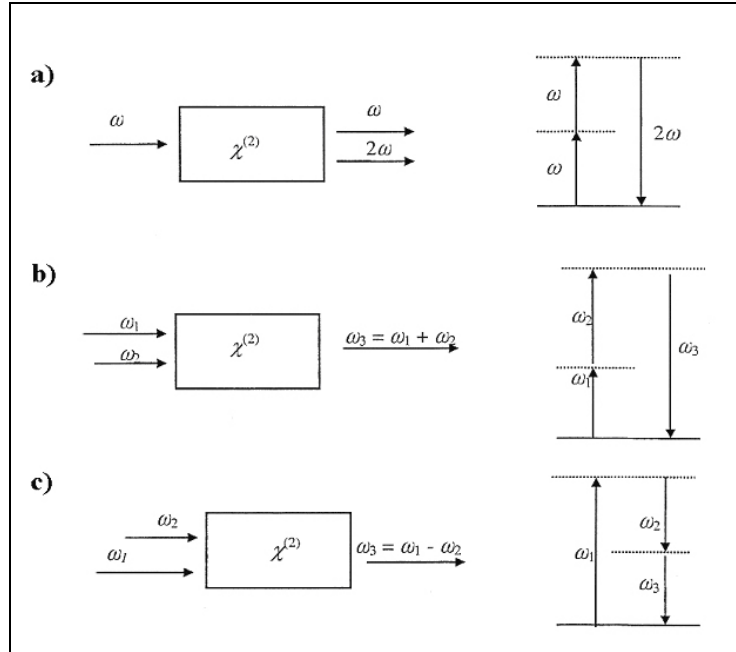


Fig. 4: Geometry and energy levels diagram describing *SHG* (a), *SFG* (b) and *DFG* (c). Levels indicated with dashed lines are virtual levels.

In the previous relations there were four different components for the nonlinear polarization. The SHG phenomenon is described by the first two relations:

$$P(2\omega) = \chi^{(2)} E^2 \quad (14)$$

From an energetic point of view what happens is the generation of a photon at frequency 2ω starting from two photons at frequency ω .

So there are four non-null components of the polarization, corresponding to four different frequencies. Nevertheless, no more than one of them will be present with appreciable intensity in the radiation generated by the nonlinear optical interaction. This is due to the fact that, as it will be seen further, the nonlinear polarization produces a significant output signal only if the particular condition of “phase-matching” is satisfied, and in general this condition cannot be satisfied for more than one frequency.

Apparently it seems that SFG and DFG processes are very similar. In practice, if we consider DFG from an energetic point of view, we see that for each photon created with difference frequency $\omega_3 = \omega_1 - \omega_2$, a photon with higher frequency ω_1 must be destroyed, whereas a photon of lower frequency ω_2 is created. So the field with lower frequency (ω_2) is amplified by this process. For this reason the difference frequency generation is also known as *optical parametric amplification* (OPA).

2.2 Second harmonic generation (SHG)

Let us consider Fig.4. Assume the nonlinear medium is without losses both at fundamental frequency ω_1 and at second harmonic frequency $\omega_2=2\omega_1$, so that the symmetry conditions be valid. In these conditions for the **second harmonic intensity** we have [16] :

$$I_2 = \frac{128\pi^5 (\chi^{(2)})^2 I_1^2}{n_1^2 n_2 \lambda_2^2 c} L^2 \frac{\text{sen}^2 (\Delta k L / 2)}{(\Delta k L / 2)^2} \quad (15)$$

where

$$\Delta k = 2k_1 - k_2 \quad (\text{"phase-mismatch" parameter})$$

$$k_j = \frac{n_j \omega_j}{c}$$

$$n_j = [\varepsilon^L(\omega_j)]^{1/2}$$

with $j=1,2$. The index 1 specifies the radiation of frequency ω , whereas 2 corresponds to the second harmonic (SH). λ_2 is the SH wavelength in vacuum, L the travelled distance inside the nonlinear medium and ε the dielectric constant of the medium.

The expression of I_2 strongly depends on the parameter Δk , as shown in Fig.5.

If $\Delta k \neq 0$, then I_2 is proportional to $\frac{\text{sen}^2(\Delta k L / 2)}{(\Delta k L / 2)^2}$ and oscillates between zero and

the maximum value, depending on the thickness L of the nonlinear medium.

If $\Delta k \rightarrow 0$, then $\frac{\text{sen}^2(\Delta k L / 2)}{(\Delta k L / 2)^2} \rightarrow 1$ and I_2 is proportional to L^2 : the SH intensity

quickly rises with the medium thickness.

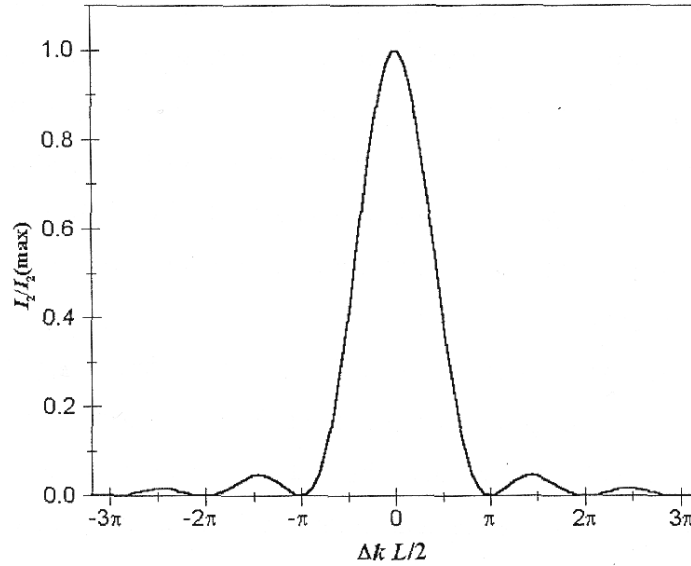


Fig. 5: Normalized *second harmonic intensity* versus parameter $\Delta k L / 2$ for fixed L .

When $\Delta k = 0$ we talk of perfect “*phase-matching*”: the refractive index at fundamental frequency is equal to the index value at SH frequency. Conversely, if $\Delta k \neq 0$, the SH frequencies generated in different points along the fundamental beam’s way do not “strengthen” each other, since they do not travel with the same speed of the incident radiation. So a chaotic interference occurs, and the total SH intensity does not increase.

Let us now introduce the tensor:

$$d_{\alpha\beta\gamma} = \frac{1}{2} \chi_{\alpha\beta\gamma}^{(2)} \quad (16)$$

In the case of SHG exchanging β and γ is insignificant, so we have

$$d_{\alpha\beta\gamma} = d_{\alpha\gamma\beta} \quad (17)$$

and the tensor is symmetric for the exchange of the last two components. This property, here introduced simply for convenience, is called *intrinsic permutation*. We can use a reduced indexes notation for these last two components, that is to put:

$$\begin{array}{lll} xx \rightarrow 1 & yy \rightarrow 2 & zz \rightarrow 3 \\ yz \rightarrow 4 & xz \rightarrow 5 & xy \rightarrow 6 \end{array}$$

So the tensor can be written in the sequent way:

$$d_{ij} \equiv \begin{pmatrix} d_{11} & d_{12} & d_{13} & d_{14} & d_{15} & d_{16} \\ d_{21} & d_{22} & d_{23} & d_{24} & d_{25} & d_{26} \\ d_{31} & d_{32} & d_{33} & d_{34} & d_{35} & d_{36} \end{pmatrix} \quad (18)$$

with $i = 1,2,3$ and $j = 1,2,3,4,5,6$.

We can see that all the indexes χ_{ijk} can be freely permuted if we work in the sequent situations:

- 1) Instantaneous response of the medium
- 2) Transparence zones (the material doesn't absorb at work frequencies)

Such symmetries are the so called *Kleinman's conjectures* [15].

Under these conditions the matrix d_{ij} has only 10 independent elements:

$$d_{ij} \equiv \begin{pmatrix} d_{11} & d_{12} & d_{13} & d_{14} & d_{15} & d_{16} \\ d_{16} & d_{22} & d_{23} & d_{24} & d_{14} & d_{12} \\ d_{15} & d_{24} & d_{33} & d_{23} & d_{13} & d_{14} \end{pmatrix} \quad (19)$$

Moreover, each crystalline symmetry of the nonlinear material further reduces the number of independent components of the tensor. For example, for LN, the tensor reduces to:

$$d_{ij} \equiv \begin{pmatrix} 0 & 0 & 0 & 0 & d_{15} & 0 \\ 0 & d_{22} & 0 & 0 & 0 & 0 \\ 0 & d_{31} & d_{33} & 0 & 0 & 0 \end{pmatrix} \quad (20)$$

The absolute values of the non-vanishing nonlinear coefficients d_{ij} for LN, measured at 1064 nm, are summarized in Tab.3 [17]:

$\mathbf{d}_{15}=\mathbf{d}_{31}(\text{pm/V})$	$\mathbf{d}_{22}(\text{pm/V})$	$\mathbf{d}_{33}(\text{pm/V})$
6.3	3.6	47.0

Tab.3: Second-order nonlinear tensor elements for LN crystal [17].

In the particular configuration adopted for our measurements, that is, as will be explained in the next paragraph, an incident “p” polarized wave beam, forming an angle ϑ with the z-axis (the optical axis of the crystal), it can be seen that the non-zero elements of the tensor are just d_{33} and d_{15} .

3. Measurement of the LN nonlinear coefficients

3.1 Maker's fringes technique

The nonlinear properties of lithium niobate have been tested on a sample consisting of a polished 500 μm thick LN z-cut crystal, by measuring the non-zero components of the second order susceptibility tensor d_{ij} . As said before, for LN they are only d_{33} and d_{15} .

The measurement has been performed through the Maker's fringes method, the theoretical model of which was elaborated by Herman and Hayden (H-H model) [18]. This model, differently from that built up by Jerphagnon and Kurtz (J-K model) [19], can be applied to all classes of materials, as it considers also absorbing and anisotropic materials; besides, it takes into account multiple reflections of the SH wave inside the nonlinear medium.

The SH field propagating inside a nonlinear crystal is described by Maxwell's equations, one solution being a superposition of a "free" wave generated at the input surface and a "bound" wave, generated by the nonlinear polarization inside the sample. These two waves interfere producing a SH signal, that is a function of the angle ϑ between the incident beam and the normal direction to the medium: a variation of ϑ results in a variation of the optical path inside the material and, consequently, the SHG efficiency is modified.

The final result for the transmitted **second harmonic power** for an absorbing material, neglecting multiple reflections and considering the refractive index as a complex number, is [18]:

$$P_{2\omega}(\vartheta) = \frac{512\pi^3}{cA} \frac{t_{a \rightarrow Nb}^4 \cdot t_{Nb \rightarrow a}^2}{n_{2\omega}^2 \cos^2 \vartheta_{2\omega}} \left(\frac{\pi T}{\lambda} \right)^2 d_{eff}^2 \frac{\sin^2 \psi}{\psi^2} \cdot P_{\omega}^2 \quad (21)$$

where

$$\psi = \frac{2\pi T}{\lambda} (n_{\omega} \cos \vartheta_{\omega} - n_{2\omega} \cos \vartheta_{2\omega}) \quad (22)$$

$$\vartheta_{\omega} = \arcsin\left(\frac{\sin \vartheta}{n_{\omega}}\right); \quad \vartheta_{2\omega} = \arcsin\left(\frac{\sin \vartheta}{n_{2\omega}}\right) \quad (23)$$

$$d_{eff} = 2d_{15} \sin \vartheta_{\omega} \cos^2 \vartheta_{\omega} + d_{33} \sin^3 \vartheta_{\omega} \quad (24)$$

ϑ is the angle between the normal to the crystal surface and the k wave vector of the incident field, ϑ_{ω} and $\vartheta_{2\omega}$ the refractive angles of the first and SH rays respectively (see Fig.6), t_{a-Nb} and t_{Nb-a} are the Fresnel's transmission coefficients of the air-substrate and substrate-air interfaces respectively, d_{eff} is a linear combination of the susceptibility tensor components, T is the thickness of the sample (in this case 0.5 mm), $n_{\omega}=2.23$ and $n_{2\omega}=2.32$ the first and second harmonic refractive indexes of LN [9], $A \approx 3\text{mm}^2$ is the transverse section (the area) of the incident beam.

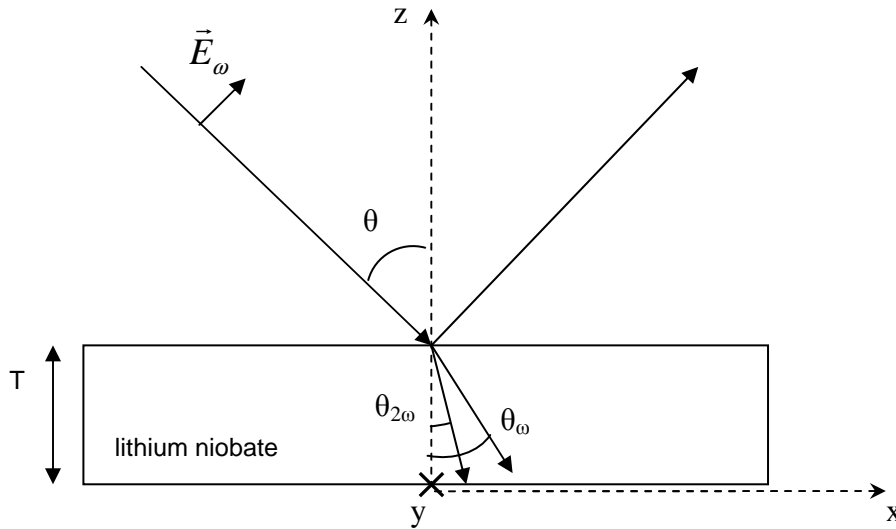


Fig. 6: Scheme of the incident, reflected and refracted beams at different frequencies, and of the coordinates system adopted.

From equation (21) we deduce that, knowing the thickness T , the optical power P_ω , the wavelength λ , the material symmetries and the refractive indexes n_ω and $n_{2\omega}$, is univocally determined the value of the function:

$$\Phi(\vartheta) \equiv \frac{P_{2\omega}(\vartheta)}{P_\omega^2} = \frac{512\pi^3}{c A} \frac{t_{a \rightarrow Nb}^4 \cdot t_{Nb \rightarrow a}^2}{n_{2\omega}^2 \cos^2 \vartheta_{2\omega}} \left(\frac{\pi T}{\lambda} \right)^2 d_{eff}^2 \frac{\sin^2 \psi}{\psi^2} \quad (25)$$

This equation is proportional to the SH signal, $V_{2\omega}$, through a certain constant of proportionality, D_{exp} , that is necessary to determine in order to obtain the d_{ij} coefficients.

Since the determination of d_{ij} also depends on the experimental apparatus' characteristics (such as the efficiency of the detector), which cannot be independently determined, it is necessary to carry out measurements on a sample whose d_{ij} is known, and has been chosen quartz. Because of the material symmetries the only independent component for quartz is $d_{11}=0.5$ pm/V ($d_{eff} = d_{11} \sin 3\vartheta_\omega$).

3.2 *Experimental methods and results*

The experimental apparatus built-up for the SH measurements is depicted in Fig.7:

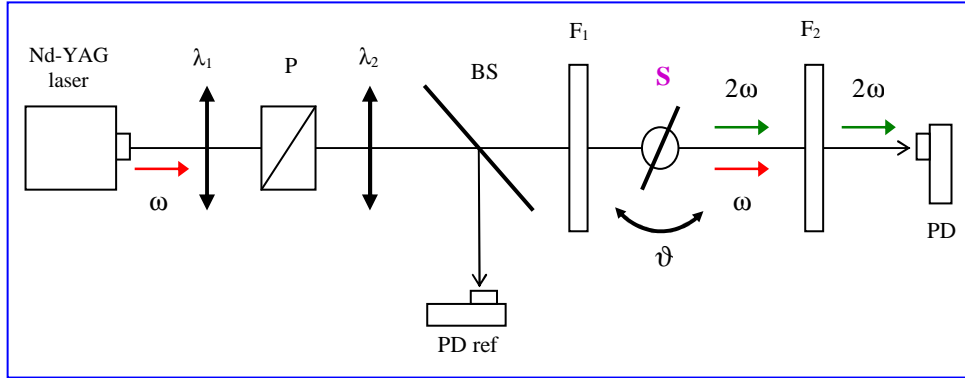


Fig. 7: Scheme of the *experimental set-up* adopted for the measurement of the SH signal generated by the sample.

The source is a pulsed Nd-YAG, a solid state laser with four levels whose active medium is the crystal $Y_3Al_5O_{12}$, doped with Nd^{3+} ions. The output energy is of about 300 mJ with repetition rate of 10 Hz. The pulses duration is about 8 ns, obtained with the Q-switching technique. The fundamental output wavelength is $\lambda=1064$ nm, and the mode is the TEM_{00} , with gaussian shape.

The light beam passes through a variable attenuator, constituted of an half-wave plate (λ_1) and a polarization cube (P). A second half-wave plate (λ_2) is necessary to change the polarization exiting from the cube in order to set the linear polarization of the beam impinging on the sample, that in the case of LN has to be of “p” type (parallel to the plane formed by the incident ray and the normal to the sample’s surface).

Before reaching the sample, the beam is splitted in two by a beam splitter (BS): the main beam is directed to the sample, the reference one to a reference photodiode (PD ref). The role of this photodiode is to detect the intensity variations of the incident signal, caused by the laser intrinsic fluctuations (representing a big source of errors), in order to obtain a reference signal V_ω . This is proportional to the incident energy on the sample E_ω and consequently to the power P_ω .

Such linearity was verified by placing a power meter before the sample and changing the incident power by means of the variable attenuator. In Fig.8 are represented the signals detected by the reference PD (V_ω) and that detected by the power meter (E_ω). With a linear fit it has been possible to determine the proportionality coefficient.

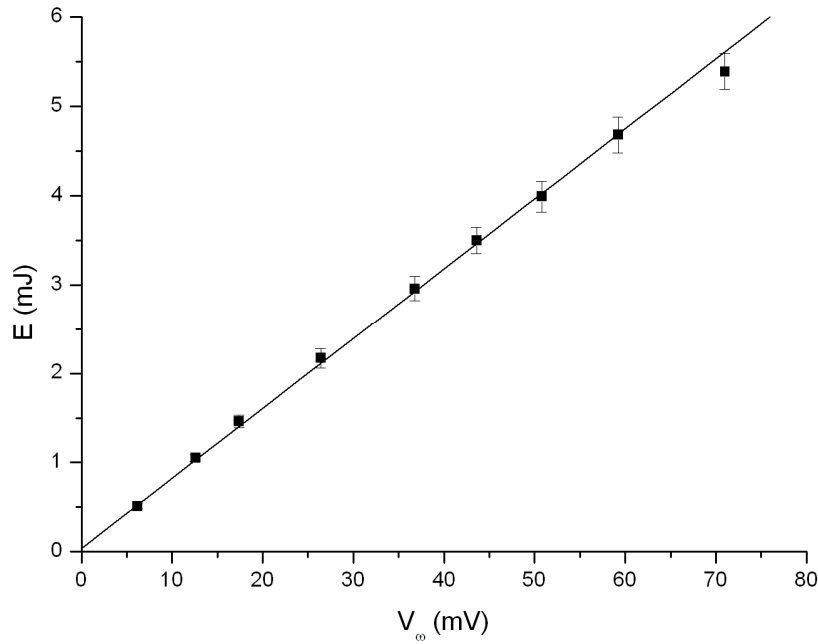


Fig. 8: Energy measurements performed with the power meter corresponding to that performed with the reference photodiode. The fit confirms the linearity of the experimental data.

After the BS, the main beam goes through a low-pass filter (F_1) that stops the SH radiation and lets the infrared radiation (of lower frequency) pass and reach the sample; this permits to detect the SH signals coming only from the sample, and not that undesirably generated by the optical components of the system. The infrared beam impinges on the LN crystal (S), placed on a support that permits the sample optical axis rotation of an angle ϑ with respect to the propagation direction (see Fig. 7), with a resolution of one degree.

Another filter, F_2 , this time high-pass, blocks the infrared radiation and permits the visible one (of higher frequency) to pass, with the aim to detect just the SH signal. The main detector, a silicon photodiode (PD), converts the light signal into an electrical signal, $V_{2\omega}$.

For each angle of incidence ϑ the SH signal $V_{2\omega}$ and the reference one V_{ω} have been acquired, by means of a digital oscilloscope. The same apparatus has been used for the measurements of quartz Maker's fringes, adopted as a reference. The only difference is that this time the plate λ_2 has been placed in a different way: in fact for the determination of the d_{11} of quartz is necessary a linear "s" polarization.

The $V_{2\omega}$ signals have been divided by the square of the incident energy, E_{ω}^2 , in order to account for laser intrinsic fluctuations. In this way the Maker's fringes of quartz have been obtained, as displayed in Fig.9.

At this point, a nonlinear fit with "*Mathematica*" has been performed, according to the relation

$$\frac{V_{2\omega}}{E_{\omega}^2}(\vartheta) = D_{exp} \Phi_{2\omega}(\vartheta) \quad (26)$$

on the parameter D_{exp} , that is the proportionality constant between the detected signal and the Φ function defined above (that in this case is known).

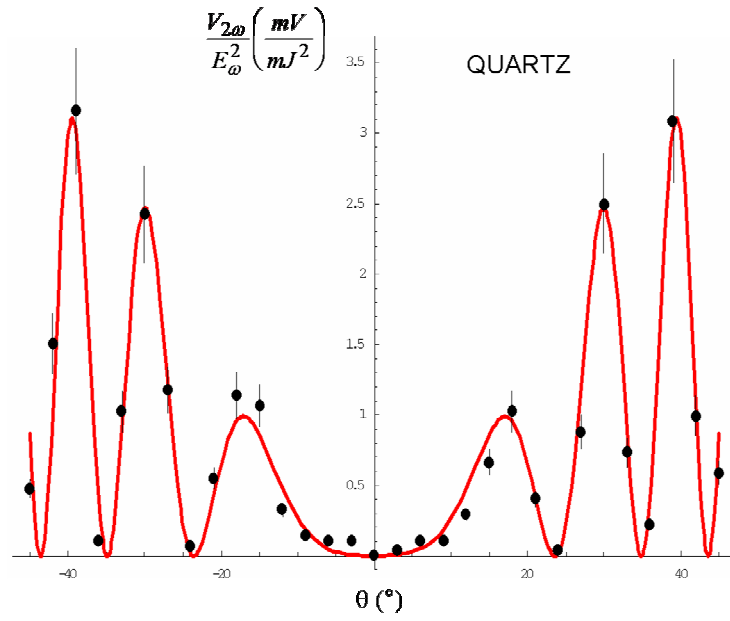


Fig. 9: *Maker's fringes* of quartz. The red line represents the nonlinear fit.

For the LN sample the same thing has been done: a measure of $V_{2\omega}$ and V_{ω} signals, dividing $V_{2\omega}$ to E_{ω}^2 . The results are shown in Fig. 10.

Knowing the constant D_{exp} that contains information about the experimental apparatus, the same fit of eq.(26) has been performed, but this time using d_{33} and d_{15} as unsettled parameters.

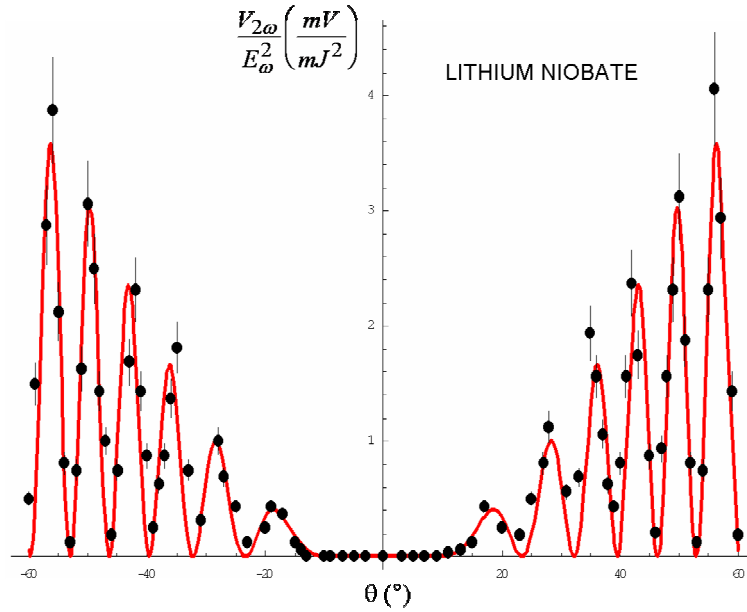


Fig. 10: Maker's fringes of lithium niobate.

The final result is:

$$\mathbf{d}_{33} = 44 \pm 11 \text{ pm/V}$$

$$\mathbf{d}_{15} = 8.6 \pm 0.7 \text{ pm/V} \quad (27)$$

We note that this value is much larger than that of quartz, and this is a confirmation of the fact that LN is an excellent nonlinear and electro-optic material, being the two properties strictly related [17,20].

It is clear that these values are just as an indication, as they depend on many factors such as the temperature, humidity, impurities of the material and so on. Before this, a lot of measurements using Maker's fringes technique have been performed on nonlinear materials and in particular on LN, and the nonlinear coefficients are well known and tabulated (see Tab.3). Nevertheless, it is important to know the coefficients values for *this* particular kind of LN (with its impurities, ecc.), as it will be used for all the experiments described in this treatise.

Conclusions

In this chapter an overview on lithium niobate has been given, describing its main properties and applications.

The nonlinear characterization, carried out by means of the Maker's fringes technique taking advantage of the second harmonic generation of the medium, has put in evidence the reason why lithium niobate is one of the most used materials for electro-optic devices: a very large value of the second order susceptibility tensor elements (at least one order of magnitude larger than that of quartz), and consequently a large value of the electro-optic coefficients of the material.

This result is very important because the electro-optic effect will be widely exploited for the applications of this type of LN described in the next chapters.

References:

- [1] B.T. Matthias, J.P. Remeika: “Ferroelectricity in the Ilmenite Structure”, *Phys. Rev.* **76**, p.1886 (1949).
- [2] A. Yariv: *Quantum electronics*, John Wiley & Sons (1989).
- [3] R.S. Weis, T.K. Gaylord: “Lithium Niobate: Summary of Physical Properties and Crystal Structure”, *Appl. Phys. A* **37**, p.191 (1985).
- [4] T. Volk and M. Wohlecke: *Lithium Niobate: Defects, Photorefraction and Ferroelectric Switching*, Springer (2008), p.1–9.
- [5] K. Nassau, H.J. Levinstein, G.M. Loiacono: “Ferroelectric lithium niobate: growth, domain structure, dislocations and etching”, *J. Phys. Chem. Solids* **27**, p.983 (1966).
- [6] H.M. O’Bryan, P.K. Gallagher, C.D. Brandle: “Congruent Composition and Li- Rich Phase Boundary of LiNbO_3 ”, *J. Am. Ceram. Soc.* **68**, p.493 (1985).
- [7] S.C. Abrahams and P. Marsh: “Defect structure dependence on composition in lithium niobate”, *Acta Cryst. B* **42**, p.61 (1986).
- [8] B.M. Park et al.: “Mechanical twinning in stoichiometric lithium niobate single crystal”, *J. Cryst. Growth.* **180**, p.101 (1997).
- [9] G. J. Edwards and M. Lawrence: “A temperature-dependent dispersion equation for congruently grown lithium niobate”, *Opt. and Quant. Elec.* **16**, p.373-375 (1984).
- [10] D.S. Smith, H.D. Riccius, R.P. Edwin: “Refractive indices of lithium niobate”, *Opt. Comm.* **17**, p.332 (1976).
- [11] G.D. Boyd, R.C. Miller, K. Nassau, W.L. Bond, A. Savage: “ LiNbO_3 : an efficient phase matchable nonlinear optical material”, *Appl. Phys. Lett.* **5**, p.234 (1964).
- [12] K.K. Wong Ed.: *Properties of lithium niobate*, IEE London (2002).

- [13] R. Nevado et al.: "Compositional characterisation of Zn-diffused lithium niobate waveguides" *Appl. Phys. B* **73**, p.555 (2001).
- [14] N. Hamelin and Y.T. Chow: "Guided-type second harmonic generation in ion implanted MgO:LiNbO₃", *J. Mod. Opt.* **45**, p.2125 (1998).
- [15] R.W. Boyd: *Nonlinear Optics*, Academic Press (2002).
- [16] Y.R. Shen: *The Principles of Nonlinear Optics*, John Wiley & Sons (1984).
- [17] S.K. Kurtz and S.H. Wemple: "Materials for Nonlinear Optics", Part D of *Laser Handbook*, F.T. Arecchi and E.O. Schulz-Dubois eds. (North-Holland Publishing Company, Great Britain, 1972).
- [18] W.N. Herman and L.M. Hayden: "Maker fringes revisited: second-harmonic generation from birefringent or absorbing materials", *J. Opt. Soc. Am. B* **12**, p.416 (1995).
- [19] J. Jerphagnon and S.K. Kurtz: "Maker Fringes: A Detailed Comparison of Theory and Experiment for Isotropic and Uniaxial Crystals", *J. Appl. Phys.* **41**, p.1667 (1970).
- [20] M. Izdebski, W. Kucharczyk and R.E. Raab: "On relationships between electro-optic coefficients for impermeability and nonlinear electric susceptibilities", *J. Opt. A: Pure Appl. Opt.* **6**, pp.421–424 (2004).

Chapter II

Super-resolution in digital holography

Summary

This chapter describes a relevant experimental technique adopted for the studies performed in this and in the sequent chapters: digital holography (DH). DH is an interferometric technique that permits, starting from a digitally recorded interference fringe pattern, to numerically reconstruct the wavefront propagating through the sample under test. There will be a short essay on the principle of operation and on the many applications of this technique, such as microscopic imaging and the enhancement of resolution (“super-resolution”).

Then I will focus on one of the applications of LN, that is a diffracting grating to get super-resolution in digital holographic microscopy. In fact, by means of a flexible hexagonal LN phase grating, it has been possible to increase the numerical aperture of the imaging system, thus improving the spatial resolution of the images in two dimensions.

This spatial resolution enhancement could be also useful in the characterization of optical waveguides and of microlenses arrays described in the next chapters.

1. Interferometric digital holography

1.1 From classical to digital holography

Holography was invented by Dennis Gabor in 1948 as a method for recording and reconstructing both the amplitude and the phase of an optical wavefield [1]. In holography, an object is illuminated by a light beam with sufficient coherence length. The illuminating beam is split into two waves by a beam splitter. One wave impinges upon the object and is scattered and reflected from it, and is called “object beam”. The second wave is called the “reference beam” and interferes with the object beam in the plane of a recording medium, such as a photographic plate. The **hologram** (from the Greek words “όλος” meaning “whole” or “entire” and “γράφω” meaning “to write”) contains information about the entire three-dimensional distribution of the optical wave field in the form of an interferometric fringe pattern. The object is reconstructed by illuminating the recorded hologram with a replica of the original recording reference wave.

Since its discovery, holography has become a very useful metrological tool in experimental mechanics, biology, fluid dynamics and non destructive inspection [2,3].

However, one of the main limitations of holography and its related approaches has been the unpractical chemical procedures connected with the need of having film plates as recording medium. Such limitation has been partially overcome by means of the advent of digital speckle holographic methods [4]. Nevertheless speckle methods are not “holographic” since they cannot reconstruct amplitude of object beams but only phase difference occurred in two or more different states of the object under investigation.

The idea of using a computer for reconstructing a hologram was proposed for the first time by Goodman and Laurence [5]. The development of computer technology and solid-state image sensors made it possible to directly record holograms by charge coupled device (CCD) cameras [6]. This important step

enabling full digital recording and reconstruction of holograms, without using any photographic recording medium, is commonly referred to as *digital holography (DH) method*. Replacing the photographic film with a CCD implies that conventional recording techniques have to be properly modified to meet the requirements placed by the use of the camera, without changing the basic purpose of holography, which is the reconstruction of the object field from the recorded interference pattern. Indeed, this is the key step to calculate quantities related to the object under investigation, such as displacement vector field of surface in deformation analysis and shape measurements, refractive index changes in transparent media, particle tracking and microscopy just to quote few examples of current research fields. In these applications, a modification of the state of the object leads to a modification of the wave field scattered, reflected or transmitted by it, and to a change of the digitally recorded interference pattern.

In DH, the reconstruction of the object field is performed numerically from the direct recording of the digitized numerical hologram. Since the information of the optically interfering waves is stored in the form of matrices, the numerical reconstruction process enables full digital processing of the holograms and offers much more possibilities than conventional optical processing. Both amplitude and phase of the reconstructed complex field can be computed.

The possibilities offered by digital processing concern for example subtraction of background noise and the elimination of the zero-order diffraction term [7]. Furthermore, the parameters governing the reconstruction algorithm can be properly selected in order to control and optimize the spatial resolution of the reconstructed object field, thus compensating for lack of spatial resolution of digital cameras compared to the conventional photographic plates. The limitation imposed by the low spatial resolution of CCD camera array compared to that of photographic materials have been widely discussed and many configurations of digital holography have been proposed and applied in various fields of science and engineering [8 and refs. therein]. Moreover, recent efforts

addressed for developing new optoelectronic devices, such as solid state pyroelectric sensors for the infrared region, made also possible to extend the potentialities of DH as a useful technique for metrological applications with light sources emitting in spectral regions different from the visible one [9].

1.2 Theory and principle of operation of digital holography

The principle of the optical recording and reconstruction in classical holography can be understood by referring to the basic set-up shown in Fig.1.

The reference beam R interferes at the plane of the holographic plate at off-axis angle θ with respect to the object beam O . In this set-up the reconstructed image is spatially separated by the zero-order diffraction and the second image, the so-called ‘twin image’. These three diffraction orders propagate along different directions and can be observed separately, leading to a significant improvement compared to the in-line configuration originally developed by Gabor, where the zero-order and the two conjugate images overlapped [10].

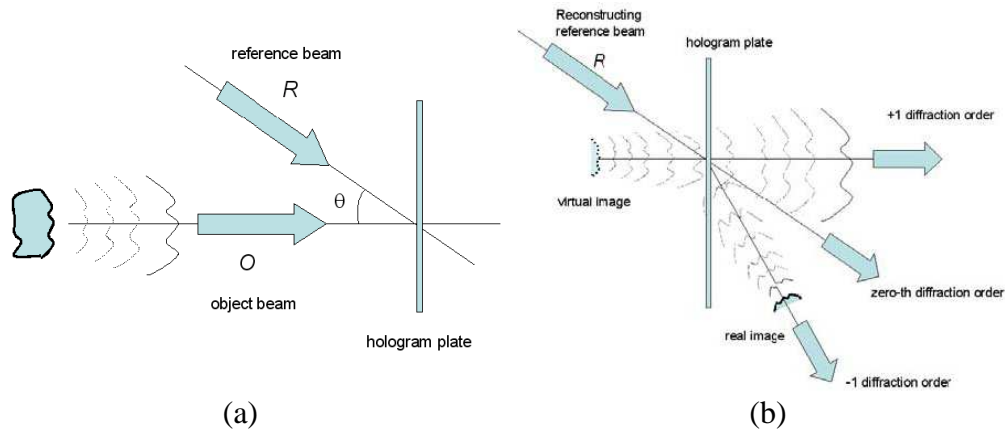


Fig. 1: Optical configuration for recording (a) and for reconstruction (b) of off-axis holograms.

The intensity distribution $I(x, y)$ across the x - y holographic recording plane can be written in the squared modulus of the complex superposition $O(x, y) + R(x, y)$, namely

$$\begin{aligned} I(x, y) &= |O(x, y) + R(x, y)|^2 = \\ &= |R(x, y)|^2 + |O(x, y)|^2 + R^*(x, y) O(x, y) + R(x, y) O^*(x, y) \end{aligned} \quad (1)$$

where the symbol $*$ denotes complex conjugation,

$O(x, y) = |O(x, y)| \exp [i \varphi_o(x, y)]$ is the complex amplitude of the object wave with real amplitude $|O(x, y)|$ and phase $\varphi_o(x, y)$, and

$R(x, y) = |R(x, y)| \exp [i \varphi_R(x, y)]$ is the complex amplitude of the reference wave with real amplitude $|R(x, y)|$ and phase $\varphi_R(x, y)$.

For the numerical reconstruction of the recorded hologram, the interference pattern $I(x, y)$ is illuminated by the reference wave $R(x, y)$, i.e we have

$$\begin{aligned} R(x, y)I(x, y) &= R(x, y)|R(x, y)|^2 + R(x, y)|O(x, y)|^2 + \\ &+ |R(x, y)|^2 O(x, y) + R^2(x, y) O^*(x, y) \end{aligned} \quad (2)$$

The first term on the right side of this equation is proportional to the reference wave field, the second one is a spatially varying “cloud” surrounding the first term. These two terms constitute the zero-order of diffraction or *DC term*. The third term represents, apart for a constant factor, an exact replica of the original wavefront $O(x, y) = |O(x, y)| \exp [i \varphi_o(x, y)]$, and for this reason it is called *virtual image*, or simply image of the object. The last term is the conjugate, the so called *twin image*, of the original object wave (or *real image*).

In holography, the hologram can be regarded like an amplitude transmittance that diffracts the reference wave. In DH the numerical reconstruction process of the object wave field is determined through the numerical calculation of the

optical field propagation of $R(x, y)I(x, y)$ from the holographic plane back to the object plane $\xi - \eta$, as shown in Fig.2.

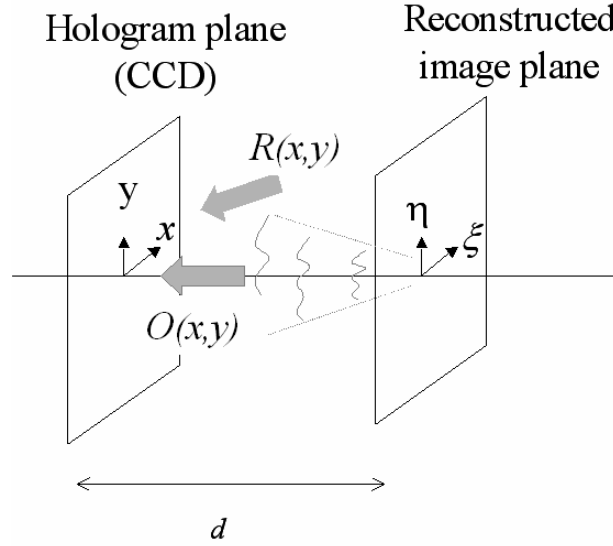


Fig. 2: Optical set-up in off-axis digital holography.

The numerical reconstruction of digitally recorded holograms follows the scalar diffraction theory in the Fresnel approximation of the Rayleigh-Sommerfield diffraction integral [11]. The reconstructed diffracted field $Q(\xi, \eta)$ in the reconstruction plane $\xi - \eta$ at distance d from the hologram plane can be written in the paraxial approximation in the following form:

$$Q(\xi, \eta) = \frac{1}{i\lambda d} \exp\left(i\frac{2\pi}{\lambda}d\right) \times \int_{-\infty}^{\infty} \int_{-\infty}^{\infty} R(x, y)I(x, y) \exp\left\{i\frac{\pi}{\lambda d}[(\xi - x)^2 + (\eta - y)^2]\right\} dx dy \quad (3)$$

Eq.(3) is the starting point for numerically reconstructing the digitized hologram in the paraxial approximation, where the x and y values and the corresponding ξ and η values in the reconstructed plane are small compared to the distance d (see Fig.2).

Once calculated the complex field $Q(\xi, \eta)$ at distance d , the intensity $I(x, y; d)$ and the phase distribution $\varphi(x, y; d)$ of the reconstructed image can be determined by the following relations:

$$I(x, y; d) = |Q(x, y)|^2 \quad (4a)$$

$$\varphi(x, y; d) = \arctan \frac{\text{Im}[Q(x, y)]}{\text{Re}[Q(x, y)]} \quad (4b)$$

Eq. (4b) provides phase values wrapped in the interval $[-\pi, \pi]$. Unwrapping procedures can be employed to convert the phase modulo- 2π into a continuous phase distribution in order to obtain a smooth phase image [12].

1.3 Reconstruction methods

Different techniques can be adopted for implementing a reconstruction of digital holograms. The most important (the one adopted for the studies in this thesis) is the *Fresnel transformation method (FTM)*.

The convolution integral given by Eq.(3) can be manipulated to obtain the reconstructed diffracted field $Q(\xi, \eta)$ in terms of the so-called Fresnel transformation of the hologram function. Indeed it results that

$$Q(\xi, \eta) = \frac{1}{i\lambda d} \exp\left(i\frac{2\pi}{\lambda}d\right) \exp\left[i\frac{\pi}{\lambda d}(\xi^2 + \eta^2)\right] \times \int_{-\infty}^{\infty} \int_{-\infty}^{\infty} R(x, y) I(x, y) \exp\left[i\frac{\pi}{\lambda d}(x^2 + y^2)\right] \exp\left[-i\frac{2\pi}{\lambda d}(\xi x + y\eta)\right] dx dy \quad (5)$$

Eq.(5) shows that the reconstruction field is determined essentially by the two-dimensional Fourier transformation of the hologram $I(x, y)$ multiplied by the reference wave $R(x, y)$ and the “chirp” phase function

$$w(x, y) \equiv \exp\left[i\frac{\pi}{\lambda d}(x^2 + y^2)\right]$$

Eq. (5) can be re-written in terms of the Fourier integral

$$Q(v_\xi, v_\eta) = \frac{1}{i\lambda d} \exp\left(i\frac{2\pi}{\lambda}d\right) \exp\left[i\pi\lambda d(v_\xi^2 + v_\eta^2)\right] \cdot \mathfrak{F}^{\pm 1}[R(x, y)I(x, y)w(x, y)](v_\xi, v_\eta) \quad (6)$$

where the direct (+1) or inverse (-1) continuous two dimensional Fourier transformations of the function $f(x, y)$ are defined, respectively, by

$$\mathfrak{F}^{\pm 1}[f(x, y)](v_\xi, v_\eta) = \int_{-\infty}^{\infty} \int_{-\infty}^{\infty} f(x, y) \exp[\mp i2\pi(v_\xi x + v_\eta y)] dx dy \quad (7)$$

In Eq.(7) v_ξ and v_η are the *spatial frequencies* corresponding to the spatial variables ξ and η in the reconstruction plane and are related to the reconstruction wavelength λ and to the reconstruction distance d by the following relations:

$$v_\xi = \frac{\xi}{\lambda d}, \quad v_\eta = \frac{\eta}{\lambda d} \quad (8)$$

With the off-axis geometry the object wave and the reference wave arrive in the hologram plane with separate directions and, according to the above equations, the different terms of the numerically reconstructed wavefront propagate along different directions, owing to their different spatial frequencies. In fact, if Eq.(2) is substituted into Eq. (5), it is clear that the reconstruction of the DC term, the virtual and the real image are essentially governed by the frequency content of the respective spectra at the reconstruction distance d , which ultimately impose restrictions on the spatial bandwidth of the object and reference beams. If the

reference field is given by $R(x, y) = \sqrt{I_R} \exp[i(k_x x + k_y y)]$, where $I_R = |R(x, y)|^2$ is the intensity of the reference field and $\mathbf{k} = (k_x, k_y, k_z)$ is the corresponding wave vector, the three terms are separated in the Fourier domain corresponding to the reconstruction plane $\xi - \eta$ at distance d . The zero-order is located around the origin while the image and the twin image are symmetrically centred on $(k_x/2\pi, k_y/2\pi)$ and $(-k_x/2\pi, -k_y/2\pi)$, respectively.

To achieve good quality reconstruction in DH, the sampling theorem (Nyquist criterion) has to be fulfilled across the whole CCD array area [13]. The criterion requires at least two pixel per fringe period; this implies that the maximum interference angle α_{\max} between the spherical wavelets from each point of the object and the reference wave field be determined by the pixel size Δx , according to the relation:

$$\alpha_{\max} = \frac{\lambda}{2\Delta x} \quad (9)$$

Relation (9) expresses the fact that for recording an hologram by a CCD array with pixel spacing Δx at least two pixels per fringe are needed. For example in case of a camera with pixel size $\Delta x = 6.7 \mu\text{m}$, the maximum interference angle is $\alpha_{\max} \approx 2.3^\circ$ for $\lambda = 532 \text{ nm}$.

Without loss of generality it can be seen that, if the whole CCD array has a finite width given by $N\Delta x \times M\Delta y$, where Δx and Δy are the pixel sizes on the CCD array in the horizontal and vertical directions, respectively, and N and M are the pixel numbers in each direction, the dimensions $\Delta\xi \times \Delta\eta$ of the reconstruction pixel are:

$$\Delta\xi = \frac{\lambda d}{N\Delta x}, \quad \Delta\eta = \frac{\lambda d}{M\Delta y} \quad (10)$$

According to Eq.(10) the pixel width in the reconstructed plane is different from that of the digitized hologram and it scales inversely to the aperture of the optical system, i.e., to the side length $S = N\Delta x$ of the hologram (limiting the analysis to the x -direction for the sake of simplicity).

This result is in agreement with the theory of diffraction which predicts that at a distance d from the hologram plane the developed diffraction pattern is characterized by the diameter $\lambda d/S$ of its *Airy disk* (or speckle diameter). Therefore the resolution of the reconstructed image (amplitude or phase image) is limited by the diffraction limit of the imaging system through the automatic scaling imposed by the Fresnel transform.

It is easy to obtain the approximate condition (limiting our analysis to one dimension only) that determines the range of distances d where the discrete Fresnel reconstruction algorithm gives good results, namely:

$$d \geq d_c = \frac{N\Delta x^2}{\lambda} \quad (11)$$

As an example, for $N=512$ pixels, $\lambda=632\text{nm}$ and pixel size $\Delta x = \Delta y = 11\mu\text{m}$, the Fresnel method is valid for distances greater than 98mm, while for $N=1024$ pixels, $\lambda=532\text{nm}$ and $\Delta x = \Delta y = 6.7\mu\text{m}$, the distance has to be greater than 86.4mm.

1.4 Digital holographic microscopy (DHM)

DH is an ideal technique for retrieving the phase distribution of the object wave field for quantitative phase contrast imaging in microscopy, meaning that the reconstructed phase distribution can be directly used for metrological applications, such as surface profilometry. The reconstruction process, in fact, is flexible and unique because focusing can be adjusted and aberrations can be removed numerically. Moreover, phase distribution, that cannot be observed in

optical reconstruction of film holography, is easily computed and displayed quantitatively.

Actually, there are other methods based on interferometry that allow one to measure minute displacements and surface profiles. Methods like holographic interferometry, fringe projection and speckle metrology can provide full-field non-contact information about coordinates, deformations, strains, stresses and vibrations. However, an important advantage of DH, in comparison with interference microscopy, is that the curvature introduced on the object beam by the microscope objective lens have not to be compensated by the very same curvature introduced on the reference beam. In fact, in interference microscopy this problem is solved experimentally by inserting the same microscope objective in the reference arm, at an equal distance from the exit of the interferometer.

For example the Linnick interferometer requires that if any change has to be made in the object arm, then the same change must be precisely reproduced in the reference arm in such a way that interference occurs between similarly deformed wavefronts. As a consequence, the experimental configuration requires a very high degree of precision. However, it is important to point out that DH, compared with other 3D measuring techniques using mechanical or electrical scanning, that are intrinsically point-wise methods, allows the direct calculation of the full-field map of the object through the calculation of the complex wavefront from a single exposure. As a consequence, both the acquisition time and the sensitivity to thermal and mechanical stability are reduced. Several applications have been demonstrated by using DHM [14-19].

In a microscope DH configuration, high magnification ratios are obtained by inserting an imaging system that magnifies the size of the object, but the image of the object is not imaged directly on the CCD array. On the contrary, the image of the object lies in a plane that can be behind or in front the CCD, at a certain distance from the sensitive array. Refocusing by a digital holographic microscope relies on the possibility to obtain the complex optical field at

whichever plane along the propagation distance of the object beam. The sample image can be refocused to its position computing the optical complex field in a plane located at the same distance d from the hologram plane at which the object was during the recording process. In this way the best in focus numerically reconstructed amplitude and phase image of the object can be obtained. In case of a 3D object, numerical focusing of different parts of the object at different distance can be focused separately.

DHM can be applied for example to obtain the profile map of an opaque object. In this case a DHM *reflection configuration* has to be adopted, as shown in Fig.3. The height distribution $h(\xi, \eta; d)$ of the object at distance d from the hologram plane is the information to be retrieved. It is simply related to the reconstructed phase distribution $\phi(\xi, \eta; d)$ by the simple relationship:

$$h(\xi, \eta; d) = \frac{\lambda}{4\pi} \phi(\xi, \eta; d) \quad (12)$$

As previously described, the values of the measured phase are restricted in the interval $[-\pi, \pi]$ and ambiguities arising from height differences greater than $\lambda/2$ can be resolved by use of standard phase unwrapping methods.

In Fig.3 a possible set-up for a digital holographic microscope is shown.

The set-up consists basically of a Mach-Zehnder interferometer for reflection imaging. For transparent objects a transmitting configuration can be alternatively arranged. In the reference arm a beam expander is introduced in order to produce an expanded beam with a plane wavefront. In the object arm, in order to illuminate the sample with a collimated beam, a combination of a beam expander, a lens with a long focal length and a microscope objective is used. This imaging system permits to obtain a magnified image of the sample object that is used for the hologram creation.

In order to control the intensities in both the arms, a combination of a neutral density filter, a half-wave plate and a polarizing beam splitter can also be used.

The advantage of a Mach-Zehnder configuration is that it allows the recording of off-axis holograms with very small angles between the directions of propagation of the object and reference waves. This feature is important when low-resolution media are used as image acquisition systems.

Finally, a CCD camera acquires an image of the hologram. Resolution better than 10 nm can be estimated for step-height measurements in DHM, as has been demonstrated in direct measurements of profiles of tiny steps [19].

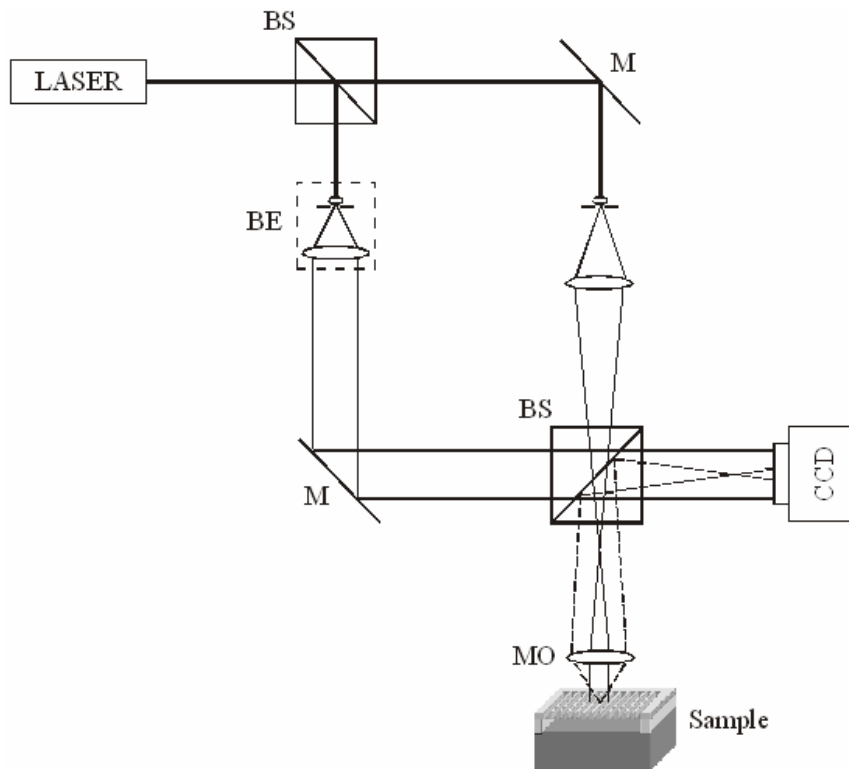


Fig.3: Experimental set-up for recording digital holograms in a reflection configuration: BS = beam splitter, M = mirror, MO = microscope objective, BE = beam expander.

DHM is very suitable for inspecting microstructures (such as microlens arrays, described in Chapter IV), or real-time acquisition, even in case of moving

objects [18]. Furthermore, thanks to the versatility of the reconstruction process, it is possible for example to numerically control the image size [20] and the image resolution [21-24]. We will now concentrate on this last feature.

2. Super-resolution in digital holographic microscopy

2.1 Introduction

The computational image reconstruction from a digital hologram, in DHM, has many advantages compared to the traditional optical holography, including amplitude and phase imaging, 3D imaging and the digital wavefront manipulation.

On the other hand, some disadvantages also exist. In fact, no electronic device is able to compete with the high resolution (up to 5000 lines/mm) of the photographic emulsions used in optical holography. Therefore, in most cases, the resolution achieved in DHM is too low and not qualified for practical applications.

Recently, important results have been achieved for increasing the optical resolution in DH imaging, thus opening new possibilities in 3D microscopy. It is well known that, in microscopy, the resolution of the optical systems is limited by its numerical aperture (NA). Essentially, because of the finite aperture of the imaging system, only the low frequency parts of the object spectrum are transmitted and then recorded by the sensor. Therefore, the corresponding reconstructed images are band limited in the frequency domain.

Several strategies have been defined and different approaches have been tested to increase the NA of the optical system in order to get super-resolution. Most of the aforementioned methods are essentially aimed at increasing synthetically the NA of the light sensor to get super-resolution. Massig et al. increased the NA by recording nine holograms with a CCD camera translated to different

positions in a rectangular raster and by recombining them in a single synthetic digital hologram [21].

In Fig. 4 the texture of the radiator of a model car is resolved. In particular, an increase of the resolution by a factor of 2.5 in respect to the size of the CCD sensor can be expected.

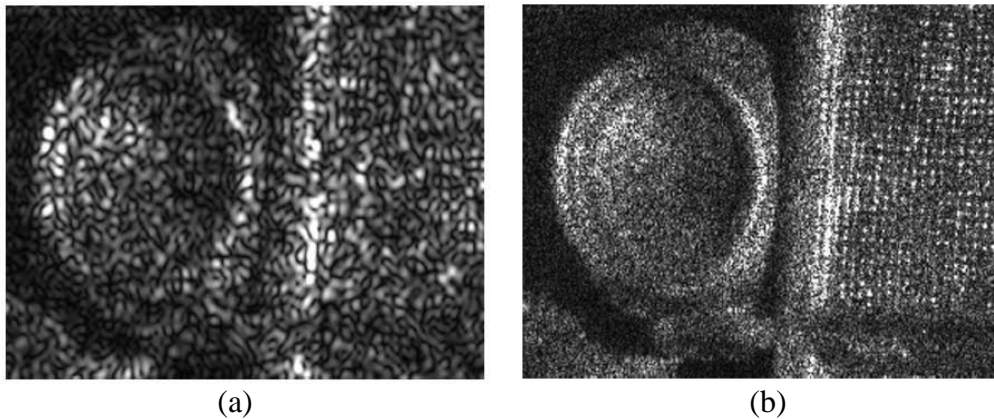


Fig. 4: Reconstruction of the object section from a single hologram (a) and from nine holograms (b) (from [21]).

Alexandrov et al. were able to break the diffraction limit by rotating the sample and recording a digital hologram for each position in order to capture the diffraction field along different directions [25]. A different approach was proposed by Kuznetsova et al. who rotated the sample in respect to the optical axis in order to re-direct the rays scattered at wider angles into the aperture of the optical system, thus going beyond its diffraction limit [26]. Mico et al. proposed and demonstrated a method for enhancing the resolution of the aperture limited imaging system based on the use of tilted illumination and common-path interferometric recording [27].

Recently, Liu et al. demonstrated that super-resolved images can be obtained simply by using the diffraction effect of an appropriate grating [22]. Essentially, their technique allows one to collect parts of the spectrum diffracted by the

object, which otherwise would fall outside the CCD array. This was achieved by inserting a diffraction grating in the recording DH set-up. The basic principle is simple but effective. In fact, the diffraction grating allows one to re-direct toward the CCD array the information that otherwise would be lost.

Basically, three digital holograms are recorded and spatially multiplexed onto the same CCD array. Super-resolved images can be obtained by the numerical reconstruction of those multiplexed digital holograms, by increasing three times the NA. The ray diagrams of the object waves are schematically shown in Fig.5 and, for simplicity, only a point object is reported.

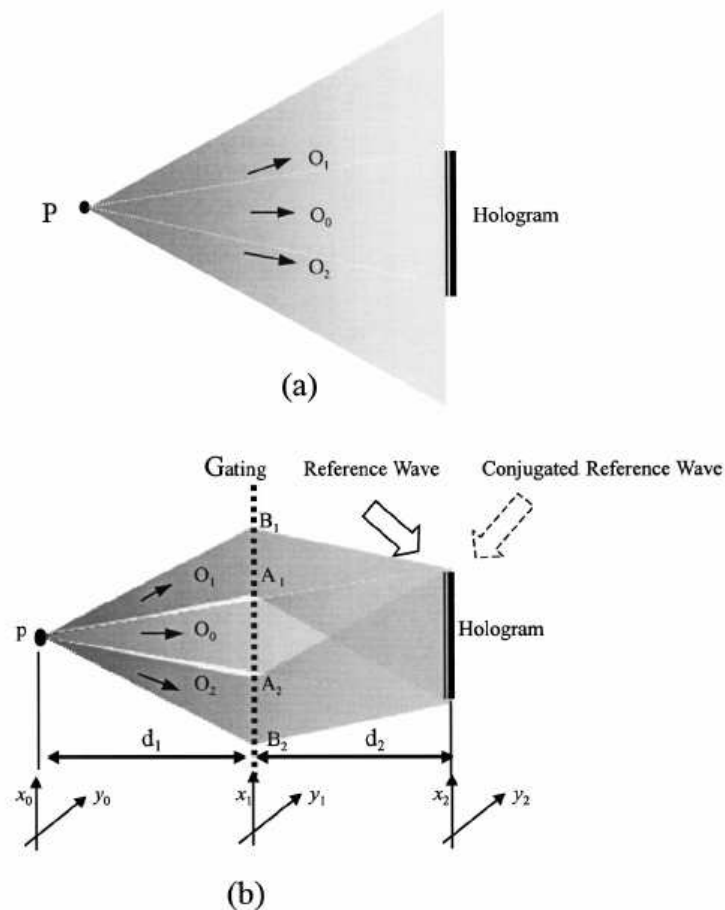


Fig. 5: Ray diagram of the object waves without (a) and with (b) a grating placed between the object and the CCD camera (from [22]).

Therefore, due to the diffraction of the grating placed between the object and the CCD camera, three beams (O_0 , O_1 and O_2) reach the area of the hologram and can be digitally recorded.

Although the working principle has been demonstrated, it is important to highlight that some limitations waited to be overcome in the approach developed in [22]. The main limitations regard the properties of the grating used for the recording process.

In the following a novel approach will be presented, where a special diffraction grating, made of lithium niobate (LN), is used. It has three important characteristics that allow one to improve the optical resolution behind the limit imposed by the recording system.

First, this grating has a two dimensional (2D) hexagonal geometry that allows one to obtain super-resolution in two dimensions. This is an important improvement compared to the technique in ref. [22], where a 1D diffraction grating was used, thus enabling to increase the NA of the recording system only along one direction, namely the direction perpendicular to the lines of the grating. Second, here a *phase* grating has been adopted, instead of the amplitude one. The main drawback of amplitude gratings is the smaller overall diffraction efficiency. In fact, only the light passing through the openings is used for imaging formation, that is only a part of the total amount of light illuminating the grating. This characteristic can turn out useful when the light gathering is critical. Third, since the phase grating, which was designed and fabricated in our laboratory, is made of an electro-optic substrate (LN), it has a tunable diffraction efficiency.

Concerning the diffraction tunability, the phase grating allows one to adjust the relative intensities of the multiplexed holograms that, indeed, depend on the diffraction efficiency of the grating itself. It will be shown that such relative intensities can affect the quality of the super-resolved image obtained by the superimposition of the reconstructed holograms. The flexible phase grating, in fact, gives one the opportunity to optimize the recording process of the

multiplexed holograms and, consequently, to improve the quality of the super-resolved images. In addition it will be demonstrated that, thanks to the flexibility of the numerical reconstruction process, it is possible to use selectively only the diffraction orders that contribute significantly to increase the spatial resolution, discarding those not carrying useful information.

2.2 The experimental set-up and the diffraction grating

The holographic set-up adopted in this experiment is shown in Fig.6. The recording process has been carried out by using a Fourier configuration in off-axis mode. The laser source is a He-Ne laser emitting at a wavelength of 632 nm. The specimen is illuminated with a collimated plane laser beam, and a spherical laser beam from a pinhole is used as the reference beam. The distance between the pinhole and the CCD is the same as that between the object and the CCD, according to the Fourier holography configuration. The CCD array has 1024×1024 pixels, with pixel size $P_{\text{CCD}} = 7.6 \mu\text{m}$.

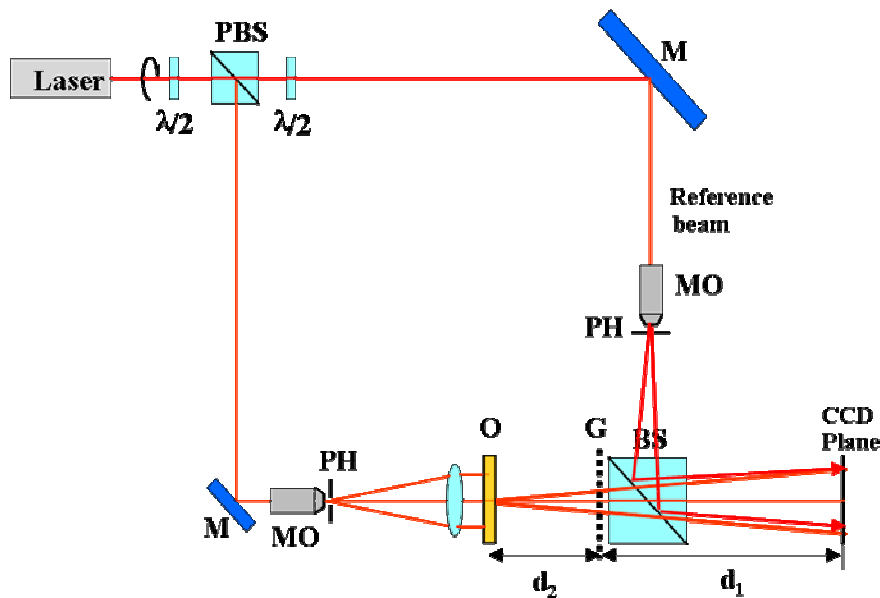


Fig. 6: Scheme of the DH recording set-up.

The **diffraction grating** G is inserted in the optical path between the object and the CCD. It consists in a 2D array of hexagonally shaped periodic reversed domains in a LN substrate. The sample has been prepared by standard electric field poling at room temperature and the distance between neighbouring hexagons is 35 μm [28-30].

After poling, transparent ITO (indium tin oxide) electrodes have been deposited on both z faces of the sample in order to apply an external field across the crystal preserving the optical transmission along the z axis.

The phase step between opposite ferroelectric domains can be varied by changing the applied voltage across the z -axis of the crystal. When no voltage is applied to the crystal, no diffraction occurs since the diffraction grating is inactive (*switched-off*). When voltage is applied, the grating becomes active (*switched-on*). It is important to note that LN has a high damage threshold over a wide spectral range, from the near UV to the IR (400 nm - 5000 nm), so that the super-resolution technique presented here could be extended to wavelengths different from that used in the present work.

One important property of this new proposed configuration is the intrinsic flexibility in terms of tunability. Because of the electro-optic effect, the phase step can be changed continuously over the entire $0-2\pi$ range by applying a variable voltage (e.g. a linear ramp). Moreover, it can be optimized for any optical wavelength within the working spectral range of the crystal.

Another very important feature of the present device, in comparison with the case of a fixed phase step, is the fine control obtainable over the step. In fact, in a conventional phase array illuminator, when the specific depth is provided by the fabrication process according to its design, it is clear that any change of temperature through the thermo-optic effect could change the refractive index of the device and consequently the phase step. In this case the phase step can be actively controlled and corrected in real time to compensate for changes in the ambient conditions.

Finally, it is important to note that the proposed configuration also shows some advantages compared with spatial light modulators based on, for example, liquid crystals. In fact, the pixel size of the device (the size of individual inverted domains) can be as small as a couple of micrometers, which is the current limit for bulk ferroelectric domain inversion with conventional methods; this value is at least two orders of magnitude smaller than the actually available spatial light modulators [31].

Hexagonally poled samples have been prepared, as said before, by standard electric field poling at room temperature. For the ferroelectric domain inversion, the z-face of a 0.5mm thick z-cut LN crystal sample has been covered with photoresist and then photolithographically patterned with a 2D array of hexagonal openings arranged in a hexagonal lattice. Fig. 7(a) shows a section of the photolithographic mask used in the fabrication process.

An external electric field of about 21 kV/mm, higher than the coercive field of the material, has been applied via conductive gel electrodes between the two opposite z faces of the crystal, while the current was monitored to control the domain inversion process (see also appendix at the end of Chap.IV). After the poling process, a 2D hexagonal lattice of domains, which is a replica of the photolithographic pattern, is created. An optical microscopy image of the actual domain structure visualized is shown in Fig. 7(b).

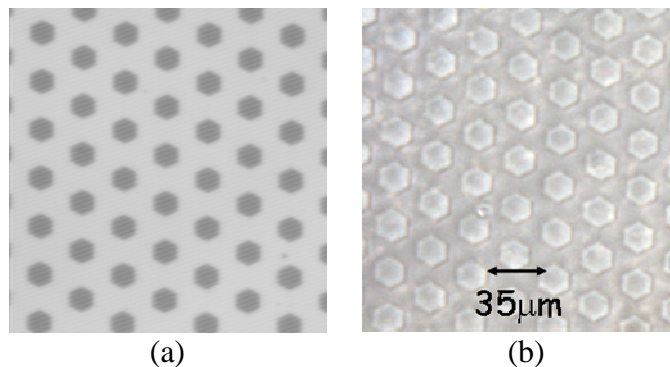


Fig.7: Optical microscopy images of the (a) photolithographic mask used in the fabrication process and (b) the actual domain structure.

The structure shown in Fig. 7(b) is very similar to the photolithography mask pattern of Fig. 7(a) in terms of the domain period. However, there is some difference between the domain inverted pattern and the mask because of sideways domain spreading during the poling process. The distance between neighboring hexagons is $35\ \mu\text{m}$ and the overall domain inverted region covers an area of about $2\ \text{cm}^2$.

Transparent indium tin oxide electrodes have been deposited on the opposite z faces of the poled crystal, as shown in Fig. 8, so that the external field could be applied across the sample without disturbing the optical transmission along the z axis.

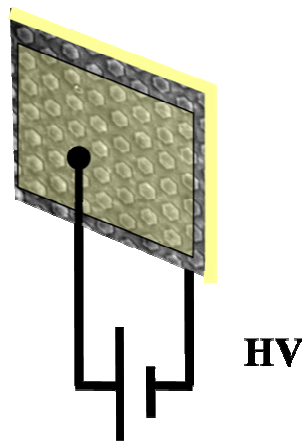


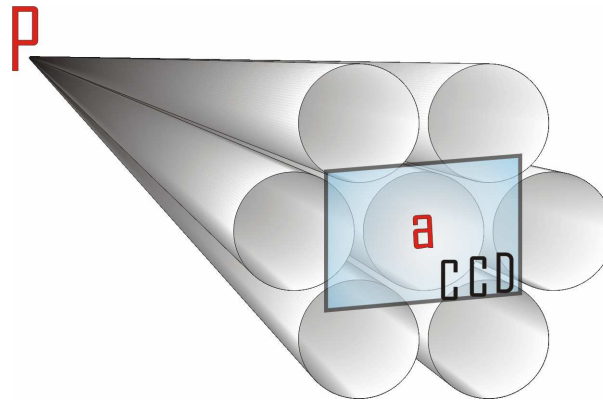
Fig. 8: Diffraction grating covered with transparent ITO electrodes.

2.3 Registration of spatially multiplexed digital holograms

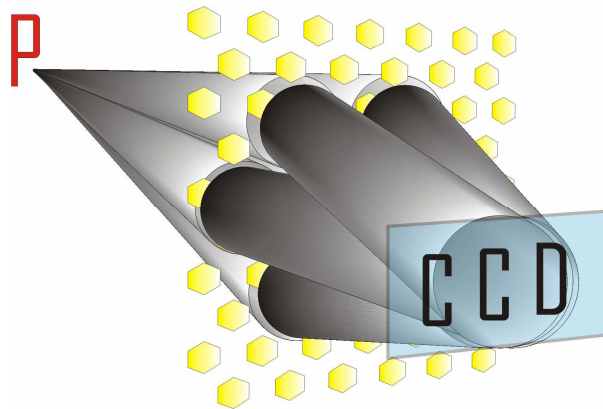
As said above, because of the electro-optic effect, the hexagonal phase array appears when the voltage is applied to the LN crystal. Whenever voltage is applied, the grating becomes active (*switched-on*). It is able to generate different diffraction orders. Essentially, each diffraction order produces a corresponding

digital hologram and all the holograms can be spatially multiplexed and recorded simultaneously by the CCD.

The schematic view of the object waves is shown in Figs. 9(a,b) where, for sake of simplicity, only one point object P is discussed.



(a)



(b)

Fig. 9: Ray diagrams of the object waves: (a) without the hexagonal grating in the set-up and (b) with the grating in the set-up.

In case of conventional holographic configurations, all the rays scattered by the object freely propagate forward to the CCD plane, but only the central ray fan reaches the area of the hologram and can be digitally recorded, as shown in

Fig.9(a). Therefore, because of the limited aperture of the CCD array, the recorded object wave beams are only a portion of the total light scattered by the object.

However, when the grating is placed between the object and the CCD array, six further fan beams waves can reach the CCD. The sketch of this configuration is depicted in Fig. 9(b). Each of the six waves are produced by the first diffraction orders of the grating. The resulting digital hologram is essentially formed by seven object beams and the reference beam. In other words, the CCD array simultaneously records seven digital holograms that are spatially multiplexed and coherently superimposed. The digital hologram has been numerically reconstructed to obtain the “in focus” real image of the tested target.

The holographic system in Fig. 9(b) clearly exhibits higher NA compared to that in Fig. 9(a). In fact, the CCD aperture augments up to three times along each of the three directions at 120°, thanks to the hexagonal geometry. Consequently, the reconstructed image of the point P has a resolution enhanced up to three times compared to the usual DH system without the diffraction grating.

2.4 Numerical reconstruction of the multiplexed digital holograms

The numerical reconstruction of multiplexed digital holograms is divided into two steps. Firstly, the wavefield in the plane just behind the grating has been obtained through the formula

$$Q(x_1, y_1) = \frac{1}{i\lambda d_2} e^{\frac{i\pi}{\lambda d_2}(x_1^2 + y_1^2)} \cdot \iint R(x_2, y_2) I(x_2, y_2) e^{\frac{i\pi}{d_2 \lambda} [x_2^2 + y_2^2]} e^{-\frac{2i\pi}{\lambda d_2} [x_2 x_1 + y_2 y_1]} dx_2 dy_2 \quad (13)$$

where $R(x_2, y_2)$ is the reference wave, while $I(x_2, y_2)$ is the intensity of the digital hologram acquired by the CCD. We assume that the grating used has a transmission function that can be written as

$$T(x_1, y_1) = 1 + a \cos(2\pi x_1 / p) + b \cos\left[\left(x_1 + \sqrt{3}y_1\right)\pi / p\right] + c \cos\left[\left(x_1 - \sqrt{3}y_1\right)\pi / p\right] \quad (14)$$

Eq.(14) is made of four terms. The first term is a constant offset. The second takes into account diffraction along the horizontal direction, while the 3rd and 4th terms consider the two other directions. In Eq.(14) p is the period of the grating, while a , b , and c are the diffraction efficiencies along the three different directions typical of the hexagonal pattern of the diffraction grating, respectively. The complex amplitude distribution at the plane immediately before the grating can be obtained by multiplying $Q(x_1, y_1)$ by $T(x_1, y_1)$; the reconstructed image in the object plane (x_0, y_0) can then be obtained by computing the Fresnel integral of $Q(x_1, y_1) \cdot T(x_1, y_1)$ according to

$$Q(x_0, y_0) = \frac{1}{i\lambda d_1} e^{\frac{i\pi}{\lambda d_1}(x_0^2 + y_0^2)} \cdot \iint b(x_1, y_1) T(x_1, y_1) e^{\frac{i\pi}{d_1 \lambda} [x_1^2 + y_1^2]} e^{-\frac{2i\pi}{\lambda d_1} [x_1 x_0 + y_1 y_0]} dx_1 dy_1 \quad (15)$$

The double-step reconstruction algorithm has been adopted to make the *reconstruction pixel* (RP) in the image plane independent from the distance between the object and the CCD, differently from what occurs in a typical single-step Fresnel reconstruction process, where $RP = \lambda d / (N \cdot P_{CCD})$. In fact, in our case, the RP only depends on the ratio d_1/d_2 , according to the formula $RP = P_{CCD} \cdot d_1/d_2$ [32]. Fixing d_1 equal to d_2 , $RP = P_{CCD} = 7.6 \mu\text{m}$. In this way, it's assured that the RP is the minimum achievable without decreasing the field of view, corresponding to the pixel size of the CCD.

As results by Eqs. (13) and (15), the double-step reconstruction is based on classical Fresnel algorithm. Recently, a novel method has been proposed to reconstruct high NA-holograms [33]. Nevertheless, the classical reconstruction

algorithm is still adopted, since in this case the super-resolved images are obtained by superimposing “a posteriori” the reconstructions of spatially multiplexed holograms rather than by reconstructing a high NA hologram.

2.5 Experimental results demonstrating the achieved super-resolution

Fig. 10(a) shows the amplitude reconstruction of the digital hologram of the object when no voltage is applied to the electro-optic grating. The object is a microscopy target with different spatial frequencies ranging from 12.6 to 100 lines/mm, corresponding to a pitch between neighbouring lines from 79.4 to 10 μm . The amplitude reconstruction clearly shows that the resolution is limited up to the maximum value of 31.6 lines/mm (31.6 μm of pitch), as evidenced by the magnified view in Fig. 10(b), while pitches of 25.1 μm and 20.0 μm are clearly below the resolution limit of the system. However, as explained in the previous section, the DH system is expected to reconstruct correctly up to the extreme limit of $2 \times 7.6 \mu\text{m} = 15.2 \mu\text{m}$, according to the Nyquist criteria (at least 2 pixels per period), and taking into account that $RP = 7.6 \mu\text{m}$. Nevertheless, the reticules with pitches below 31.6 μm are clearly unresolved due to the limited NA of the system.

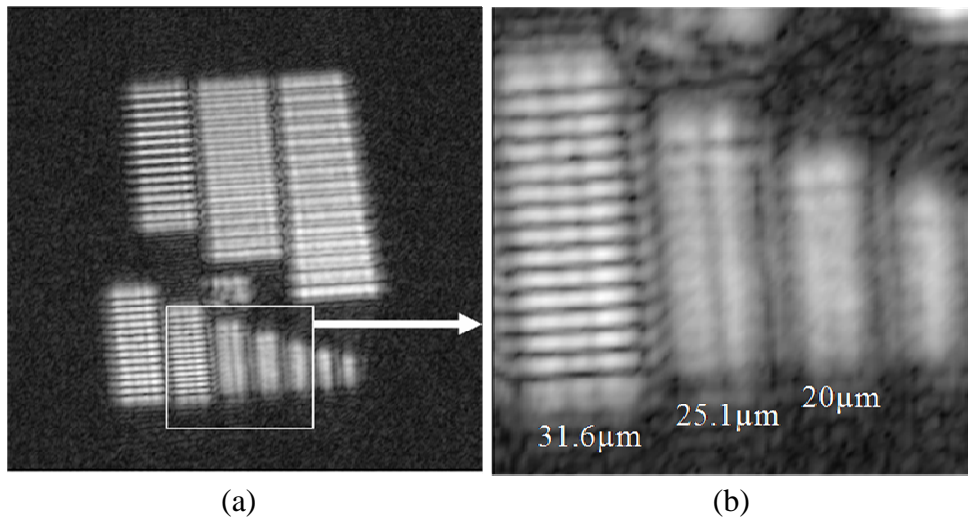


Fig. 10: (a) Amplitude reconstruction of the digital hologram when no voltage is applied to the electro-optic grating; (b) magnified view showing the lines with the shortest pitches ($31.6 \mu\text{m}$, $25.1 \mu\text{m}$, $20.0 \mu\text{m}$, $15.8 \mu\text{m}$).

When the phase grating is switched-on, seven spatially multiplexed digital holograms are recorded by the CCD array simultaneously. Fig.11 shows the amplitude reconstruction of the multiplexed digital hologram when a voltage is applied (2.5 kV in this case). The numerical reconstruction has been performed by using Eq.(15) without introducing the transmission function $T(x,y)$ of the phase diffraction grating (i.e. with $T=1$).

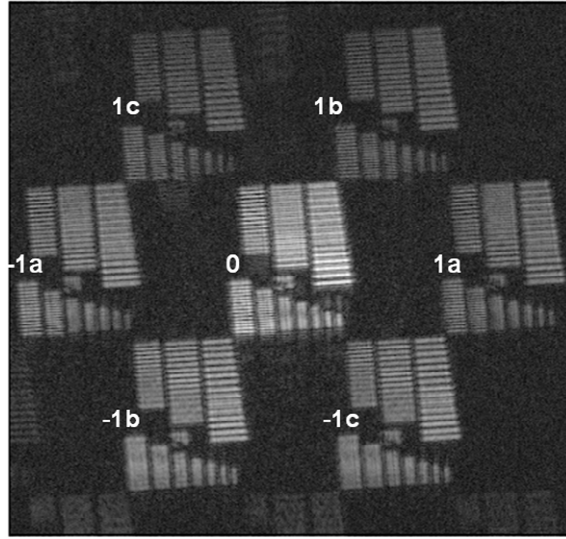


Fig. 11: Amplitude reconstruction of the multiplexed digital hologram when the phase grating is switched-on (applied voltage of 2.5 kV). This numerical reconstruction has been obtained without introducing the transmission function of the phase diffraction grating in the reconstruction algorithm (i.e. $T(x,y)=1$). The labels of reconstructed images indicate the corresponding diffraction orders.

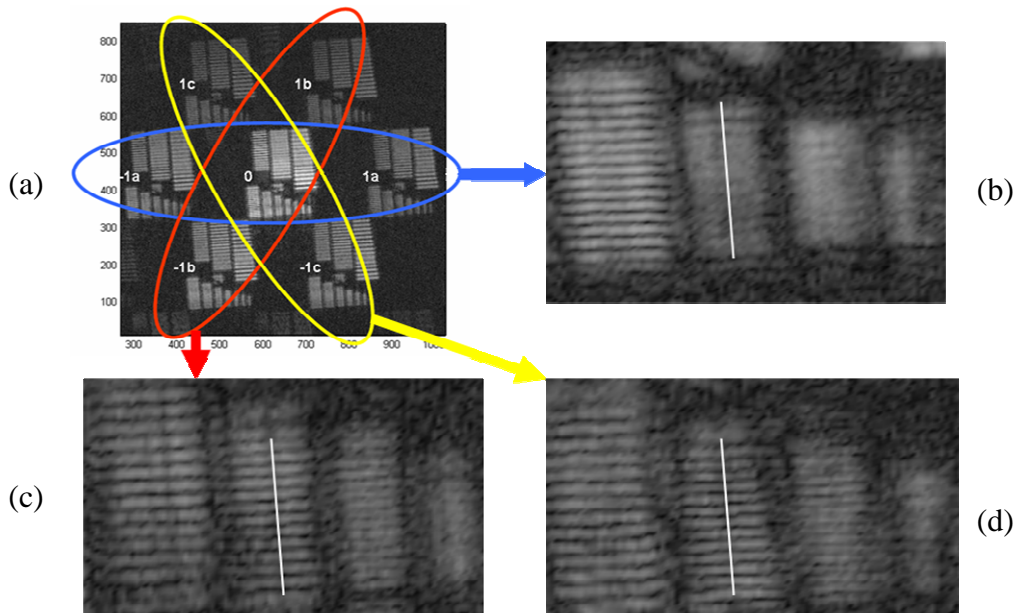
As explained before, each diffraction order produces one of the multiplexed holograms. Consequently, the reconstruction process shows up seven corresponding images, one for each of the multiplexed holograms: one for the 0th order and six for the first orders of diffraction, that are along the three typical directions of the hexagonal grating (see Fig.11).

Each couple of images along the three different directions (encircled respectively by the yellow, blue and red ellipses) in Fig. 12(a) carries different information about the object spatial frequencies spectrum. In fact, each hologram originates from the rays scattered by the object along different directions and re-directed onto the CCD area by means of the diffraction grating. It is important to point out that, without the grating (or with the grating

switched-off), the information carried by the six holograms would fall outside the NA of the CCD array and would be missed.

The resolution enhancement can be obtained only by selectively superimposing the different reconstructed images obtained by the digital holograms. In fact, in this way, it is possible to increase the NA of the optical system and therefore the optical resolution of the resulting image. It is important to note that in this case super-resolved images have been got in two dimensions, differently from what was reported in ref. [22]. This configuration reveals that the best image resolution can be obtained by using at least two diffraction directions, as shown by the following results. The superimposition of the reconstructed multiplexed holograms has been obtained automatically by using Eq.(15).

According to the particular geometry of the object, it is possible to superimpose only some of the reconstructed images that effectively possess and carry useful information with the aim to resolve the details of the object under examination. In fact, the numerical reconstruction algorithm can be considered for one, two or all of the three directions, simply assigning appropriate values to the diffraction efficiency coefficients in Eq.(14) (i.e. a , b , c , respectively).



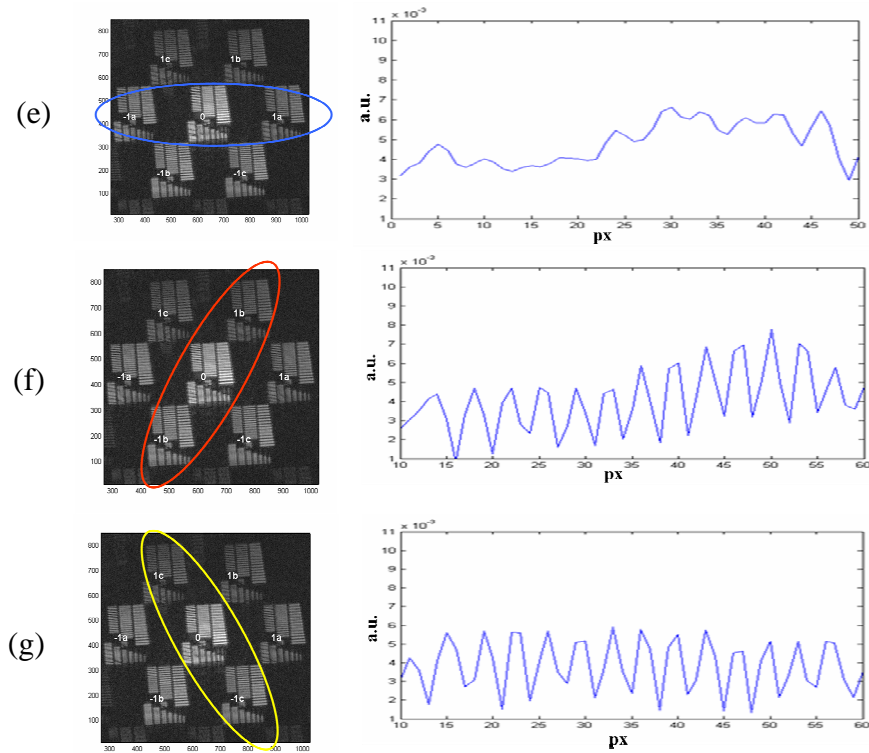


Fig. 12: (a) Coloured ellipses encircle the reconstructed images along the three typical directions of the hexagonal grating. (b-d) Magnified view of the image obtained by superimposing only the (b) -1a, 0th, +1a diffraction orders (blue ellipse), the (c) -1b, 0th, +1b orders (red ellipse), the (d) -1c, 0th, +1c orders (yellow ellipse). The reticule with a pitch of $25.1 \mu\text{m}$, completely blurred in (b), is resolved in (c) and (d) thanks to an improvement of the optical resolution.

Plots of amplitude profile along the white lines in the images (b), (c) and (d) are shown in (e), (f) and (g), respectively.

For example, Fig. 12(b) shows the magnified view of the reconstructed image obtained by superimposing the diffraction orders -1a, 0th and +1a (blue ellipse) only, that means just the horizontal direction is being considered. Differently, Figs. 12(c) and (d) show the reconstructions obtained by taking into account the -1b, 0th, +1b and -1c, 0th, +1c orders respectively, corresponding to the oblique

directions (red and yellow ellipses). Only the last two reconstructions lead to an improvement of the optical resolution allowing one to resolve the reticule with $25.1 \mu\text{m}$ pitch, otherwise completely blurred in Fig. 12(b). This is clearly evidenced by the profiles in Fig. 12(e), (f), and (g).

This result demonstrates that the collection of the rays diffracted along the horizontal direction is not useful for increasing the resolution of such target. In fact, since the rulings have only lines parallel to the horizontal direction, the rays scattered from finer rulings are directed mainly at higher angles along the vertical direction. Therefore, the object frequencies have components only along the directions of diffraction orders $\pm 1b$ and $\pm 1c$. Consequently, in order to obtain the best signal/noise ratio in the super-resolved image, the superimposition of the orders 0th , $\pm 1b$ and $\pm 1c$ without the $\pm 1a$ is more favourable.

Fig. 13(a) shows the reconstruction obtained by superimposing all of the first diffraction orders, $\pm 1a$, $\pm 1b$ and $\pm 1c$ on the zero order, while Figs. 13(c) and 13(e) show the reconstructions where the $\pm 1a$ orders (corresponding to the horizontal direction) are not considered. By comparing the reconstruction in Fig. 13(a) with those in Figs. 13(c) and (e), it is possible to notice that, involving a useless order ($a \neq 0$) in the reconstruction, only noise is added without any benefit for the resolving power. Figs. 13(b,d,f) show the profiles calculated along the ruling with a pitch of $25.1 \mu\text{m}$ for each of the corresponding reconstructed images in Fig. 13(a,c,e). The super-resolved images shown in Fig. 13(c,e) differ each other because they are obtained using two different sets of parameters in Eq. (14), namely ($a=0$, $b=2$, $c=4$) for Fig. 13(c) and ($a=0$, $b=4$, $c=4$) for Fig. 13(e).

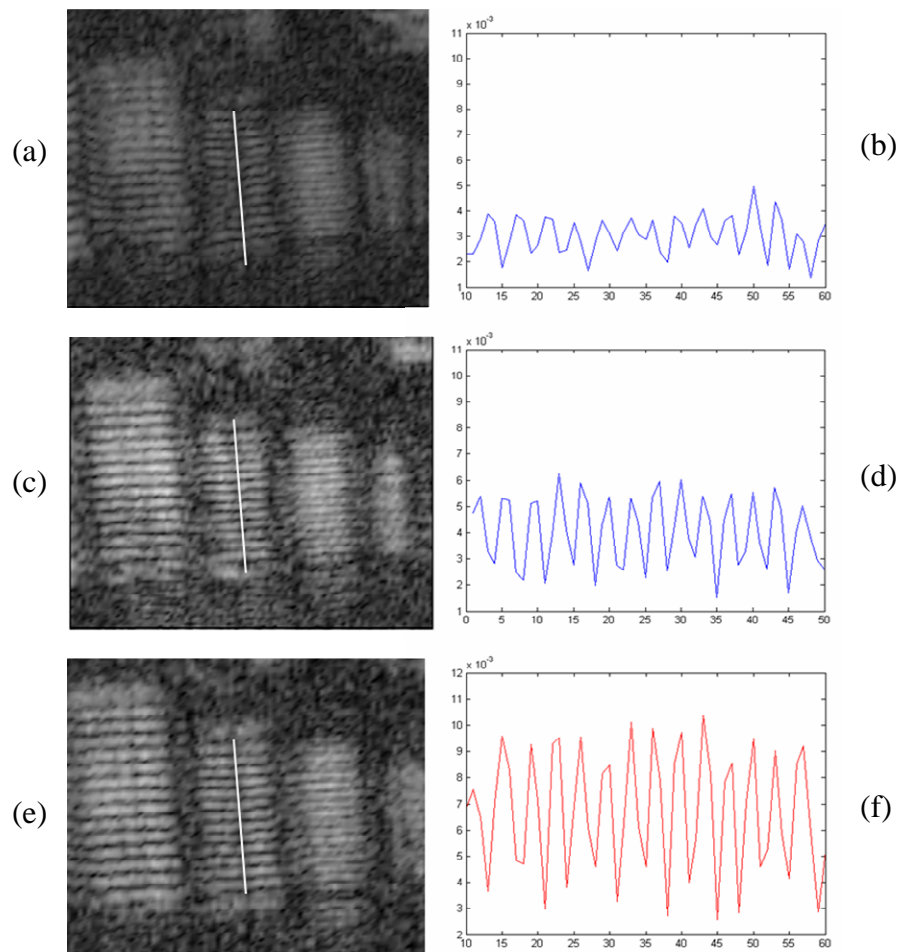


Fig. 13: (a) Amplitude reconstruction of the target obtained by superimposing all the first diffraction orders, $\pm 1a$, $\pm 1b$ and $\pm 1c$, on the 0 order; (c,e) amplitude reconstruction obtained by ignoring the $\pm 1a$ orders and by using (c) different or (e) same weight for the orders $\pm 1b$, $\pm 1c$, respectively. (b,d,f) Corresponding profiles calculated along the lines with $25.1\mu\text{m}$ of pitch. Axes of the plots have a.u. for intensities on ordinates while pixel numbers on abscissa.

The results clearly show that for the used object, the signal/noise ratio in the super-resolved image is increased when the two orders $\pm 1b$ and $\pm 1c$ have the same weight in the superimposition (see Fig. 13(e,f)). This depends on the

particular geometry of the object which has spatial frequencies all along the vertical direction, that is exactly along the bisector of the angle between the directions of the diffraction orders b and c . Therefore, the spatial frequency components along the directions of the diffraction orders $\pm 1b$ and $\pm 1c$ are the same. However, for some particular experimental conditions, the possibility to modulate the weight of each diffraction order could be useful with the aim to recover the best super-resolved image. This selective superimposition, both in terms of selected directions and weights to be assigned to each of the considered diffraction orders, is uniquely allowed by the flexibility of such numerical reconstruction process.

2.6 Influence of the diffraction efficiency flexibility on super-resolved images

In addition to the analysis and optimization of the spatial resolution through the superimposition of reconstructed images relative to different diffraction orders, it has been also studied how the dynamic properties of the diffraction grating could be exploited to improve the final result.

As explained above, the diffraction grating used in the experiment is an electro-optically tuneable phase grating. Therefore, by changing the *applied voltage* across the z -axis of the LN crystal, it is possible to tune the phase step. Consequently, the efficiency of the diffraction orders is also adjustable since it is proportional to $\sin^2(\Delta\varphi/2)$, where $\Delta\varphi$ is the phase step between inverted domains that changes proportionally to the applied voltage V . The maximum value of the efficiency is obtained for $\Delta\varphi = \pi$ ($V=2.5$ kV).

Figs. 14 (b),(d) and (f) show, respectively, the super-resolved image optimized as to the geometrical issues (i.e. with $a=0$, $b=c=4$), its magnified view concerning the reticules with the shortest pitches and the profile of the $25.1 \mu\text{m}$ pitch grating for $\Delta\varphi = \pi$ ($V=2.5$ kV). Conversely, Fig. 14 (a), (c), (e) show the same types of images for $\Delta\varphi = 3\pi/5$ ($V=1.5$ kV).

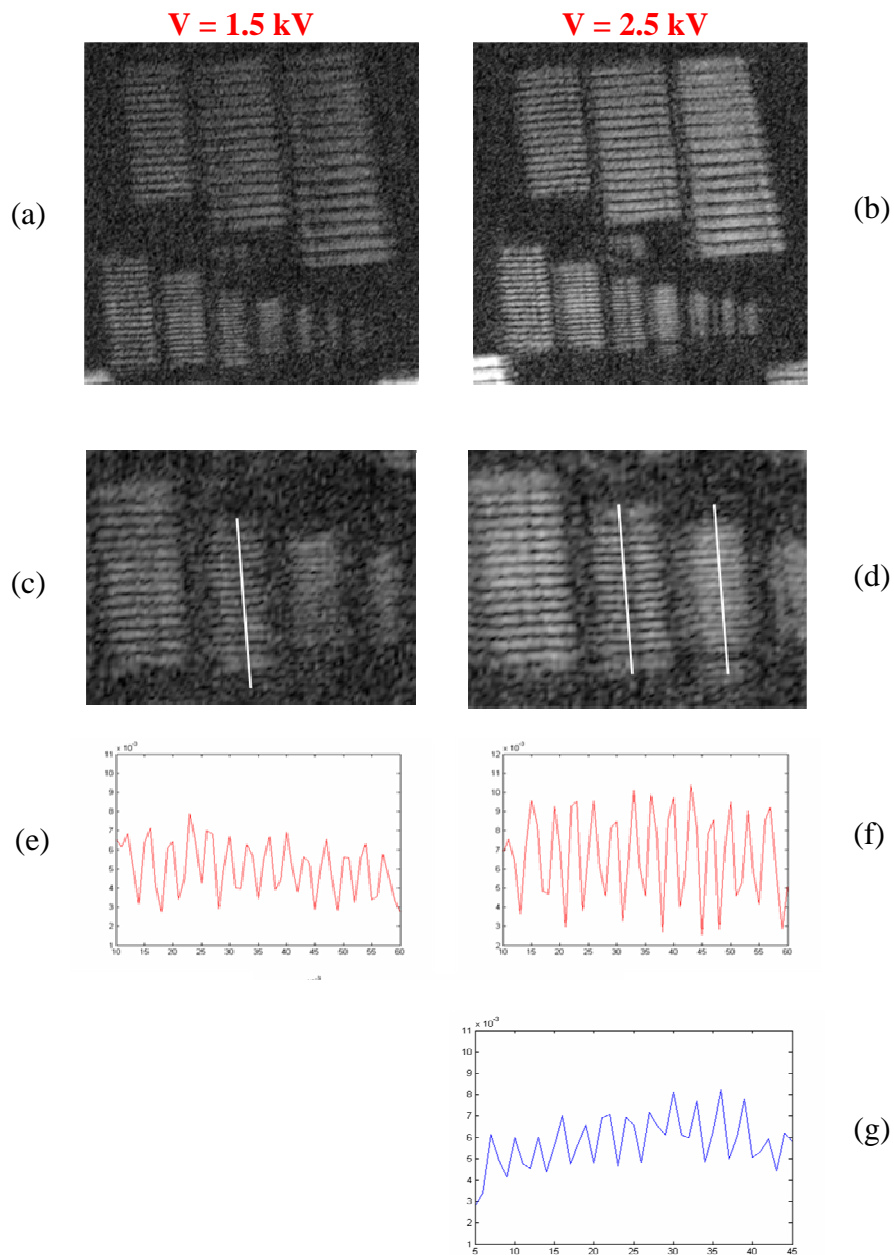


Fig. 14: (a,b) Super-resolved images optimized as to the geometrical issues, (c,d) their magnified view concerning the reticules with the shortest pitches and (e,f) profiles of the 25.1 μm pitch lines (along the white line) for $\Delta\varphi = 3\pi/5$ ($V=1.5\text{kV}$) and $\Delta\varphi = \pi$ ($V=2.5\text{kV}$), respectively. (g) Profile of the 20.0 μm pitch lines, clearly resolved for $\Delta\varphi = \pi$.

The two profiles in Fig. 14 (e), (f) clearly show that the increase of the optical resolution is higher when the phase step is $\Delta\varphi = \pi$. In fact, in this case the diffraction efficiency has the maximum possible value and therefore the images coming from the diffracted orders, containing information about the high spatial frequencies of the object spectrum, have a high weight in the superimposition process. This is a key point since, if the diffraction efficiency can be tuned, it is possible to find the best experimental condition for recording multiplexed digital holograms.

Finally, Fig. 14(g) shows also the plot of the amplitude profile for the lines with a pitch of 20.0 μm , blurred in the case of $V=1.5\text{kV}$ (see Fig. 14c), whereas resolved when $V=2.5\text{kV}$. On the basis of this latter result it can be claimed an improvement of resolution of at least 1.6.

Conclusions

It has been tried, in this chapter, to give an overview of the principle of operation and recent improvements of a quite novel interferometric technique: digital holography. Numerous examples have been reported (and will be in next chapters) of application in microscopy for inspection, characterization and investigation of different materials and processes. One of these is the enhancement of resolution, in digital holographic microscopy, achieved by means of a LN dynamic grating. In fact, super-resolution can be obtained by adopting a diffraction grating that allows one to increase the effective NA of the optical system. Up to now the proof of principle had been demonstrated only in the 1D case, limiting the resolution improvement to one single direction.

In this chapter a step forward has been presented, demonstrating that the improvement is possible in two dimensions, adopting a LN diffraction grating having an hexagonal geometry able to increase the NA along three different directions (i.e. the three directions typical of the hexagonal geometry).

Furthermore, there are two important and novel aspects in this approach. Firstly, a dynamic phase grating obtained by electro-optic effect is adopted: the diffraction efficiency can be tuned (simply by varying the applied voltage) allowing one to optimize the recording process of the digital holograms. Moreover, it is shown that, by appropriate handling of the transmission function of the numerical grating in the reconstruction algorithm, it is possible to further improve the signal/noise ratio in the final super-resolved image.

Some of the results discussed in this chapter have led to the publication of the article of ref. [24].

References:

- [1] D. Gabor: “A new microscopic principle”, *Nature* **161**, p.777–778 (1948).
- [2] K.A. Stetson, R.L. Powell: “Hologram Interferometry”, *J. Opt. Soc. Am.* **54**, p.1161 (1966).
- [3] P.K. Rastogi: *Holographic Interferometry*, Springer Verlag, Berlin, 1994.
- [4] K.A. Stetson, W.R. Brohinsky: “Electrooptic holography, its application to hologram interferometry”, *Appl. Opt.* **24**, p.3631 (1985).
- [5] J.W. Goodman, R.W. Lawrence: “Digital image formation from electronically detected holograms”, *Appl. Phys. Lett.* **11**, p.77–79 (1967).
- [6] U. Schanrs and W. Jüptner: “Direct recording of holograms by a CCD target and numerical reconstruction”, *Appl. Opt.* **33**, p.179-181 (1994).
- [7] T.M. Kreis and W. Jüptner: “Suppression of the dc term in digital holography”, *Opt. Eng.* **36**, p.2357–2360 (1997).
- [8] U. Schnars and W. Jüptner: “Digital recording and numerical reconstruction of holograms”, *Meas. Sci. Technol.* **13**, p.R85–R101 (2002).
- [9] E. Allaria et al.: “Digital Holography at 10.6 μm ”, *Opt. Comm.* **215**, p.257-262 (2003).
- [10] E. Leith and J. Upatnieks: “Microscopy by wavefront reconstruction”, *J. Opt. Soc. Am.* **55**, p.569-570 (1965).
- [11] J.W. Goodman: *Introduction to Fourier Optics*, 2nd ed. McGraw-Hill, New York, 1996.
- [12] T.M. Kreis, W. Jüptner: *Principles of Digital Holography*, in Jüptner, Osten, eds. Fringe 97, Academic Verlag, p.253–363.
- [13] L. Onural: “Sampling of the diffraction field”, *Appl. Opt.* **39**, p.5929-5935 (2000).

- [14] X. Lei, P. Xiaoyuan, M. Jianmin, A.K. Asundi: “Studies of Digital Microscopic Holography with Applications to Microstructure Testing”, *Appl. Opt.* **40**, p.5046-5052 (2001).
- [15] S. Seebacker, W. Osten, T. Baumbach, W. Juptner: “The determination of materials parameters of microcomponents using digital holography”, *Opt. Las. Eng.* **36**, p.103-126 (2001).
- [16] E. Cucho, F. Bevilacqua, C. Depeursinge: “Digital Holography for quantitative phase-contrast imaging”, *Opt. Lett.* **24**, p.291-293 (1999).
- [17] S. De Nicola et al. : “Surface topography of microstructures in lithium niobate by digital holographic microscopy”, *Meas. Sci. Technol.* **15** (5), p.961–968 (2004).
- [18] P. Ferraro, G. Coppola, S. De Nicola, A. Finizio, G. Pierattini: “Digital holographic microscope with automatic focus tracking by detecting sample displacement in real time”, *Opt. Lett.* **28**, p.1257-1259 (2003).
- [19] G. Coppola et al.: “A digital holographic microscope for complete characterization of microelectromechanical systems”, *Meas. Sci. Tech.* **15**, p.529-539 (2004).
- [20] P. Ferraro et al. : “Controlling image size as a function of distance and wavelength in Fresnel transform reconstruction of digital holograms”, *Opt. Lett.* **29** (8), p.854-856 (2004).
- [21] J.H. Massig: “Digital off-axis holography with a synthetic aperture”, *Opt. Lett.* **27**, p.2179 (2002).
- [22] C. Liu, Z. Liu, F. Bo, Y. Wang, J. Zhu: “Super-resolution digital holographic imaging method”, *Appl. Phys. Lett.* **81**, p.3143-3145 (2002).
- [23] P. Ferraro, S. DeNicola, A. Finizio, G. Pierattini, G. Coppola: “Recovering image resolution in reconstructing digital off-axis holograms by Fresnel-transform method”, *Appl. Phys. Lett.* **85**, p.2709-20711 (2004).
- [24] M. Paturzo, **F. Merola**, S. Grilli, S. De Nicola, A. Finizio, and P. Ferraro: “Super-resolution in digital holography by a two-dimensional dynamic phase grating”, *Opt. Express* **16**, p.17107 (2008).

- [25] S.A. Alexandrov, T.R. Hillman, T. Gutzler, and D.D. Sampson: “Synthetic Aperture Fourier Holographic Optical Microscopy”, *Phys. Rev. Lett.* **97**, p.168102 (2006).
- [26] Y. Kuznetsova, A. Neumann, and S.R. Brueck: “Imaging interferometric microscopy—approaching the linear systems limits of optical resolution”, *Opt. Express* **15**, p.6651-6663 (2007).
- [27] V. Mico, Z. Zalevsky, P. García-Martínez, and J. García: “Superresolved imaging in digital holography by superposition of tilted wavefronts”, *Appl. Opt.* **45**, p.822-828 (2006).
- [28] S. Grilli, M. Paturzo, L. Miccio and P. Ferraro, “In situ investigation of periodic poling in congruent LiNbO₃ by quantitative interference microscopy”, *Meas. Sci. Tech.* **19**, p.074008 (2008).
- [29] M. Paturzo et al.: “Tunable two-dimensional hexagonal phase array in domain-engineered Z-cut lithium niobate crystal”, *Opt. Lett.* **31**, p.3164-3166 (2006).
- [30] M. Paturzo et al.: “Flexible coherent diffraction lithography by tunable phase arrays in lithium niobate crystals”, *Opt. Commun.* **281**, p.1950-1953 (2008).
- [31] M.S. Millán, J. Otón, and E. Pérez-Cabré: “Chromatic compensation of programmable Fresnel lenses”, *Opt. Express* **14**, p.6226 (2006).
- [32] F. Zhang, I. Yamaguchi, L.P. Yaroslavsky: “Algorithm for reconstruction of digital holograms with adjustable magnification”, *Opt. Lett.* **29**, p.1668-1670 (2004).
- [33] F. Zhang, G. Pedrini, and W. Osten: “Reconstruction algorithm for high-numerical-aperture holograms with diffraction-limited resolution”, *Opt. Lett.* **31**, p.1633-1635 (2006).

Chapter III

Solitonic waveguides in lithium niobate

Summary

In this chapter an overview about optical waveguides properties, techniques of fabrication and materials used will be provided. In particular, I will focus on lithium niobate waveguides, as LN is a widely used material in this sense, thanks to its special properties, as explained in the first chapter.

Then the technique used in the present experiment will be described, aimed at forming a waveguide inside a crystal made of pure LN. In this case the waveguide is self-written, thanks to the photorefractive (PR) effect, by means of a spatial photorefractive soliton, that is a self-reinforcing wave propagating in space with a constant diameter.

The guide has been characterized both during its formation and after the ending of the writing process by digital holography. This technique has allowed to recover both amplitude and phase of the soliton beam exiting from the crystal, in different writing conditions.

1. Optical waveguides

An optical waveguide (OW) is a structure which confines and guides an electromagnetic field. There are different types of OWs, that differ in the

geometry adopted to confine energy: in one dimension such as *slab* waveguides, in two dimensions as fibers or *channel* waveguides (Fig.1):

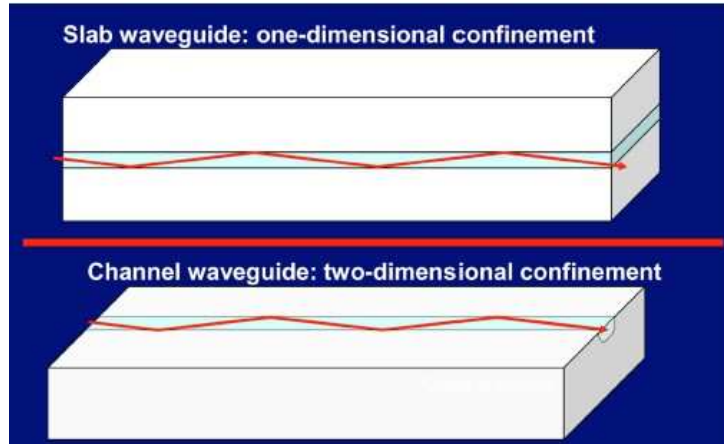


Fig. 1: Different kinds of waveguides, slab (upper) or channel (lower).

Waveguides used at optical frequencies are typically structures in which a dielectric material with high permittivity, and thus high index of refraction, is surrounded by a material with lower permittivity.

The structure guides optical waves by **total internal reflection**. This phenomenon occurs when a ray of light strikes a medium boundary at an angle larger than a particular critical angle (the “limit angle”) with respect to the normal to the surface. If the refractive index is lower on the other side of the boundary, no light can pass through and all of the light is reflected, as displayed in Fig. 2(a,b).

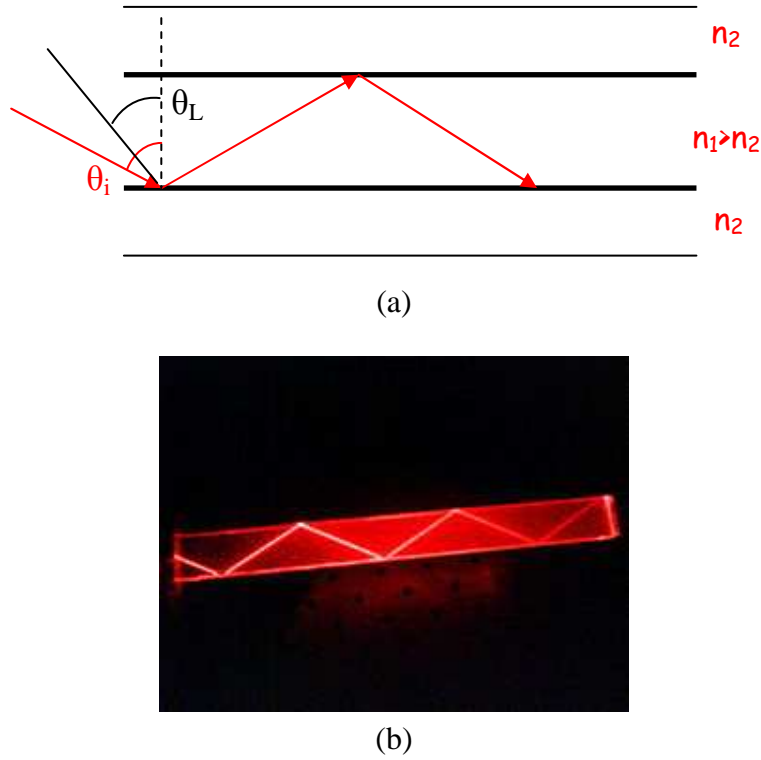


Fig. 2: (a) Scheme and (b) picture of the total reflection phenomenon.

The *limit angle* is the angle of incidence above which the total internal reflection occurs, that is, from the Snell's law:

$$\theta_i > \theta_L = \arcsen \frac{n_2}{n_1} \quad (1)$$

For example, in a typical optical fiber made of silica, n_1 (i.e. the index of the “core”) is about 1.48, while n_2 (the “cladding” index) is 1.46. So from Eq.(1) we have $\theta_L \approx 81^\circ$, meaning that the incident light must be almost parallel to the guide.

An OW is constituted of two main spatial regions: the propagating *core* and the surrounding medium. In order to confine light, as seen before, the core must have a refractive index higher than that of the surrounding medium, to ensure

the total reflection regime for the optical rays trapped inside the core area. Consequently, the propagating light proceeds inside the guide with a particular configuration, called *mode*.

According to the refractive index contrast between core and surrounding medium and according to the transverse dimension of the waveguide, one or many modes can propagate; however, the characteristic of every mode is to keep its transverse profile constant along the whole propagation length. Thus, the mode is a steady-state solution of the light propagation equation inside the confining structure.

Many techniques [1] have been developed in the past with the aim to realize such waveguide structures. Anyway, they are mainly based on two principles:

- a) Deposition of the propagating layer on a substrate;
- b) Modification of the substrate's surface in order to obtain the propagating layer.

The deposition of a layer on a substrate can be realized by many different techniques: evaporation, radio-frequency sputtering, spin-dip-coating, chemical vapour deposition and epitaxial growths by melting, by liquid or vapour-phase and by molecular beams. Among all these techniques, epitaxial growths by melting, by liquid-phase and by molecular beams [2,3] have been efficiently applied to grow **lithium niobate** films on substrates.

However, the most efficient methods for realizing waveguides in such material are those based on substrate modification, which means out-diffusion of atoms from the substrate, in-diffusion of metallic impurities inside the material, ion exchange (Li-Na, Cs-Na, Ag-Na, K-Na, Ti-Na/K) and high-energy ion implantation. Almost all of these techniques have been efficiently applied in LN, but the most efficient and used one is titanium in-diffusion. Ti ions can strongly increase the refractive index of the substrate (up to 10^{-2} ÷ 10^{-3}), penetrating for microns with concentrations up to 0.8% and with semi-Gaussian

profiles. Consequently, single-mode waveguides can be obtained by such a technique, with quite low propagation losses (0.1 dB/cm).

It must be said that each technique here described is only able to realize either planar or channeled waveguides on the top of substrates, i.e. surface structures. Historically, this is also the reason for the name “substrate”, which clearly describes the material under the structure. Integrated optical microcircuits, that are structures based on OWs, are consequently only bi-dimensional on the external surface of substrates. Some efforts have been done to bury waveguides inside the substrates: either growing on the top of the realized other layers or pushing the in-diffusion for long time in order to force the highest doping concentration deep below the external surface.

All these efforts have made possible to bury the realized structure few or tens of microns inside, anyhow far from a real three-dimensional circuit. A promising technique for real 3-D circuits is represented by **solitonic waveguides**. A soliton beam, as will be explained in the next paragraph, is a non-diffracting wave propagating in a material. The diffraction compensation is ensured by a local modification of the refractive index of the medium induced by light-excited electric-charge distribution (the so called “photorefractive effect”). Such charge distribution, via the electro-optic effect, “writes” a light confining structure.

With respect to the previous techniques, many advantages can be identified in this case, making solitonic waveguides very attractive for applications:

- a) The guiding structure can be written everywhere in the volume of the host material (I don't speak anymore of substrates but “host materials”), giving a perfect 3-D structure;
- b) The associated waveguide is perfectly symmetrical, allowing always at least one mode to propagate inside, with very low propagation losses (<0.1 dB/cm), being the refractive index profile self-written by a non-diffracting light beam;

c) Solitons can live for long time after the writing procedure, and the writing technology is very simple and low costly (the writing beam should have powers of the order of μW or mW).

According to the initial focusing of the writing light, the associated waveguide can be planar, channeled or conical, in fact also not-completely formed solitons are able to modify the material's refractive index, realizing conical stigmatic structures.

The guide characteristics depend on the writing procedure; according to the writing wavelength different dimensions can be obtained, ranging from 18-20 μm at FWHM for red light down to 6-8 μm for blue light. The refractive index profile might be either Gaussian (for short time formation) or hyperbolic secant (for long time formation), with a total variation ranging between 10^{-4} and 10^{-6} . Such low refractive contrast guarantees that also large structures may behave as single-mode waveguides.

2. Photorefractive soliton formation in a lithium niobate crystal

2.1 *Introduction: what is a soliton?*

In this paragraph a systematic study of the relevant features of the optical soliton formation process inside a nonlinear medium is presented, by analyzing the parameters that influence formation times and dynamics.

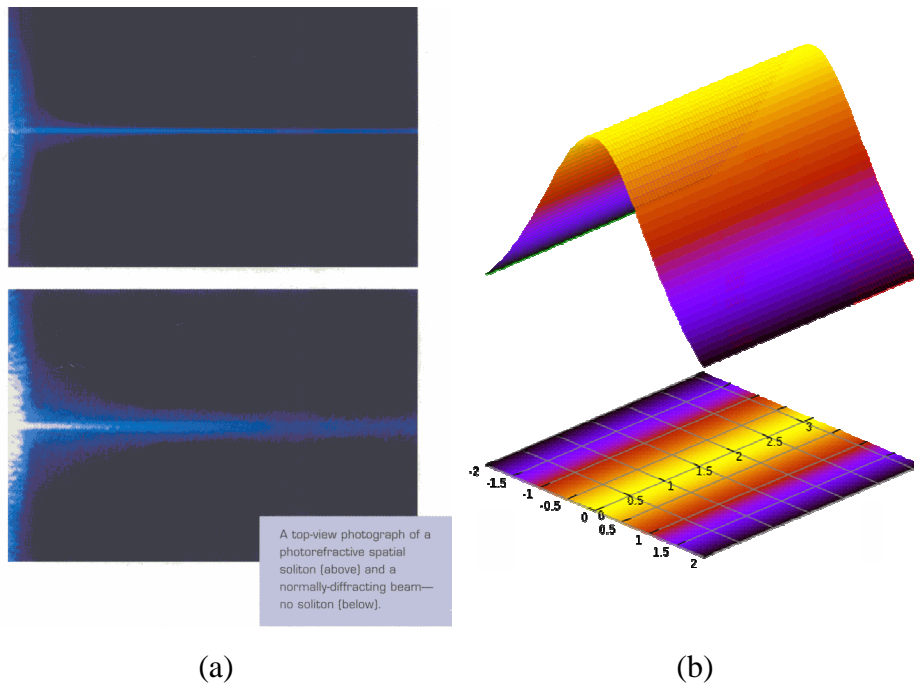
A **soliton** is a self-reinforcing solitary wave (a wave packet or pulse) that maintains its shape while traveling at a constant speed [4]. However, a single, consensual definition of a soliton is difficult to find. Drazin and Johnson (1989) ascribe three properties to solitons:

- 1) They are of permanent form;
- 2) They are localized within a region;
- 3) They can interact with other solitons and emerge from the collision unchanged, except for a *phase shift*.

The first documented report of a soliton was in 1834 when a Scottish naval engineer, John Russell, observed a water wave in a canal propagating “*without change of form or diminution of speed*”, that he called “*Wave of Translation*” [5]. During the following years, similar phenomena have been observed in many physical systems: charge density waves in plasma, phonons in solids, excitations on DNA chains, “branes” in superstring theory, and others.

In optics, solitons were predicted for the first time in the 1970s [6] and then observed in 1980 [7]. These kind of solitons were the so called *temporal solitons*, i.e. temporally localized pulses of light, and are now being considered as a possible candidate for long distance optical communication systems [8,9]. On the other hand there are *spatial solitons*.

It is well known that an optical beam propagating in a homogeneous medium tends to broaden in space because of diffraction [10]. However, in a nonlinear optical medium, the diffraction effect can be compensated by the perturbation of the refractive index induced by the nonlinear interaction between the light beam and the medium. The beam can be self-trapped and thus propagates inside the medium with a constant diameter: this is known as an *optical spatial soliton* (Fig. 3).



A top-view photograph of a photorefractive spatial soliton (above) and a normally-diffracting beam—no soliton (below).

Fig. 3: (a) Photo of an optical spatial soliton (above) and in comparison of a normally-diffracting beam, from right to left (below). (b) Simulation of a spatial soliton propagating with uniform shape (from [4]).

Spatial solitons manifest themselves in a large variety of settings and in recent years have become the object of intense studies [6,7,11-15].

There are mainly three kinds of optical spatial solitons that have been demonstrated experimentally. The first discovered were the *Kerr solitons* [11,12], originated from a third-order electronic susceptibility process that gives rise to the optical Kerr effect, which can be described by an intensity dependent index of refraction. A second type was discovered in the 1970's: the *quadratic soliton* [13-15]. It cannot be interpreted as originating from a modification of the medium's refractive index, but self-trapping occurs as a result of rapid exchange of energy among beams at different frequencies, mediated by the second order nonlinearity of the medium.

The last type of spatial soliton was discovered in 1992, when Segev et al. predicted that PR media could support a new kind of soliton, in which diffraction was balanced by focusing effects caused by a light-induced index change. The latter was named **photorefractive soliton** [16-18].

The first PR soliton that was investigated originates from the non-local nature of the PR effect and was named *quasi-steady-state soliton* [19]. Another type of PR soliton can be realized in photovoltaic materials (*photovoltaic soliton*), where the internal photovoltaic field provides the necessary drift effect of the optically-induced free-charge carriers [20,21]. One more interesting kind of PR soliton is known as *screening soliton* that, differently from the case of the photovoltaic one, requires an external electric field to be applied across the crystal along the transverse direction in respect to the optical propagation direction. The external field is applied in order to drift the free charge carriers [22-26].

The attractive property of screening solitons is the very low laser power that is necessary for their generation. This permits investigation of these objects with conventional continuous-wave laser sources and, consequently, the development of realistic applications to waveguiding thanks to the easy availability and relatively low cost of the experimental devices.

PR screening solitons have been the object of extensive research in the last years, because of the richness of PR effects that invites experimental investigations into a large variety of soliton phenomena. First experiments were performed on strontium barium niobate (SBN) [27], and then in many other materials, such as KTN, BGO, BTO, BaTiO₃, polymers, ecc. Among nonlinear materials, LN has been demonstrated to be very suitable for the generation and propagation of screening solitons [28,29], owing to its high electro-optic and non-linear coefficients (see Chap.I), and also to its remarkable photovoltaic, piezoelectric and PR properties.

One of the most interesting feature of these solitons is that they can be guided inside the host medium by the refractive index perturbation created by their

passing-through it [22,30,31]. So it is possible to use solitons for optical waveguides generation and characterization by means of a low power continuous-wave laser.

Waveguides in LN were first demonstrated by *dark* screening solitons (defocusing case), that are dark shadows propagating without diffraction in a light background [20,21,32], but it has been shown that *bright* screening solitons (self-focusing case) are much more stable and suitable for waveguiding [28,33].

Even though in the last few years photorefractive screening solitons have given rise to a great interest, the formation and evolution mechanisms are not completely clear yet. Experiments discussed in this paragraph represent an effort to contribute to a deep understanding of these processes. The effective changes of the refractive index of the crystal during the writing process and after the soliton formation are obtained by determining the phase distribution of the optical wavefront at the exit face of the crystal. The phase analysis provides a way to control and monitor the process of soliton formation more reliable than the evaluation of the sole intensity distribution of the output beam. Such kind of investigation is made possible from the unique feature of digital holographic (DH) technique. In fact by means of this interferometric technique it is possible to reconstruct and manage the whole optical field (i.e. complex field in amplitude and phase, see also Chap. II) of the soliton beam [34].

The basic parameters that influence the process of soliton formation are the intensity of the writing and of the background beams and the value of the applied electric field. Both static and dynamic analysis of the soliton generation process has been performed. The static analysis, discussed in par. 2.3, concerns a great number of screening bright solitons, each created with a particular writing intensity or with a different value of the external electric field. By means of DH it has been possible to compare intensity and phase features of these solitons, at the exit face of the sample, generated with different writing parameters. The dynamic measurements (par. 2.4-2.5) deal with the soliton

temporal behavior, starting from the beginning of the formation process till one month after the solitonic waveguide complete creation. DH has allowed to retrieve temporal evolving profiles for both intensity and phase of the beam at the exit crystal face, starting from a sequence of holograms recorded at different instants of time.

2.2 Experimental set-up and procedures

The experimental set-up utilized for the study and characterization of the soliton writing process is a Mach-Zehnder interferometer where the sample is placed in a transmission configuration (Fig. 4(a,b)). The source is an Argon ion laser emitting a light beam with $\lambda = 514$ nm, that is splitted in two beams: the object and the reference beam. The object one, that is the writing beam for the waveguide and propagates along the x-axis, is focused down to a beam waist at $1/e^2$ of 30 ± 5 μm (corresponding to a Rayleigh length of 12 ± 4 mm) on the input face of an undoped z-cut lithium niobate crystal (Altechna Co. Ltd.), with dimensions of 7x20mm along the x and y directions, respectively, and thickness $d = 1$ mm along the z-axis. The sample is electrically biased along its crystal optical axis z; the role of the applied field is to start up the charges drift that produces, by means of the electro-optic effect and together with the passing through of the writing beam, the refractive index variation necessary to the waveguide generation [28].

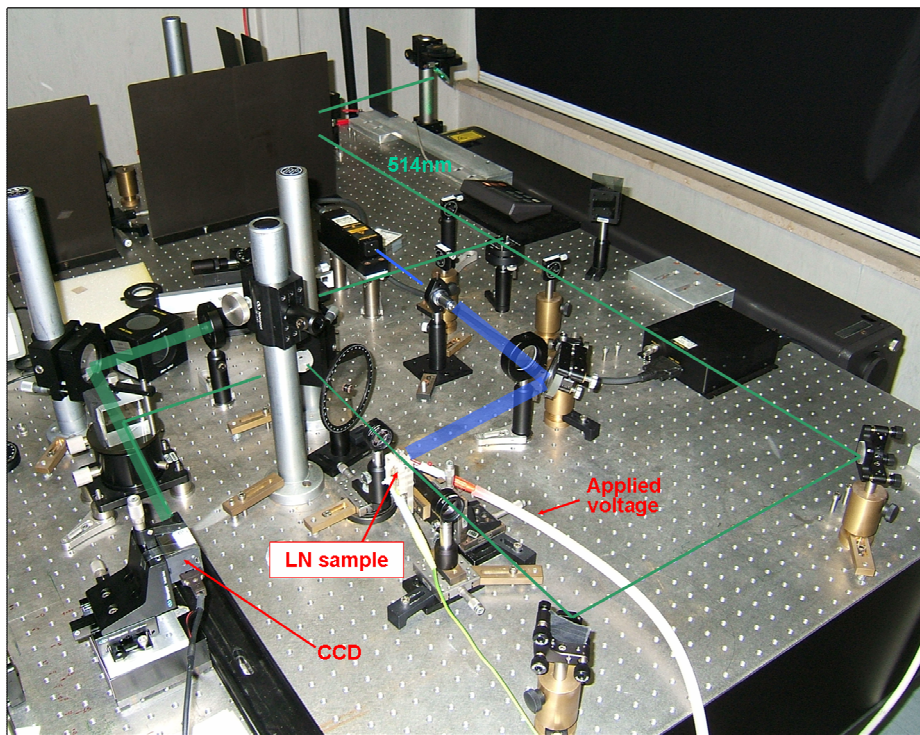
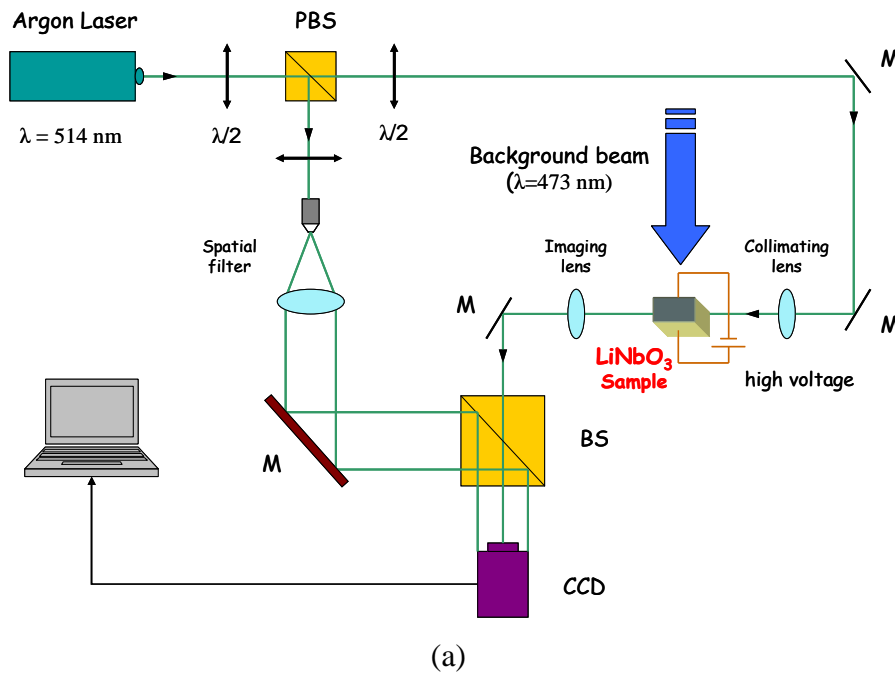


Fig.4: (a) Scheme and (b) photo of the experimental set-up used for the characterization of the solitonic waveguide writing process.

After propagation inside the medium, the exit beam is imaged by a biconvex lens and then recombines with the reference beam (a plane wave) on the CCD camera (pixel size = $4.4\mu\text{m}$), that is placed at a distance $d = 15\text{cm}$ from the image plane. The recorded interference pattern is the *digital hologram* (see Chap.II). Both writing and reference beams are linearly polarized with an angle θ that can be varied (but not in the present experiment) by a $\lambda/2$ plate, from the horizontal z direction to the vertical y (as depicted in Fig.5(b)). Besides, a background non-polarized light beam from a diode laser ($\lambda = 473\text{ nm}$), with an intensity $I_b = 2\text{ mW/cm}^2$, impinges on the x - y face of the crystal (see Figs. 4 and 5(b)) along the z -axis and uniformly illuminates the sample in order to enhance the PR effect.

A plenty of interferometric fringe patterns have been recorded, varying several writing parameters. The amplitude and the phase of the complex wavefields at the exit crystal face have been numerically calculated starting from these digitally recorded *object holograms*. The phase distribution contains all the contributions due to the optical aberrations introduced by optical elements present in the set-up. To compensate such aberrations it has been necessary to record another hologram, named the *reference hologram*, that is the result of interference between the reference beam and the object one just before the electrical bias field was switched on, i.e. before the actual beginning of the writing process [35,36]. The phase map of the solitonic wavefront has been obtained as the difference $\Delta\varphi$ between the phase calculated from the object hologram and the one calculated from the reference one.

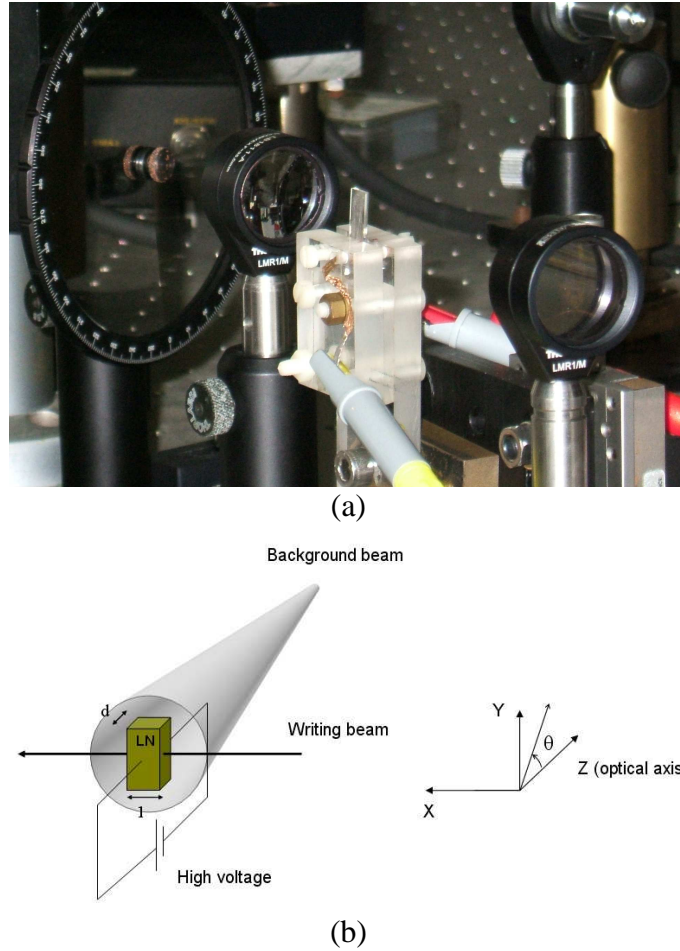


Fig. 5: (a) Close-up of the LN sample mounted on a plexiglass holder. (b) Coordinate system adopted.

2.3 Steady-state features of the soliton formation process

Using the experimental set-up shown in Fig.4, with a constant external applied electric field $E_0 = 3.5 \text{ kV/mm}$, and taking also constant the background beam at 2 mW/cm^2 , a set of measurements has been performed, varying the power P (i.e. the intensity I) of the incident z-polarized beam, whose diameter at the entrance face of the sample was about $60 \text{ }\mu\text{m}$.

Fig. 6 shows the intensity maps and profiles of the reconstructed wavefield along the y and z crystal axes, calculated at the output face of the crystal.

Measurements have been carried out with different powers of the writing beam, ranging from $10\mu\text{W}$ to $370\mu\text{W}$ (corresponding to $180 \leq I/I_b \leq 7000$). Fig. 6(a) shows the intensity map of a soliton generated with an incident power of $25\mu\text{W}$, while in Figs. 6 (b,c) all the intensity profiles along y (b) and z axes (c) are displayed. Experimental data have been also fitted with the squared-hyperbolic secant theoretical curve [28]: Figs. 6 (d,e) show the fitted curves corresponding to Fig. 6(a), i.e. to a writing power of $25\mu\text{W}$.

From the **intensity analysis** (Fig. 6) we notice that the soliton regime has been always achieved, both along y and z axes, and this is in agreement with other experiments performed on different materials such as BTO [37] and SBN [27]. However, with the increase of the writing power, the time required for the soliton generation becomes shorter. Fig.7 shows the solitonic waveguide formation time for different values of the writing beam power; the experimental points are fitted well by an inverse intensity $a/(b+P)$ law, with a and b constants. For higher powers (higher than that considered) this expression should be revised taking into account also thermal and other effects [18,33,38,39].

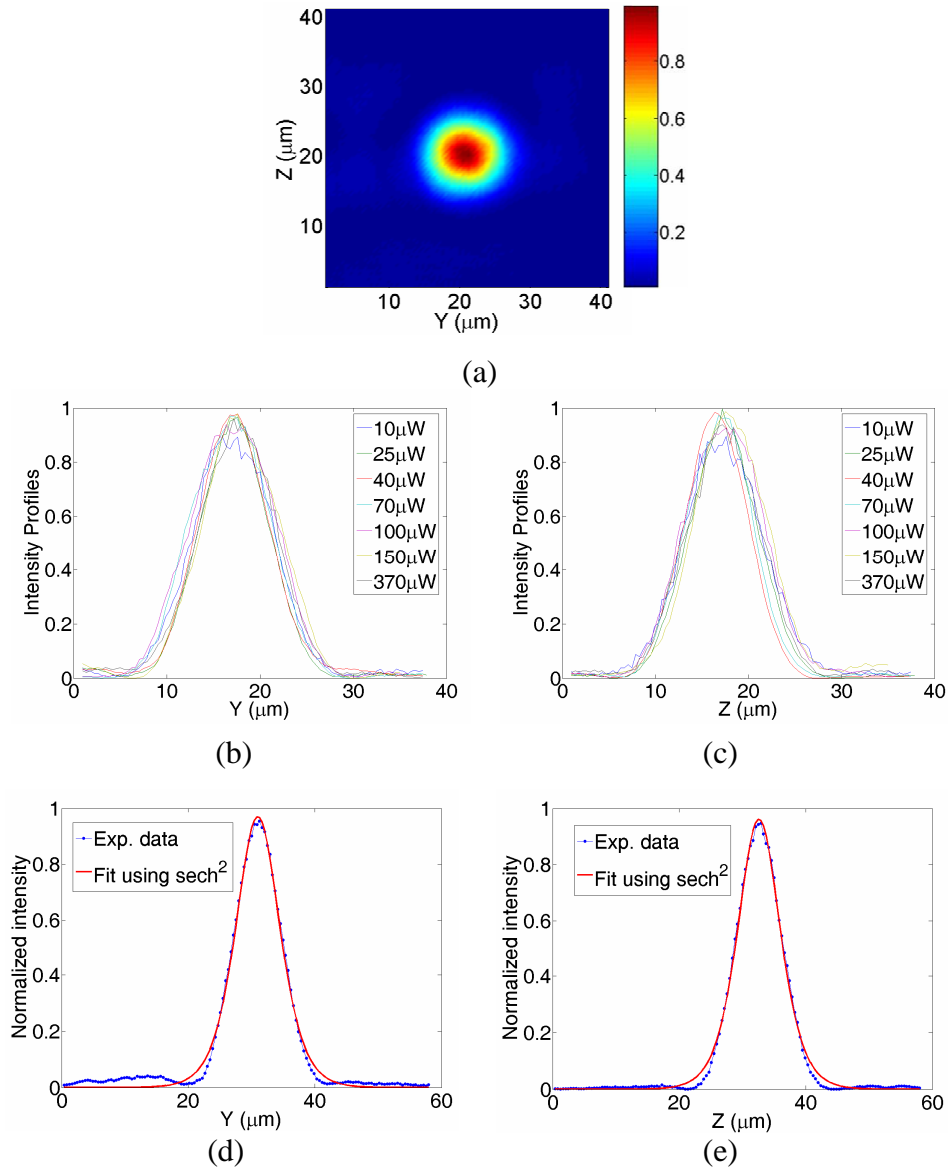


Fig. 6: (a) Intensity map of a soliton beam generated with a writing power of $25\mu\text{W}$. (b-c) Intensity profiles along y (b) and z (c) axes. Experimental data (blue lines) regarding the writing power of $25\mu\text{W}$ are fitted with a squared-hyperbolic secant (red lines) along y (d) and z (e).

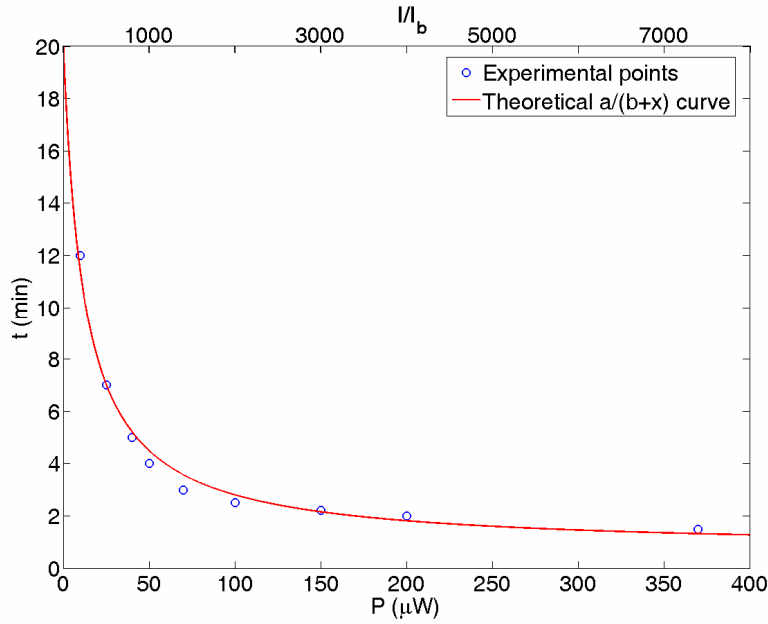


Fig. 7: Solitonic waveguide formation time for different values of the writing beam power; experimental points (blue circles) are fitted with an inverse intensity $a/(b+P)$ law (red line).

The **phase analysis** of the complex wavefield at the exit crystal face gives a further confirmation of the correctness of the intensity study and gives additional information about the solitonic waveguide characteristics.

Fig. 8 shows the phase profiles of the soliton output beam along the y and z -axes. We can see that, in the whole explored power range, the phase and consequently the refractive index values quickly change from the outside to the interior of the waveguide ($\Delta n \approx 2.4 \cdot 10^{-5}$), confirming that a solitonic waveguide has been created [38]. In fact, in Figs. 8 (a-c) phase profiles along both axes, for incident powers of $70 \mu\text{W}$, $100 \mu\text{W}$ and $150 \mu\text{W}$, are shown, in each figure the phase distribution being displayed as inset. We notice that for power values between 70 and $150 \mu\text{W}$ (I/I_b ranging from 1200 to 2700) the refractive index along the transverse section of the waveguide is approximately flat across the soliton section.

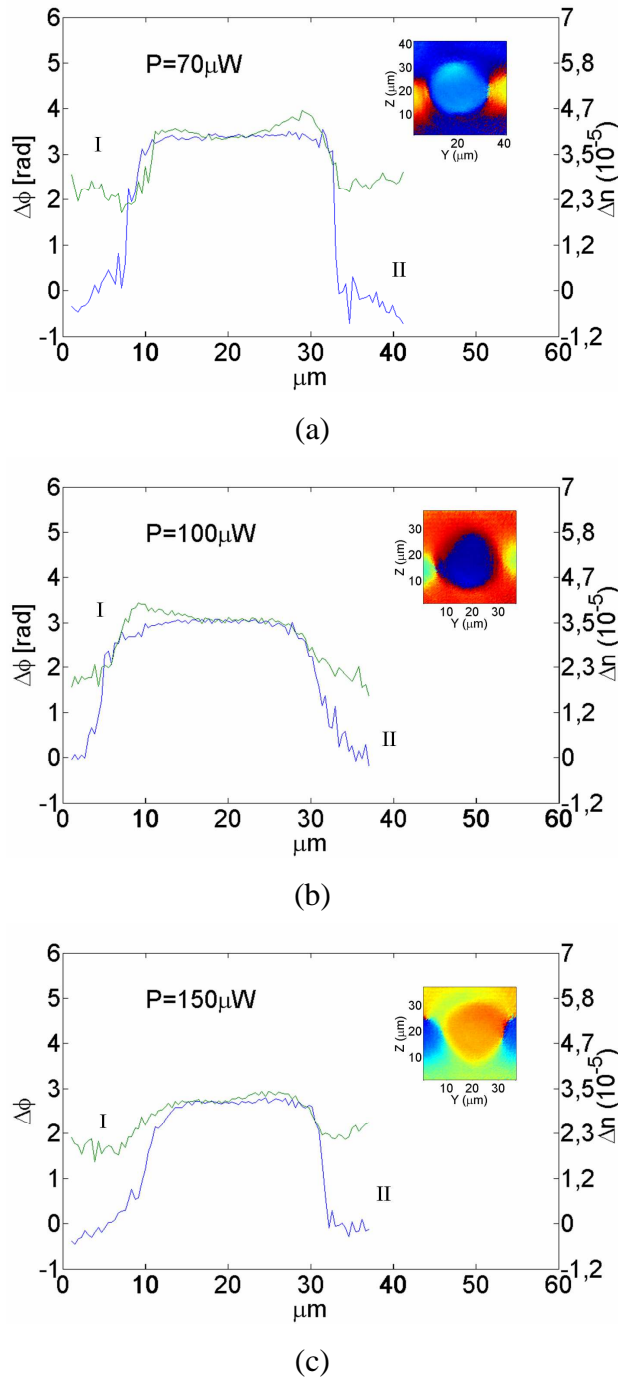


Fig. 8: Phase profiles along y (blue line, II) and z (green line, I) axes, for incident powers of $70\mu\text{W}$ (a), $100\mu\text{W}$ (b) and $150\mu\text{W}$ (c). Phase distributions are displayed as insets.

On the contrary, for powers lower than $70\mu\text{W}$ and higher than $150\mu\text{W}$, the index profiles show a pronounced concavity. To put better in evidence the phase profile's shape of the soliton wave in this range of writing powers, in Fig.9 a zoom of the profiles along y and z-axes has been reported, corresponding to the more internal part (i.e. the core) of the waveguide, for writing powers of 25 (a,b), 200 (e,f) and $370\mu\text{W}$ (g,h), and in comparison of $70\mu\text{W}$ (c,d).

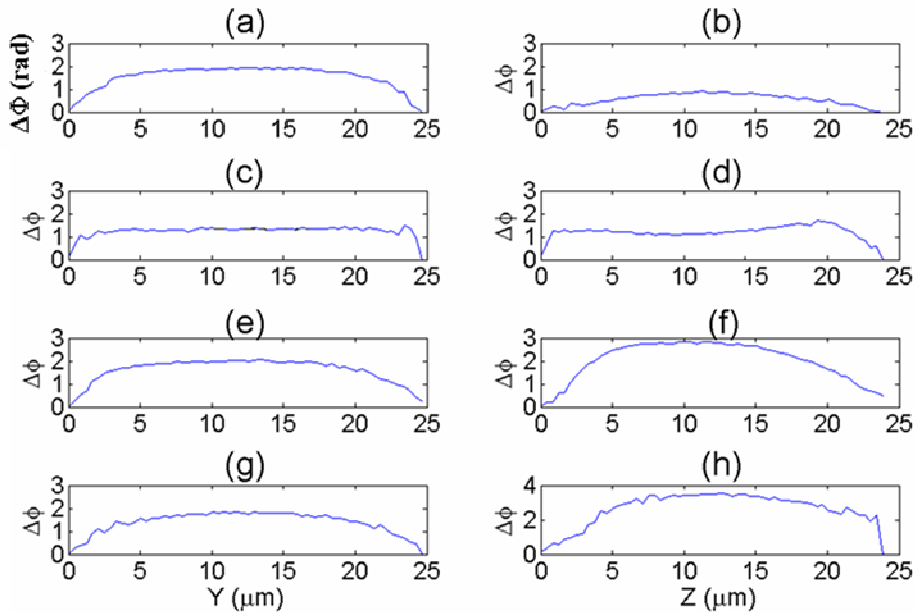


Fig. 9: Partial phase profiles along Y (a,c,e,g) and Z (b,d,f,h) for solitons formed by different writing powers: $25\mu\text{W}$ (a,b), $70\mu\text{W}$ (c,d), $200\mu\text{W}$ (e,f), $370\mu\text{W}$ (g,h).

On the basis of the results shown in this figure it can be taken into consideration the analogy with terms like “step-index” and “graded-index” perturbation created by the soliton beam. The depth of the concavity ranges from 0.8 rad (for $25\mu\text{W}$) up to 3.8 rad (for $370\mu\text{W}$), corresponding to a variation in the refractive index of $0.9 \cdot 10^{-5}$ and $4.4 \cdot 10^{-5}$ respectively ($\Delta\phi = l \cdot \Delta n \cdot 2\pi/\lambda$, with $l=7\text{mm}$), while for $70\mu\text{W}$ (Figs. 9(c,d)) the concavity is much less evident. So it

seems that it is possible, simply varying the writing power, to generate different kinds of optical waveguides. This observation has not been reported previously because only an interferometric technique can measure the refractive index with enough accuracy to detect it. The latter results and corresponding experimental observations will be object of future work to understand in which way the differences in the writing power affect the creation of one kind of waveguide instead of another.

In a further series of interferogram analyses the incident beam power has been fixed at about $70\mu\text{W}$ ($I/I_b \approx 1200$), and the electric bias tuned from 1 kV/mm up to 3.5 kV/mm. Figs. 10(a-f) show different intensity (a-c) and phase (d-f) distributions obtained for different values of the external applied field.

To better highlight the differences among the diverse situations, in Figs. 11(a,b) the reconstructed intensity beam profiles along y (a) and the corresponding output beam diameters (b), versus the electrical bias, have been plotted, whereas Figs. 12(a-f) show the phase profiles along the y and z directions.

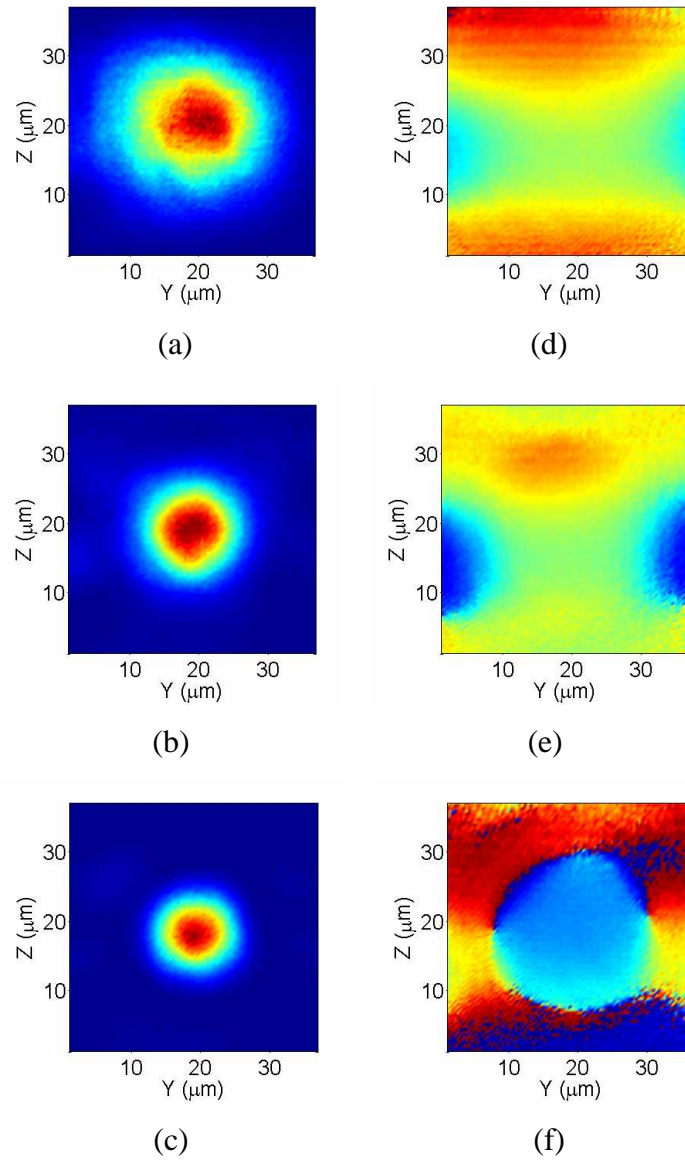
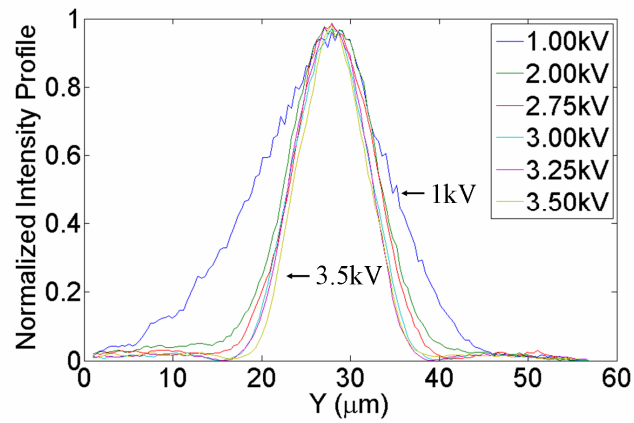
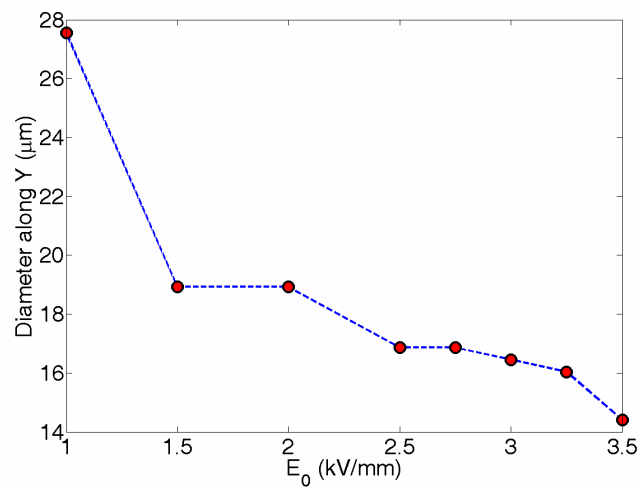


Fig. 10: Intensity (a-c) and phase (d-f) distributions of the optical beam at the exit face of the crystal obtained with an external applied voltage of 1.0 kV (a,d), 2.0 kV (b,e), 3.5 kV (c,f).



(a)



(b)

Fig. 11: (a) Reconstructed intensity beam profiles along y with varying the electrical bias; (b) corresponding output beam diameters. The dotted line is only a guide for the eye.

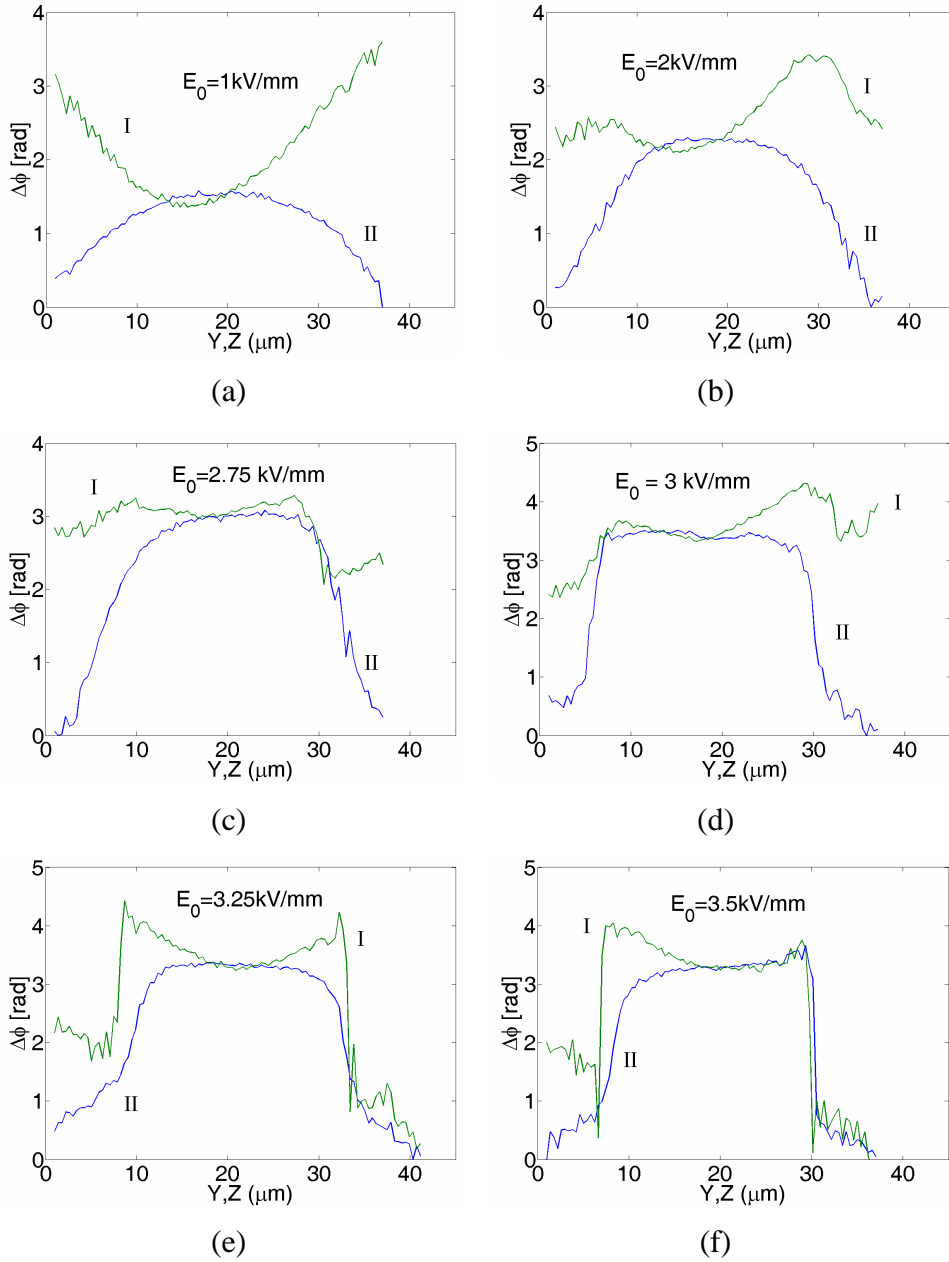


Fig. 12: Phase profiles along y (blue line, II) and z (green line, I) for different applied voltages: 1 kV (a), 2 kV (b), 2.75 kV (c), 3 kV (d), 3.25 kV (e) and 3.5 kV (f).

This time there is an optimal experimental condition to create an optical waveguide, by means of PR screening bright solitons. This condition corresponds to the application of an external electric field higher than about

3kV/mm to compensate for diffraction, but lower than 3.6 kV/mm to avoid “over-focusing” and/or the dielectric breaking of the sample (see also ref.[16,27,28,37]). In this intermediate region the phase profiles along y and z directions become more or less constant after a sharp rise corresponding to the edge of the waveguide, confirming a clear step-index-like refractive index perturbation. This information coming from the phase is fundamental because from a sole intensity analysis is not always clear whether the waveguide has been created or not.

2.4 Temporal evolution

Making use of the Mach-Zehnder shown in Fig.4, the time behavior of the optical beam propagating inside the LN sample has been investigated.

In Fig.13 a sequence of the frames (in intensity) corresponding to the soliton formation is displayed, using an incident power of about 70 μ W and an applied electric field of 3.5 kV/mm, switched on at $t = 0$ (first frame). On the basis of the previous results obtained in static conditions, this corresponds to the optimal configuration for a waveguide formation inside the material considered.

The whole duration of the soliton formation process is about 4-5 minutes.

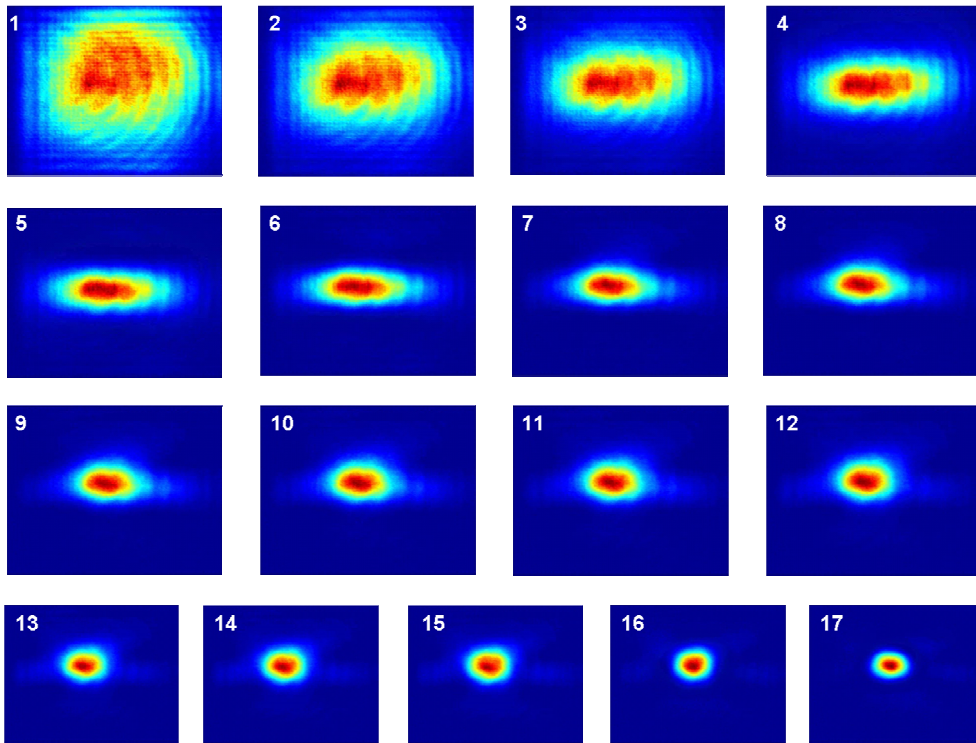


Fig.13: Sequence of 17 reconstructed intensity images of the soliton formation process. Frame 1 corresponds to $t=0$ (a normally diffracting beam), frame 17 to the end of the process (a beam with an almost symmetrical soliton shape), after more or less 300s.

To quantify the differences between the two axes beam dimensions in Fig.14 is shown the output beam diameter along y and z axes as function of the time, from the beginning till the end of the writing process. The beam narrows along the z direction (corresponding to the applied field direction) faster than along the y one. The last frame of the sequence of the previous figure is shown as inset and represents the formed soliton.

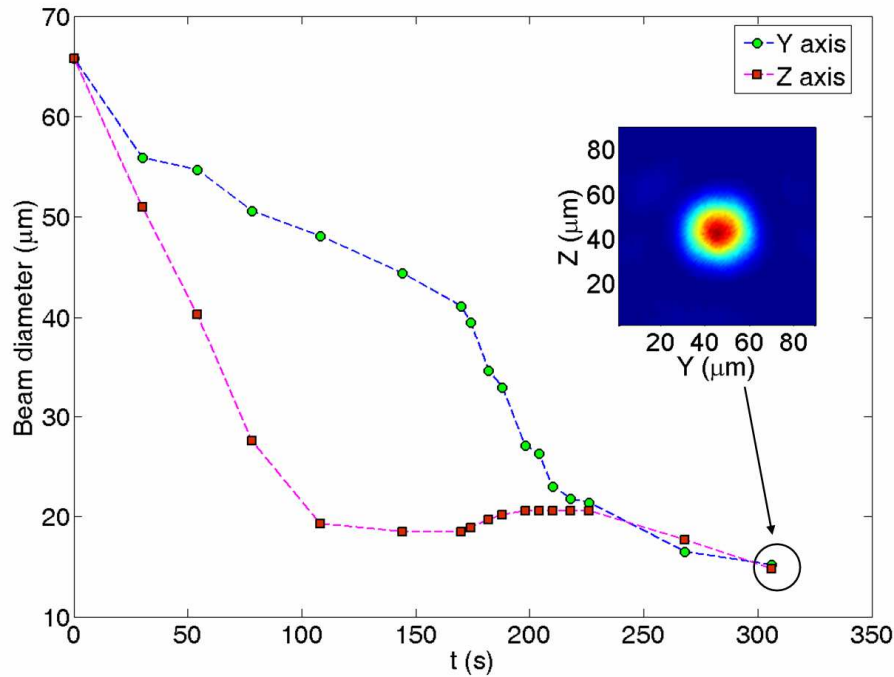


Fig. 14: Output beam diameters along y (circles) and z (squares) axes as functions of time. Each experimental point corresponds to a frame of Fig.13. **Inset:** last frame of the sequence of Fig.13, representing the beam intensity at the end of the soliton formation process.

We notice that the two diameters, which at the beginning were identical, decrease in a different manner but at the end become more or less of the same size. This is a further confirmation that the solitonic regime has been achieved in both directions, in agreement with ref. [33].

Complete waveguide creation is also proved by the phase maps and profiles along the y-axis, displayed in Fig.15 and Fig.16, respectively. We can see that, after more or less 4 minutes, the phase profile becomes flat, and then presents a sort of saturation: this confirms that the soliton generation, i.e. the writing process, is completed [38].

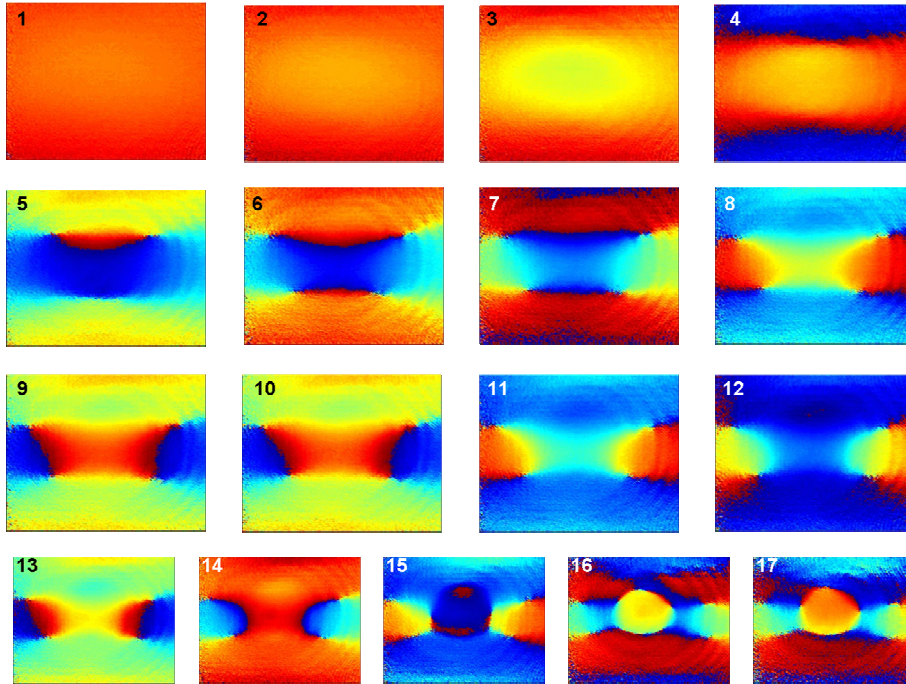


Fig. 15: Sequence of 17 reconstructed phase images of the soliton formation process, in analogy with the intensity ones of Fig.13.

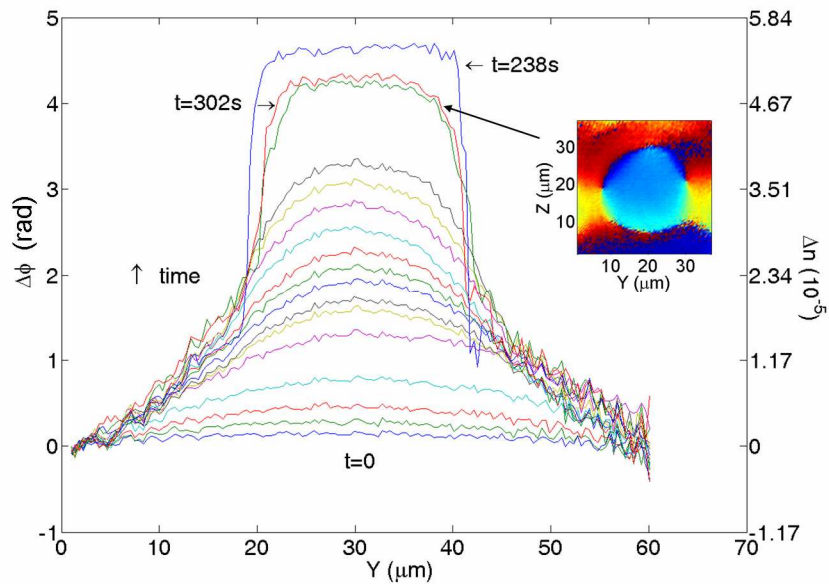


Fig. 16: Phase profiles along y-axis of the evolving beam of Figs. 13-15. In the inset is shown the phase map corresponding to the last profile obtained (last frame of Fig.15). The difference in the colours is just due to a phase shift.

The refractive index variation at the end of the process is $\Delta n \approx 5.2 \cdot 10^{-5}$, as displayed in Fig.17, in agreement with the steady-state measurements.

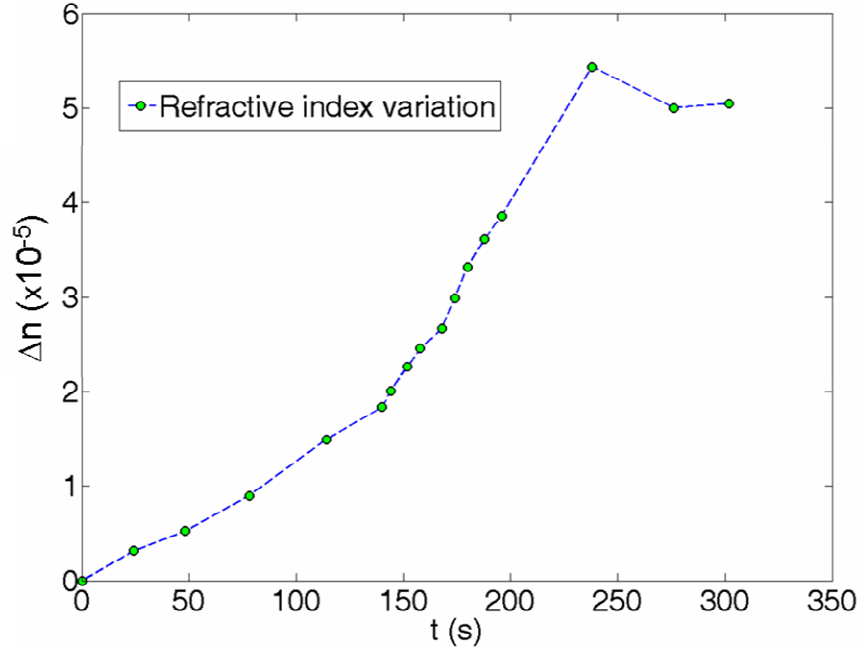
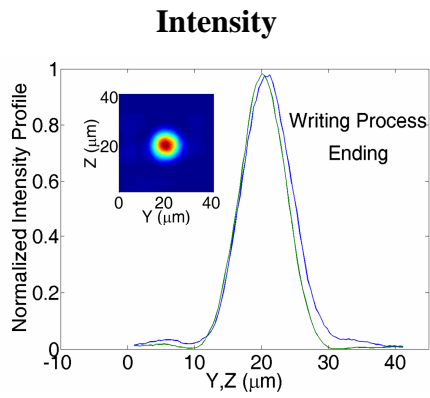


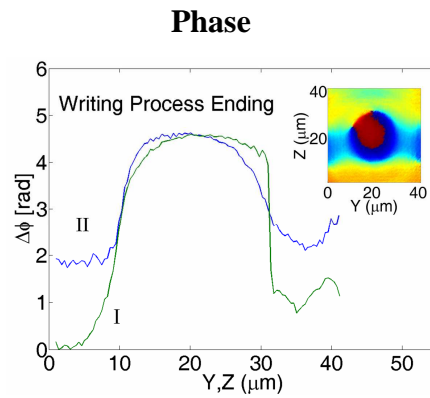
Fig. 17: Refractive index variation with the increasing of time.

2.5 Long time behavior of the induced refractive index perturbation

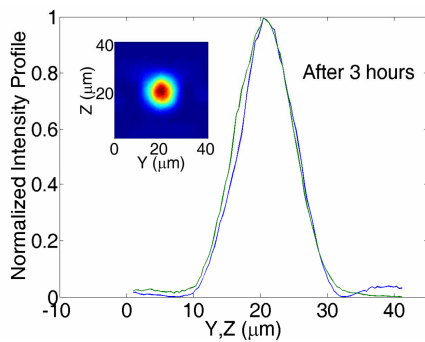
The long time behavior of the solitonic waveguide has been studied by characterizing the soliton beam profile after the external field was turned off (i.e. after the completion of the writing process): immediately, three hours, one day and a month later. Figs. 18(a-h) show the intensity and phase profiles along y and z -axes, as well as the reconstructed intensity and phase maps (in the insets) of the soliton beam, at the exit face of the crystal, at different times.



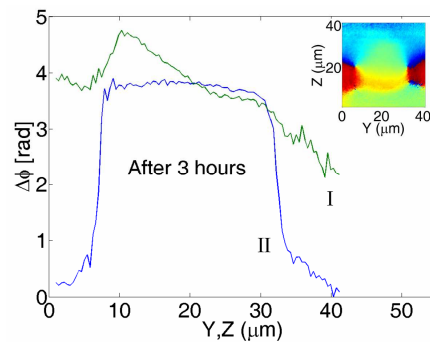
(a)



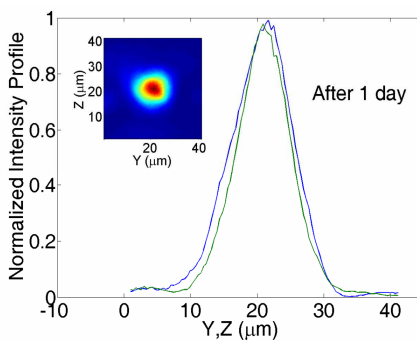
(e)



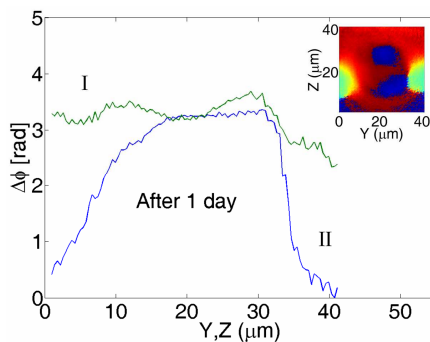
(b)



(f)



(c)



(g)

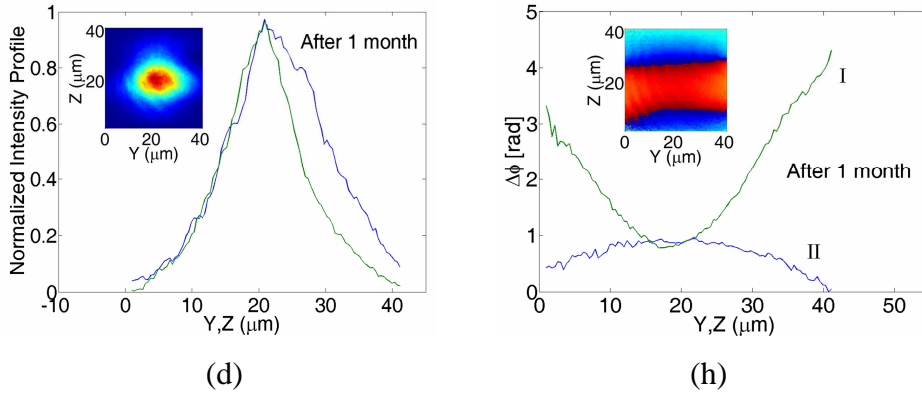


Fig. 18: Intensity (a-d) and phase (e-h) profiles along y (blue line, II) and z (green line, I) axes of the soliton beam, at the exit face of the crystal, at different times after the completion of the waveguide writing process: immediately (a,e), 3 hours (b,f), 1 day (c,g) and 1 month (d,h). Reconstructed intensity and phase maps are displayed in the insets.

At first glance, looking at the intensity images, it could seem that, even after a month, the solitonic waveguide is preserved, at least along the z-axis. However, careful analysis of the phase maps and of the corresponding profiles (Figs. 18(e-h)) reveals that the optical beam is no more solitonic, i.e. the waveguide tends to disappear, just a few hours after the conclusion of the writing process. This is probably due to the fact that, after the first measure (a,e), the sample has been reutilized for other tests, and so illuminated by both the background beam and natural light, leading to a re-distribution of charges and of the internal electric field.

However, other measurements carried out on another LN sample have shown that the guide can be preserved for a couple of months, if kept in dark. Moreover, some techniques enabling permanent fixing of solitonic waveguides have already been developed [33].

Conclusions

In this chapter is reported, from an experimental point of view, an accurate amplitude and phase analysis of the photorefractive bright soliton formation process inside an undoped lithium niobate crystal, by means of an interferometric digital holographic technique.

Thanks to this technique it has been possible to study the optical beam profile at the exit face of the crystal both in a stationary and time evolving situation, discerning, with the analysis of the phase, when and in which writing conditions the solitonic regime was actually achieved, while from an intensity analysis it was not always clear. The long time behavior of the waveguide has been also investigated, in order to estimate the time the soliton regime was preserved.

Moreover, the phase analysis allowed us to monitor and quantify the changes in the refractive index of the medium, and so to characterize the solitonic waveguide in the diverse situations.

The possible application in waveguiding is evident, as the soliton shape of the beam can be perfectly cylindrical and it is not necessary to have different media for the “core” and the “cladding”, as the refractive indexes difference is assured by the PR effect. Furthermore, being the refractive profile not depending on any physical-chemical process, while being self-written by an undiffracting light beam, it is optimized for single-mode propagation, low dispersion and low losses.

Some of the results discussed in this chapter have led to the publication of the article of ref. [40].

References:

- [1] B. Chen and T. Findakly Eds., *Optical waveguide fabrication in Integrated Optical Circuits and Components*, Marcel Dekker (1987).
- [2] S. Miyazawa: “Growth of LiNbO₃ single-crystal film for optical waveguides”, *Appl. Phys. Lett.* **23**, p.198 (1974).
- [3] R.A. Betts and C.W. Pitt: “Growth of thin-film lithium niobate by molecular beam epitaxy”, *Electr. Lett.* **21**, p.960 (1985).
- [4] <http://en.wikipedia.org/wiki/Soliton>
- [5] J.S. Russell: “Report on waves”, *Fourteenth meeting of the British Association for the Advancement of Science*, 1844.
- [6] A. Hasegawa and F. Tappert: “Transmission of stationary nonlinear optical pulses in dispersive dielectric fibers. I. Anomalous dispersion”, *Appl. Phys. Lett.* **23**, p.142 (1973).
- [7] L. Mollenauer, R. Stolen and J. Gordon: “Experimental observation of picosecond pulse narrowing and solitons in optical fibers”, *Phys. Rev. Lett.* **45**, p.1095 (1980).
- [8] A. Hasegawa: *Optical Solitons in Fibers* (Springer-Verlag, Berlin, 1989).
- [9] G.P. Agrawal, *Nonlinear Fiber Optics* (Academic Press, Boston, 1989).
- [10] K. Kos, H. Meng, G. Salamo, M. Shih, M. Segev and G. Valley: “One-dimensional steady-state photorefractive screening solitons”, *Phys. Rev. E* **53**, p.R4330 (1996).
- [11] M. Segev and G. Stegeman: “Self-Trapping of Optical Beams: Spatial Solitons”, *Physics Today* (1998).
- [12] G. Stegeman and M. Segev: “Optical Spatial Solitons and Their Interactions: Universality and Diversity”, *Science* **286**, p.1518 (1999).
- [13] Y. Karamzin and A. Sukhorukov, *Sov. Phys. JETP* **41**, p.414 (1976).
- [14] W. Torruellas et al.: “Observation of two-dimensional spatial solitary waves in a quadratic medium”, *Phys. Rev. Lett.* **74**, p.5036 (1995).

- [15] R. Schiek, Y. Baek and G. Stegeman: “One-dimensional spatial solitary waves due to cascaded second-order nonlinearities in planar waveguides”, *Phys. Rev. E* **53**, p.1138 (1996).
- [16] M. Segev, B. Crosignani, A. Yariv and B. Fischer: “Spatial solitons in photorefractive media”, *Phys Rev. Lett.* **68**, p.923 (1992).
- [17] C. Denz, M. Schwab and C. Weillnau: *Transverse-Pattern Formation in Photorefractive Optics* (Springer, Berlin, 2003).
- [18] P. Günter and J.-P. Huignard: *Photorefractive Materials and their Applications I* (Springer, New York, 2006).
- [19] M. Segev: “Optical spatial solitons”, *Opt. Quantum Electron.* **30**, p.503 (1998).
- [20] M. Taya, M.C. Bashaw, M.M. Fejer, M. Segev, and G.C. Valley: “Observation of dark photovoltaic spatial solitons”, *Phys. Rev. A* **52**, p. 3095 - 3100 (1995).
- [21] G. Valley, M. Segev, B. Crosignani, A. Yariv, M. Fejer and M. Bashaw: “Dark and bright photovoltaic spatial solitons”, *Phys. Rev. A* **50**, p. R4457 (1994).
- [22] M. Shih, M. Segev and G. Salamo: “Circular waveguides induced by two-dimensional bright steady-state photorefractive spatial screening solitons”, *Opt. Lett.* **21**, p.931 (1996).
- [23] M. Segev, G. Valley, B. Crosignani, P. Di Porto and A. Yariv: “Steady-state spatial screening solitons in photorefractive materials with external applied field”, *Phys. Rev. Lett.* **73**, p.3211 (1994).
- [24] M. Shih, M. Segev, G. Valley, G. Salamo, B. Crosignani and P. Di Porto: “Observation of two-dimensional steady-state photorefractive screening solitons”, *Electron. Lett.* **31**, p.826 (1995).
- [25] E. Del Re: *Solitons and Nonlinear Optical Propagation in Ferroelectric and Near-Critical Paraelectric Photorefractive Crystals*, Doctorate Thesis in Physics, Università dell’Aquila (1998).

- [26] E. Fazio, W. Ramadan, M. Bertolotti, A. Petris and V. Vlad: "Complete characterization of (2+1)D soliton formation in photorefractive crystals with strong optical activity", *J. Opt. A: Pure Appl. Opt.* **5**, p. S119-S123 (2003).
- [27] G. Duree et al.: "Observation of self-trapping of an optical beam due to the photorefractive effect", *Phys. Rev. Lett.* **71**, p.533 (1993).
- [28] E. Fazio et al.: "Screening-photovoltaic bright solitons in lithium niobate and associated single-mode waveguides", *Appl. Phys. Lett.* **85**, p.2193 (2004).
- [29] M. Paturzo, L. Miccio, S. De Nicola, P. De Natale and P. Ferraro: "Amplitude and phase reconstruction of photorefractive spatial bright-soliton in LiNbO₃ during its dynamic formation by digital holography", *Opt. Express* **15**, p.8243 (2007).
- [30] J. Petter and C. Denz: "Guiding and dividing waves with photorefractive solitons", *Opt. Comm.* **188**, p.55 (2001).
- [31] V. Vlad, E. Fazio, M. Bertolotti, A. Bosco and A. Petris: "Laser generated soliton waveguides in photorefractive crystals", *Appl. Surf. Sci.* **248**, p.484-491 (2005).
- [32] G. Couton, H. Maillotte, R. Giust and M. Chauvet: "Formation of reconfigurable singlemode channel waveguides in LiNbO₃ using spatial solitons", *Electron. Lett.* **39**, p.286 (2003).
- [33] E. Fazio et al.: "3-D integrated optical microcircuits in lithium niobate written by spatial solitons", Chap.5 of *Ferroelectric Crystals for Photonic Applications*, P. Ferraro, S. Grilli and P. De Natale eds. (Springer Series in Materials Science, 2008).
- [34] S. Grilli, P. Ferraro, S. De Nicola, A. Finizio, G. Pierattini and R. Meucci: "Whole optical wavefields reconstruction by Digital Holography", *Opt. Express* **9**, p.294-302 (2001).

- [35] P. Ferraro et al.: “Compensation of the inherent wave front curvature in digital holographic coherent microscopy for quantitative phase-contrast imaging”, *Appl. Opt.* **42**, p.1938-1946 (2003).
- [36] L. Miccio et al.: “Direct full compensation of the aberrations in quantitative phase microscopy of thin objects by a single digital hologram”, *Appl. Phys. Lett.* **90**, p.41104 (2007).
- [37] M. Iturbe Castillo, P. Marquez-Aguilar, J. Sanchez-Mondragon, S. Stepanov and V. Vysloukh: “Spatial solitons in photorefractive $\text{Bi}_{12}\text{TiO}_{20}$ with drift mechanism of nonlinearity”, *Appl. Phys. Lett.* **64**, p.408 (1994).
- [38] N. Fressengeas, J. Maufoy and G. Kugel: “Temporal behavior of bidimensional photorefractive bright spatial solitons”, *Phys. Rev. E* **54**, p.6866 (1996).
- [39] J. Maufoy, N. Fressengeas, D. Wolfersberger and G. Kugel: “Simulation of the temporal behavior of soliton propagation in photorefractive media”, *Phys. Rev. E* **59**, p.6116 (1999).
- [40] **F. Merola**, L. Miccio, M. Paturzo, S. De Nicola and P. Ferraro: “Full characterization of the photorefractive bright soliton formation process using a digital holographic technique”, *Meas. Sci. Technol.* **20**, p.045301 (10pp) (2009).

Chapter IV

Self-formation of PDMS microlens arrays on lithium niobate substrates

Summary

In this chapter, after a brief introduction about microlenses (and in particular about polymeric microlenses), an explanation of how an opportunely functionalized polar dielectric crystal can be suitable for the fabrication of an array of micrometric polymeric lenses is given. The fabrication process is obtained through the self-arrangement of a thin Polydimethylsiloxane (PDMS) liquid film onto a lithium niobate substrate. The above self-arrangement process is named here “Pyro-Electro-Wetting” (PEW) mechanism.

In this case the substrate, a LiNbO_3 (LN) z-cut wafer, is micro-engineered with periodically poled ferroelectric domains, with the aim to provide an appropriate wettability patterning induced by a thermal stimulus. Different experimental procedures are explored demonstrating that arrays of thousands of microlenses, having diameter size of $100\mu\text{m}$ and focal lengths ranging between $300\text{-}1000\mu\text{m}$, can be fabricated. Furthermore, a microscope interference method based on digital holography is adopted for microlenses' characterization.

Details about the fabrication process and the optical characterization are given.

1. Introduction to microlenses

Microlenses are small lenses, generally with diameters less than a millimeter and often down to $10\mu\text{m}$. Examples of microlenses can be found in nature, ranging from simple structures to gather light for photosynthesis in leaves to dewdrops or compound eyes in insects (Fig.1 (a-d)).

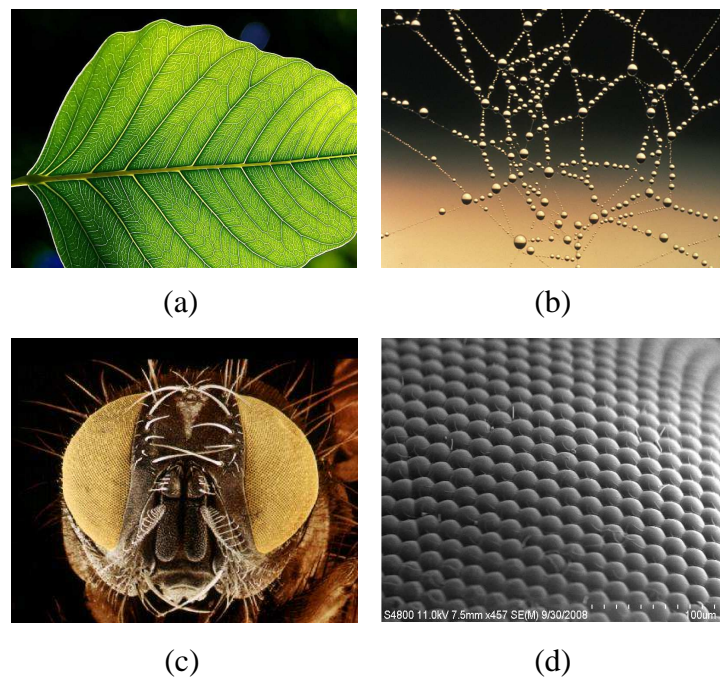


Fig. 1: Examples of natural microlenses.

On the other side, artificial single microlens and microlens arrays play a fundamental role in the actual photonic technology. Numerous materials and a variety of processes have been investigated for fabricating microlenses [1-4]. In particular, most of microlens arrays are fabricated by means of moulding or embossing processes starting from an original matrix [5-10].

For what concerns the materials used, they are basically of three kinds: *liquids* (such as oils), *liquid crystals* and *solids* (glasses, polymers). Each of them has different properties; for example liquid and liquid crystals microlenses possess a

tunable focal length, while solid microlenses have well defined optical properties and are much less influenced by external agents. Consequently, the applications of these microlenses are different: the solid ones are mainly used in the field of optical transmissions and photonics (fiber optics, CCD sensors), while the others are used in biomedicine, microfluidics, as displays (LCD monitors), ecc. However, it's to be pointed out that polymeric microlenses are recently being used also in the biological field [11].

Undoubtedly a great interest has been focused on microlenses with changeable focal length [12-17]. Tunable microlens arrays obtained by wettability patterning through *pyro-electro-wetting* (PEW) [18] have displayed a change in their focal length from infinity (afocal system) down to about 1mm [1]. Microlens array based on a hydrogel material actuated with temperature, that can switch from positive to negative focal lengths, has been also demonstrated [19].

Nevertheless, a great interest is still maintained in fabricating microlens arrays that are not tunable, by using different materials. In this way, polymeric materials such as PMMA [20] or PDMS [5] have been extensively investigated. PDMS is an elastomer material widely used in different applications, such as micro/nanofluidics, electrical insulation, micro/nanoelectromechanical systems (MEMS/NEMS), soft lithography, quantum dots and charge patterning in thin-film electrets [21-23].

PDMS offers many advantages for the fabrication of patterned structures. It is optically transparent, electrically insulating, mechanically elastic and gas-permeable. Moreover it is also biocompatible, thus finding application in the field of bioengineering, where the position of cells on a substrate is important for different purposes. These include biosensor fabrication for drug toxicity and environmental monitoring, tissue engineering, patterning of active proteins, patterning of animal cells and basic biology studies where the role of cell adhesion, shape, proliferation and differentiation are studied as a function of cell-cell and cell-extracellular matrix interactions [24-26]. The ability to reliably

pattern PDMS in the form of both thick substrates and thin membranes or films is critical for expanding the scope of its applications, especially in the fields of microfluidics and bioengineering.

In particular, as said above, PDMS is specifically suitable because of its good optical quality and the simplicity of the lenses fabrication process known as “soft lithography”. In soft lithography it is only necessary to have a mould to obtain a negative replica of the structure [3,6-8]. Recently, a replica moulding process to form a three dimensional metal pattern on the surface of polymeric microstructures has been demonstrated [9]. Fabrication of PDMS microlens arrays was demonstrated by surface wrinkling technique [27] or by using electromagnetic force-assisted UV printing [4]. Moreover, patterning of arrayed PDMS structures through parylene C lift-off [28] and capillary forming process [10] were demonstrated too.

It is important to note that lenses made with polymeric materials like PDMS can be also tuned thanks to the inherent elastic properties of the material. In fact, it has been demonstrated that a single PDMS microlens can be actuated and tuned thermally [29]. Furthermore, microlens arrays can change their focusing properties when subjected to lateral strain [30].

In the following it will be shown how microlens arrays made of PDMS can be self-formed on a polar dielectric substrate due to PEW effect. This self-patterning of PDMS by PEW approach has been recently discovered [31] and is here demonstrated that such discovered process can be exploited in several different ways to produce polymeric microlens arrays with different focal lengths, depending on the parameters adopted in the process and on the type of substrate’s functionalization. In fact, through this effective lithography-based technique, PDMS microlens arrays made of thousand of lenses have been obtained -as shown in Fig. 2- having micrometric size (100 μ m of diameter) and focal length in the range 300-1000 μ m. To the best of our knowledge such kind

of method for fabricating polymeric microlens arrays has never been performed before.

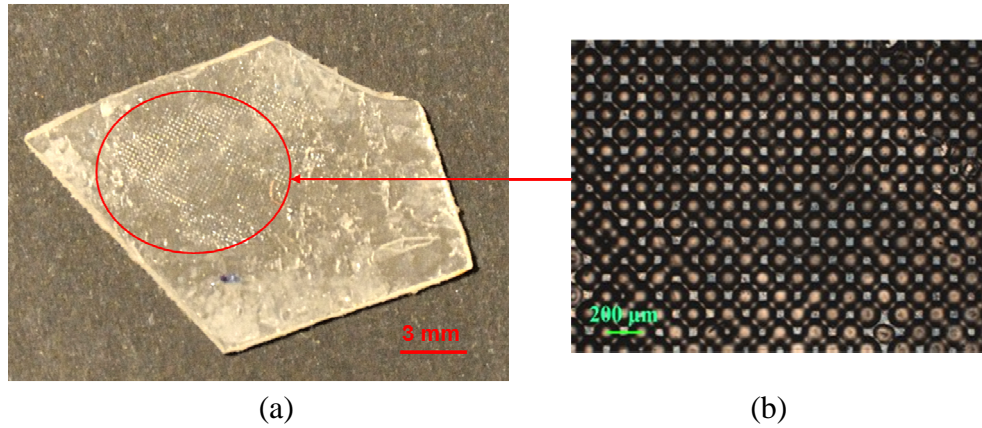


Fig. 2: (a) Example of fabricated sample. (b) Optical microscope image of the PDMS microlens array contained in the circle.

2. Fabrication of the samples

2.1 Photolithography and electric field poling

The fabrication process has been carried out onto a functionalized LN substrate. A polished 500 μm thick LN z-cut crystal (Crystal Technology Inc.) was subject to conventional mask-photolithography and standard periodic electric field poling [32,33] (see appendix at the end of the chapter) in order to achieve a square array of hexagonal reversed domains, shown in Fig. 3:

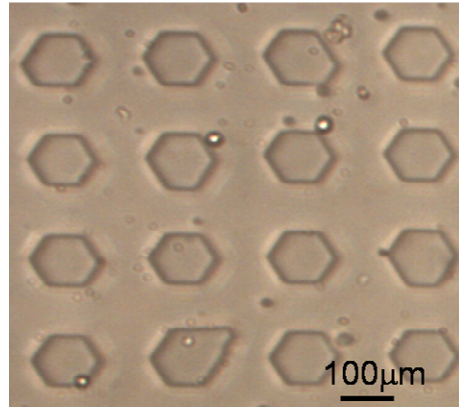
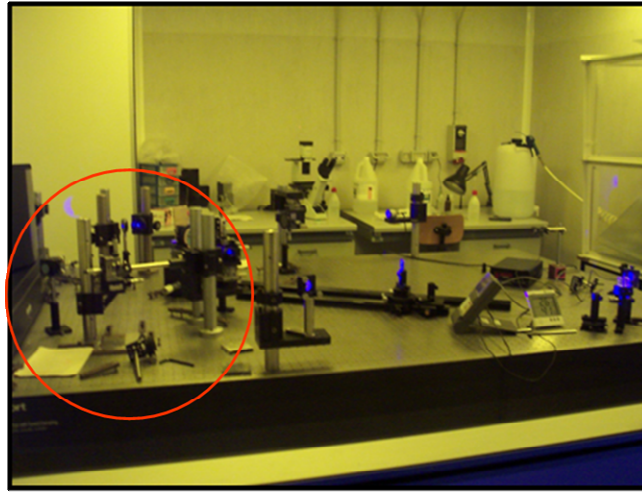


Fig. 3: Optical microscope image of the periodically poled LN sample.

An external voltage, exceeding the coercive field of the material (around 21 kV/mm), was necessary to reverse the ferroelectric domains, while the inversion selectivity was ensured by an appropriate resist pattern, generated by conventional photolithography. The period of the obtained domains is around 200 μm along both x and y crystal directions [1,31].

The photolithographic set-up is displayed in Fig. 4 (a,b):



(a)



(b)

Fig. 4: (a) Clean room and (b) close-up of the experimental apparatus (red circle in (a)) used for the photolithographic process on LN crystals.

It consists in a He-Cd laser emitting light at 441.6 nm. The exit beam, opportunely expanded, passes through a chromium mask with the geometry of

Fig. 5 and impinges on the LN sample, first spin-coated with a $1.3 \mu\text{m}$ thick photoresist layer (Shipley Microposit S1813-J2).

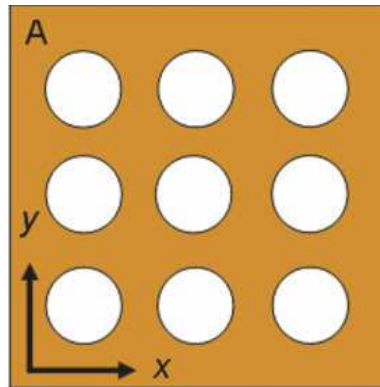


Fig. 5: Geometry of the mask used for the photolithographic process: a square array of round openings with pitch of $200\mu\text{m}$.

The sample was always baked after resist development to harden the resist before poling. It was mounted in a special Plexiglas holder [34], allowing both external voltage application for the periodic electric field poling (EFP) and laser illumination along the z crystal axis. A lithium chloride saturated solution was used as a liquid electrolyte. The external circuit consisted of a conventional signal generator which drove a high voltage amplifier and details are given in the appendix.

After poling, the layer of resist was peeled off and the sample presented the geometry of Fig.3. In fact, the round circles become hexagons because of the hexagonal structure of the LN unit cell (see Chap.I).

2.2 Microlenses' formation

Three different samples have been prepared, named A, B and C. Sample A was wet-etched in pure HF for 10 minutes (etching depth $\approx 12 \mu\text{m}$) after the poling

process with the aim to obtain a structure similar to that shown in Fig. 6. On the contrary, samples B and C were not etched.

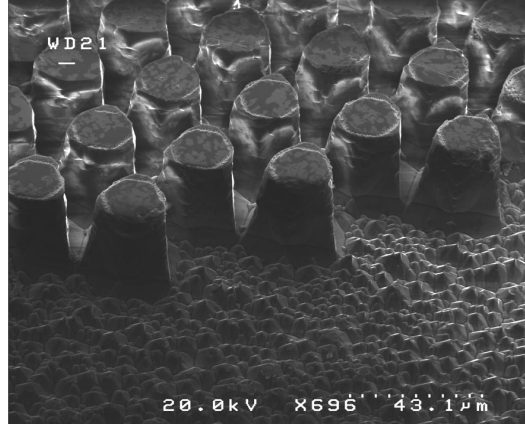


Fig. 6: SEM image of a HF etched LN sample after photolithographic and poling processes, having a slightly different pitch and depth of etching of sample A.

For **samples A** and **B**, a layer of PDMS polymer solution (Dow Corning Sylgard 184, 10:1 mixing ratio base to curing agent) was spin-coated onto the z-face of the periodically poled lithium niobate (PPLN) substrate at 6000 RPM for 2 min. The PDMS-coated samples (with a PDMS layer thickness of about 3 μm) were then placed onto a hotplate at a temperature of 170°C for 30s, thus inducing rapid heating of the sample and generating a microlens array following the arrangement of the hexagonal domains [18], as depicted in Fig. 7.

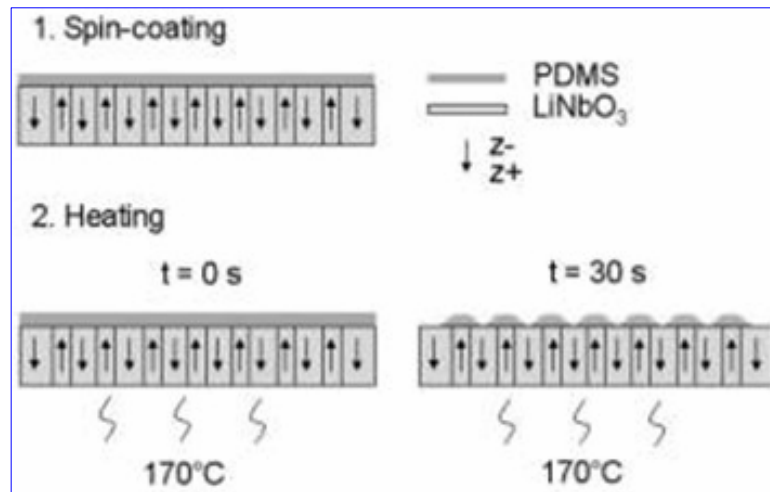


Fig. 7: Schematic view of microlenses' formation process steps.

The subsequent sudden cooling (from 170°C to room temperature) solidified the PDMS lenses that were so ready for being characterized, as shown in Figs. 8(a) and 9(a).

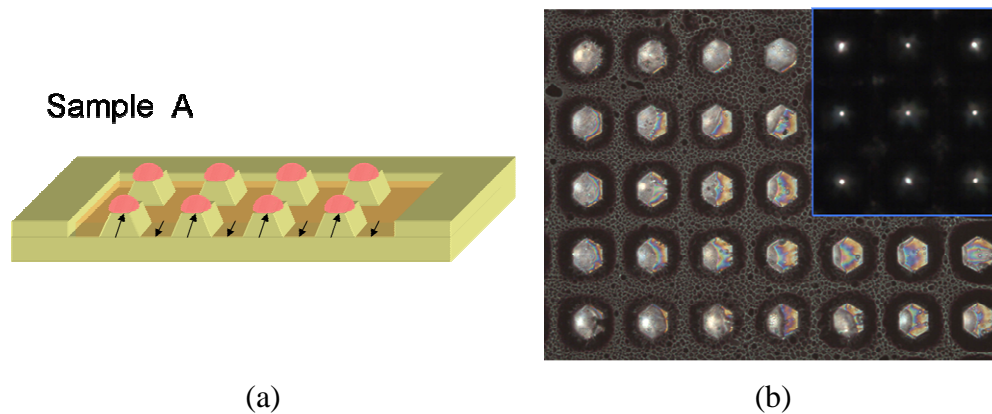


Fig. 8: (a) Drawing and (b) optical microscope image of fabricated *sample A*: etched PPLN with reversed hexagonal domains, on which a PDMS microlens square array was formed. The pitch of the structures is about 200 μm .

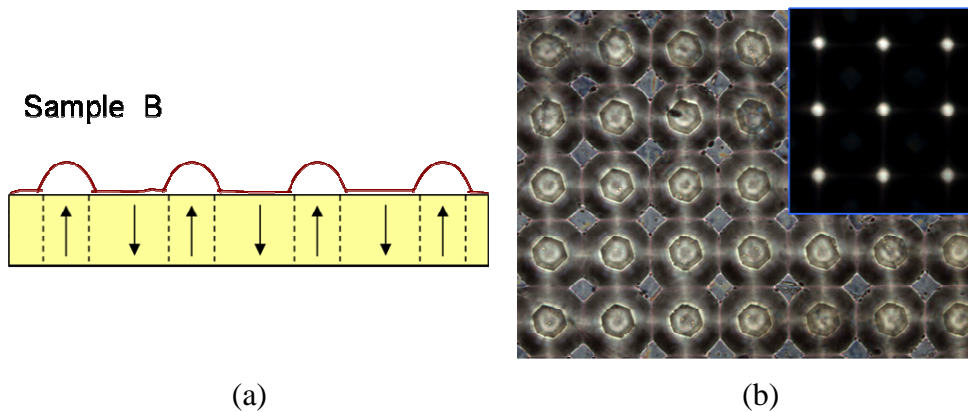


Fig. 9: (a) Drawing and (b) optical microscope image of *sample B*: non-etched PPLN with PDMS microlenses.

Sample C was prepared in a different way. A layer of $1.3\mu\text{m}$ -thick photoresist was first spin-coated on a LN z-face, at 3000 RPM for 1min; subsequently, the sample was placed onto a hotplate at a temperature of 115°C for 60s in order to bake the resist. Then, it was covered with a drop of PDMS diluted with Hexane (mixing ratio 3:1 PDMS to Hexane), placed onto a hotplate at a temperature of 130°C for 60s, chilled and finally peeled off. In this way the microlens array was detached from the substrate adopted to realize it, as displayed in Fig. 10(a). It must be said that the photoresist (being a dielectric material) did not seem to affect too much the PDMS microlenses' formation process, at least with the very thin layer used for this experiment.

Figs. 8-10(b) show the optical microscope images corresponding, respectively, to samples A, B and C in the substrate's plane, the image in the lenses focus plane being displayed as insets.

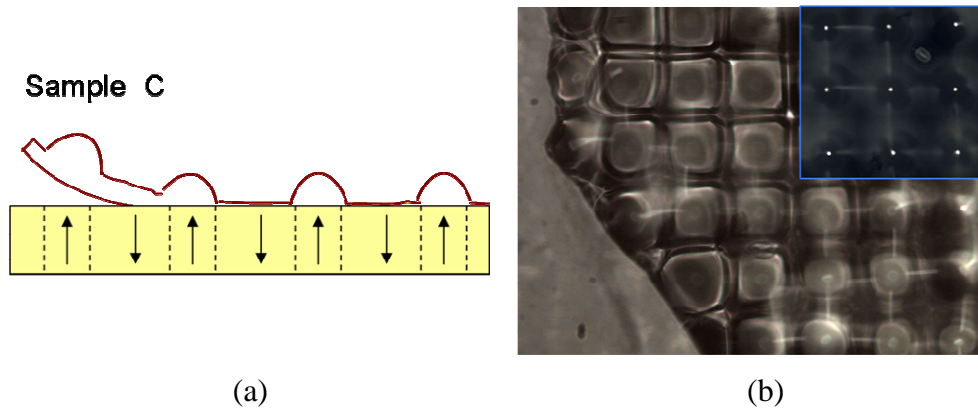


Fig.10: *Sample C* : PDMS microlenses alone, peeled off from a non-etched PPLN substrate.

Explanation of the phenomenon

The PDMS patterning is related to the spatial wettability variation of the LN substrate under the pyroelectric effect [18]. The pyroelectricity exhibited at room temperature by LN [35] makes the spontaneous polarization P_s to change according to $\Delta P_i = p_i \Delta T$, where P_i is the coefficient of the polarization vector, p_i is the pyroelectric coefficient and ΔT is the temperature variation.

At equilibrium, the whole polarization in the crystal is fully screened by the external screening charge σ , and no electric field exists. The polarization intensity decreases under heating and increases under cooling, thus causing an excess or lack of surface charge, respectively, as shown schematically in Fig.11(a). These surface charges generate high electric field distributions [18].

In particular, Fig.11(b) shows the side view of the sample with a numerical simulation of the electric potential distribution induced into the liquid PDMS by pyroelectric charges. The hexagonal reversed domains correspond to the narrower regions into the scheme of the crystal cross section.

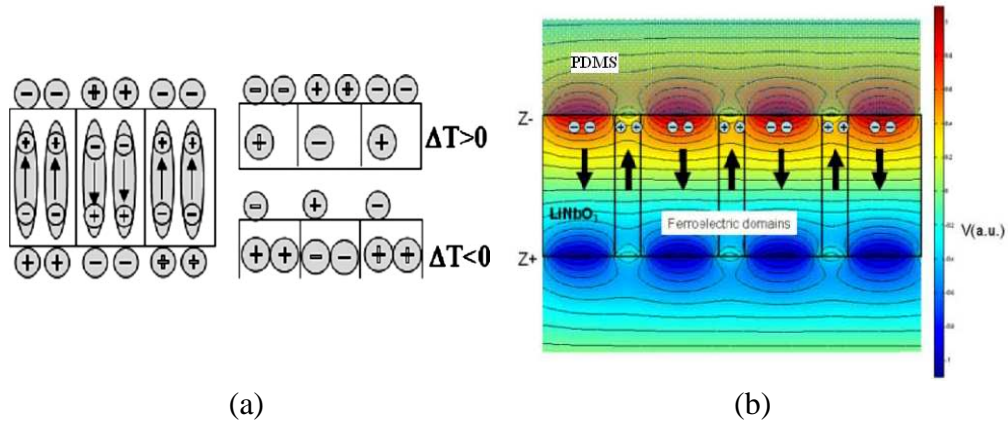


Fig. 11: (a) Schematic view of the surface charges formation under thermal treatment; (b) simulation of the electric potential distribution generated by the pyroelectric charges.

It is important to note that the potential is distributed according to the reversed domain pattern with higher intensities corresponding to the regions outside the hexagonal domains. Consequently, the surface tension at the PDMS-crystal interface varies according to an electrowetting-like effect (the above mentioned “PEW”), where the electric fields are generated by the uncompensated surface charges produced during the thermal treatment.

In fact, it is well-known that, in the general case of a sessile droplet, the surface tensions at the solid-liquid γ_{sl} , solid-gas γ_{sg} , and liquid-gas γ_{lg} interfaces are described by the one-dimensional Young equation

$$\gamma_{sl} + \gamma_{lg} \cos \vartheta = \gamma_{sg} \quad (1)$$

where ϑ corresponds to the *contact angle* of the droplet. The charges at the solid-liquid interface reduce the surface tension according to the Lippman equation [36]:

$$\gamma_{sl}(V) = \gamma_{sl0} - \frac{1}{2}CV^2 \quad (2)$$

where γ_{sl0} corresponds to zero charge condition, V is the electric potential, and C is the capacitance per unit area, assuming that the charge layer can be modeled as a symmetric Helmholtz capacitor [37]. Even though the surface here is not a metal and the liquid is not an electrolyte, as assumed by the double charge model, a similar model still describes the effect in case of dielectric surfaces [38].

The surface tension profile is then calculated by using Eq. (2) and the corresponding behaviour, in accordance with the experimental results, is shown in Fig.12:

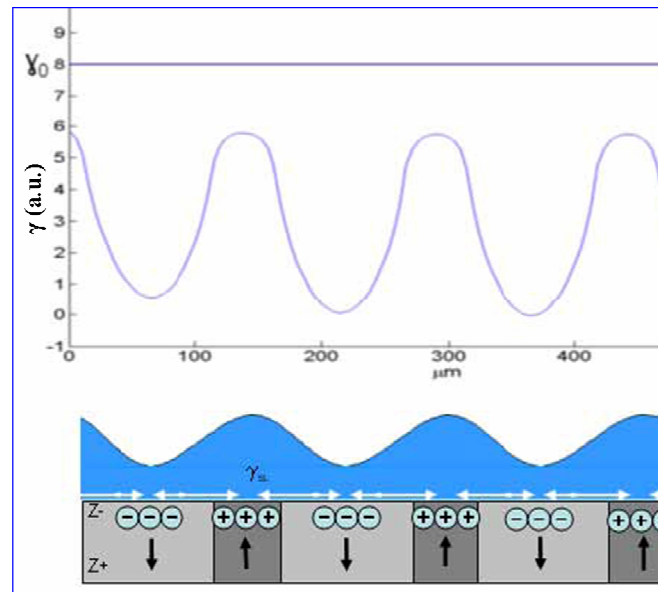


Fig.12: (top) Surface tension profile and (bottom) schematic view of the corresponding PDMS film topography. The black arrows indicate the orientation of the spontaneous polarization.

The air-PDMS interface exhibits a waviness profile in order to minimize the energy of the whole system. The simulation clearly shows that the surface tension is modulated according to the domain structure, thus exhibiting maximum value in correspondence of the hexagon centres.

3. Microlenses' characterization by digital holography

The three fabricated samples exhibit different optical properties; they have been characterized by a digital holographic technique. The experimental set-up consists in a typical Mach-Zehnder interferometer arranged in a transmission configuration, as depicted in Fig.13. The source is a continuous-wave solid state laser emitting light at 532 nm. The beam is divided in two by a beam splitter; the object beam passes through a thin PDMS microlens array and is imaged by a 5X microscope objective onto a CCD camera. The reference beam, opportunely expanded and with the same polarization of the object one, is recombined with it thanks to another beam splitter. The resulting interference pattern (the *digital hologram*, see Chap.II), is recorded by the CCD camera (pixel size 4.4 μm), placed at a distance d from the image plane according to the holographic technique.

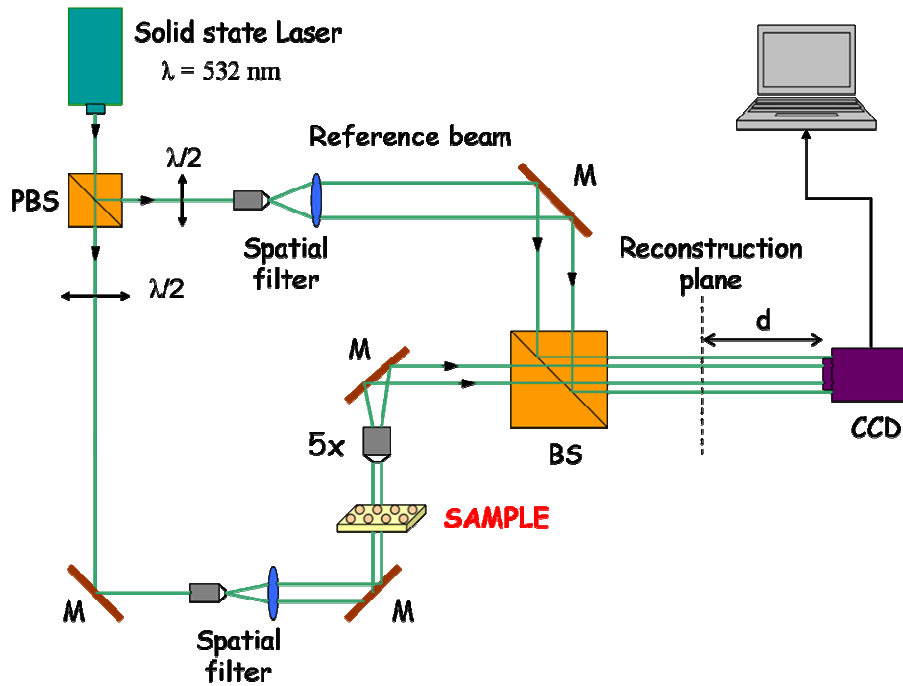


Fig. 13: Experimental set-up used for the microlenses' optical characterization.

The intensity and the phase of the complex wavefields passing through the PDMS sample are numerically calculated starting from these digitally recorded holograms, that contain all the specimen's information. Thanks to the flexibility of DH the wavefields reconstruction is possible in different image planes without changing the set-up, i.e. without moving the sample.

Figs. 14-16(a) display the phase maps of a portion of each sample. The phase of three microlenses, each picked out from a different sample and indicated by a red frame, has been analysed in order to recover the **focal length** f . Figs.14-16(b) show a parabolic fit along both dimensions of the unwrapped phase map $\varphi(x,y)$, according to the equation

$$\varphi(x, y) = \frac{2\pi}{\lambda} \frac{(x^2 + y^2)}{2f} \quad (3)$$

with $\lambda=0.532\mu\text{m}$. Here the parabolic approximation of the spherical wavefront of the beam passed through the lens has been considered. The focal lengths recovered from the parabolic fits are:

Sample A: $f \approx 307 \mu\text{m}$

Sample B: $f \approx 1010 \mu\text{m}$

Sample C: $f \approx 394 \mu\text{m}$

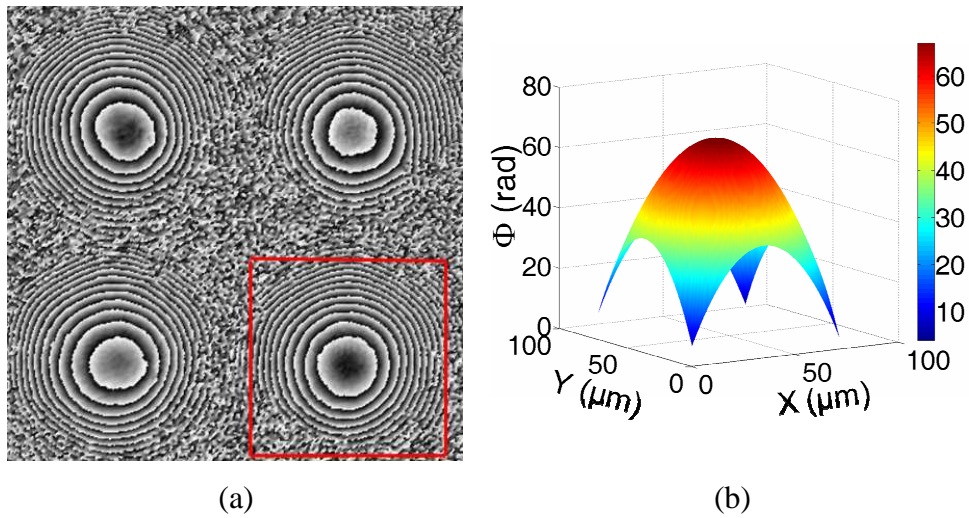


Fig. 14: (a) Phase map of a portion of **sample A** and (b) parabolic fit corresponding to the microlens in red frame. $f \approx 307 \mu\text{m}$.

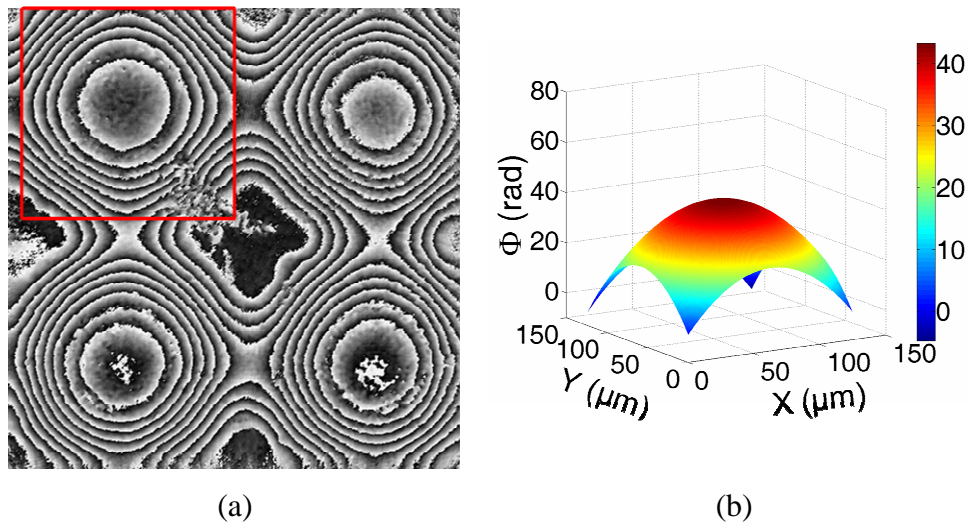


Fig. 15: (a) Phase map of a portion of **sample B** and (b) parabolic fit corresponding to the microlens in red frame. $f \approx 1010 \mu\text{m}$.

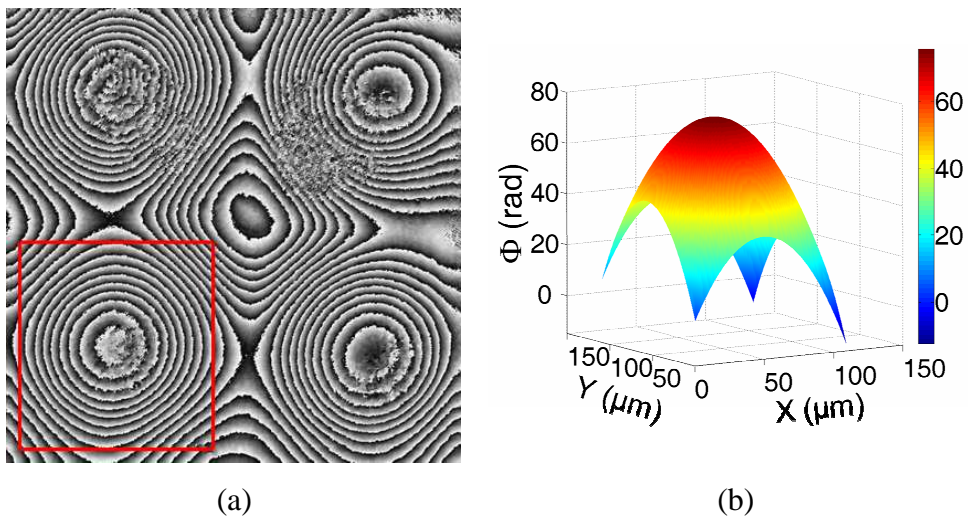


Fig. 16: (a) Phase map of a portion of **sample C** and (b) parabolic fit corresponding to the microlens in red frame. $f \approx 394 \mu\text{m}$.

By the measurements it results that the smallest focal length is that of sample A. This effect is probably due to etching and thus reduction of the domains area.

For sample B the value of f is higher and the lenses are flatter -probably as a consequence of the fabrication process- as results from the fringes number and from the lower value of the phase (see Fig.15(a,b)). As regards sample C, it seems that the process of peeling did not cause appreciable deformations in the lenses' shape or aberrations (see Fig.16(a,b)). This could be very important for a realistic application of polymeric microlens arrays. The evaluated focal length is of the same order of magnitude of sample A.

For sample A an amplitude reconstruction varying the reconstruction distance d has been also performed. By a single acquisition with the CCD it has been possible to recover, by varying d , the amplitude of the beams exiting from the microlenses, at different steps, starting from the lens array plane up to the lens focal plane, as shown in Fig. 17(a).

The result is displayed in Fig. 17(b), the resulting focal length being about $300\mu\text{m}$, in agreement with that obtained from the parabolic fit for sample A.

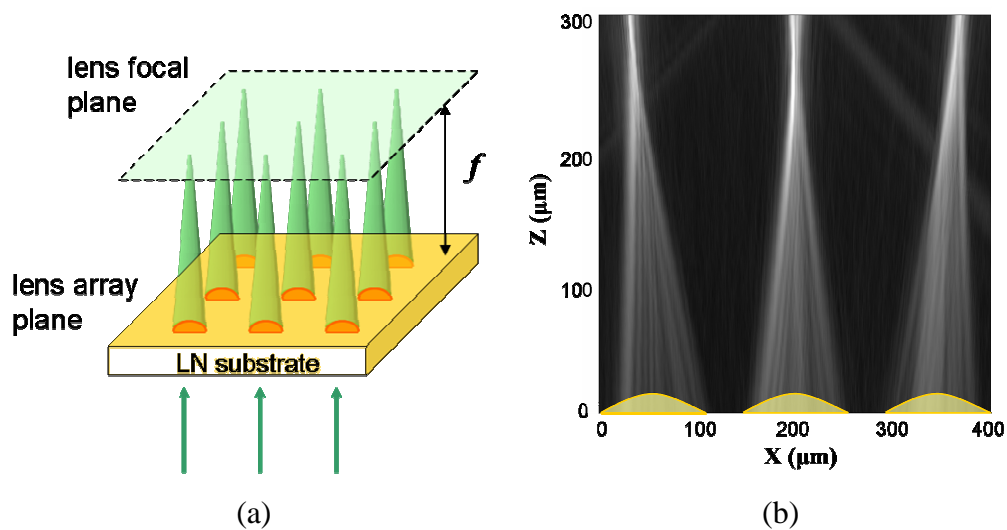


Fig.17: (a) Scheme of the path of the rays passing through the sample. (b) Reconstructed amplitude of the beams exiting from the microlenses and focusing after about 0.3 mm .

Conclusions

In this chapter a quick and relatively simple way for fabricating PDMS microlens arrays has been reported, based on thermal self-patterning of PDMS films on micro-engineered LN crystals, which could find suitable applications in optical fibers or biomedicine [11]. A careful optical analysis of the fabricated microlenses by means of digital holography has been performed, allowing to determine the focal length of each single lens. The measured focal lengths range from about 300 μm up to 1000 μm .

Besides, the process is repeatable many times, simply cleaning the sample with ethanol or acetone, and the desired lenses' focal lengths can be decided "a priori" knowing the parameters used for their fabrication.

Some of the results discussed in this chapter have led to the publication of the article of ref. [39].

Appendix

Periodic electric field poling

Several methods have been developed to produce periodic domain structures in LN. The most widely used nowadays consists in the application of high external electric fields at room temperature to reverse the spontaneous polarization of the crystal, the so called *electric field poling* (EFP) [40]. This technique has produced PPLN crystals [32,41] for quasi-phase-matching (QPM) SHG.

Starting from a single-domain crystal the production of periodic domain structures is achieved by application of electric fields at room temperature [32]. The challenge of fabricating high quality QPM structures by EFP lies in achieving few micrometers wide domains in crystals of several millimeters in thickness. This puts high demands on the poling process.

Most last years papers on PPLN structures obtained by EFP use commercial samples of 0.5 mm thickness and interaction lengths of few centimeters are

commonly reported. Thicker samples cannot be used because of the dielectric breakdown appearing before domain inversion. Recently it has been reported the decrease of the ferroelectric coercive field by one order of magnitude between congruent and stoichiometric crystals. This makes possible the electric field fabrication of periodic structures at room temperature in few millimeters thick samples [42].

Periodic EFP consists of using lithographic techniques to produce a photoresist grating of the desired period to be used as a mask for applying the electric field with a liquid electrolyte electrode [32]. A positive voltage pulse slightly exceeding the coercive field of the material (around 21 kV/mm in LN) is applied on the patterned crystal face by using a liquid electrolyte. The liquid electrode configuration has two electrolyte containing chambers which squeeze the sample between two *O*-ring gaskets, as shown schematically in Fig. 18.

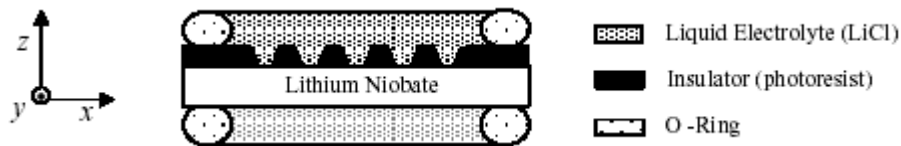


Fig. 18: Schematic view of the sample cross section after lithographic patterning.

Fig.19 illustrates the external electrical circuit. A conventional Signal Generator (SG) drives an High Voltage Amplifier (HVA - 2000x) with a series current limiting resistor R_S in order to get a 12kV positive voltage. A diode rectifier D is connected to the output of the HVA to prevent flowing of backswitch current in the circuit.

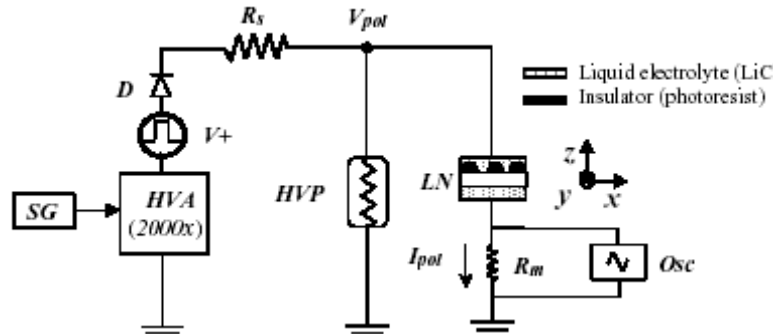


Fig.19: Schematic view of the external circuit for EFP. *SG* = Signal Generator; *HVA* = High Voltage Amplifier; *D* = Rectifier Diode; R_s = Series Resistor; V_{pol} = Poling Voltage; *HVP* = High Voltage Probe; R_m = Monitoring Resistor; *OSC* = Oscilloscope; I_{pol} = Poling Current.

In case of LN the reversed domains typically grow beyond the width of the electrodes as result of the remaining fringing fields along the edges of the lithographic grating strips [32]. For example, in PPLN processed for infrared applications (periods $>10 \mu\text{m}$), the inverted domain width is typically $\approx 3\text{-}4 \mu\text{m}$ wider than that of the electrode. To obtain the desired domain size, insulating strips wider than the electrodes must be fabricated. The strategy for optimal domain patterning is to stop the voltage pulse before poling progresses under the photoresist layer. This is usually accomplished by delivering the “a priori” known amount of charge required for polarization reversal in the electrode regions [43].

The conductivity of LN at room temperature is low enough that the poling current can be monitored readily by measuring the voltage drop across the R resistor (usually $10 \text{ k}\Omega$), while a conventional High Voltage Probe (HVP) is used to measure the poling voltage V_{pol} across the sample. Both current and voltage waveforms are visualized on the oscilloscope *OSC* during the poling process.

Reversed ferroelectric domain patterns are usually inspected unambiguously by a well established technique based on selective wet etching [44]. A HF:HNO₃=1:2 mixture etching solution is used for LN with the property to attack the z^- polarity face while leaving z^+ face untouched. Faster etching rates are obtained by acid bath at high temperature. Alternative approaches include the non-invasive domain visualization by crossed polarizers [45] and the observation of domain structure by the EO effect [46].

References:

- [1] S. Grilli et al.: “Liquid micro-lens array activated by selective electro-wetting on lithium niobate substrates”, *Opt. Express* **16**, p.8084 (2008).
- [2] P. Ruffieux et al.: “Two step process for the fabrication of diffraction limited concave microlens arrays”, *Opt. Express* **16**, p.19541 (2008).
- [3] S. Chang and J. Yoon: “Shape-controlled, high fill-factor microlens arrays fabricated by a 3D diffuser lithography and plastic replication method”, *Opt. Express* **12**, p.6366 (2004).
- [4] T.T. Wen and H. Hocheng: “Innovative rapid replication of microlens arrays using electromagnetic force-assisted UV imprinting”, *J.Micromech. Microeng.* **19**, p.025012 (2009).
- [5] T.H. Lin, H. Yang and C.K. Chao: “Concave microlens array mold fabrication in photoresist using UV proximity printing”, *DTIP of MEMS & MOEMS*, Stresa, Italy (2006).
- [6] C.Y. Chang, S.Y. Yang, L.S. Huang and T.M. Jeng: “A novel method for rapid fabrication of microlens arrays using micro-transfer molding with soft mold”, *J. Micromech. Microeng.* **16**, p.999 (2006).
- [7] T.K. Shih, J.R. Ho and J.W.J. Cheng: “A new approach to polymeric microlens array fabrication using soft replica molding”, *IEEE Phot. Tech. Lett.* **16**, p.2078 (2004).
- [8] T.K. Shih, C.F. Chen, J.R. Ho, F.T. Chuang: “Fabrication of PDMS (polydimethylsiloxane) microlens and diffuser using replica molding”, *Microel. Eng.* **83**, p.2499 (2006).
- [9] Y. Zhao et al.: “Three dimensional metal pattern transfer for replica molded microstructures”, *Appl. Phys. Lett.* **94**, p.023301 (2009).
- [10] C.Y. Chang, S.Y. Yang, L.S. Huang and K.H. Hsieh, “Fabrication of polymer microlens arrays using capillary forming with a soft mold of

- micro-holes array and UV-curable polymer”, *Opt. Express* **14**, p.6253 (2006).
- [11] C.-M. Cheng, J.D. Kubicek and P.R. LeDuc: “Polymeric microlenses for real-time aqueous and nonaqueous organic imaging”, *Appl. Phys. Lett.* **88**, p.053902 (2006).
- [12] K.S. Hong et al.: “Tunable microfluidic optical devices with an integrated microlens array”, *J. Micromech. Microeng.* **16**, p.1660 (2006).
- [13] H. Ren and S.T. Wu: “Tunable-focus liquid microlens array using dielectrophoretic effect”, *Opt. Express* **16**, p.2646 (2008).
- [14] Y. Choi, H.R. Kim, K.H. Lee, Y.M. Lee and J.H. Kim: “A liquid crystalline polymer microlens array with tunable focal intensity by the polarization control of a liquid crystal layer”, *Appl. Phys. Lett.* **91**, p.221113 (2007).
- [15] G.R. Xionget al.: “Liquid microlens with tunable focal length and light transmission”, *Appl. Phys. Lett.* **92**, p.241119 (2008).
- [16] X. Huang et al.: “Thermally tunable polymer microlenses”, *Appl. Phys. Lett.* **92**, p.251904 (2008).
- [17] H.Y. Dai, Y.J. Liu, X.W. Sun and D. Luo: “A negative–positive tunable liquid-crystal microlens array by printing”, *Opt. Express* **17**, p.4317 (2009).
- [18] P. Ferraro, S. Grilli, L. Miccio and V. Vespini: “Wettability patterning of lithium niobate substrate by modulating pyroelectric effect to form microarray of sessile droplets”, *Appl. Phys. Lett.* **92**, p.213107 (2008).
- [19] Z. Ding and B. Ziaie: “A pH-tunable hydrogel microlens array with temperature-actuated light-switching capability”, *Appl. Phys. Lett.* **94**, p.081111 (2009).
- [20] P.H. Huang, T.C. Huang, Y.T. Sun and S.Y. Yang: “Fabrication of large area resin microlens arrays using gas-assisted ultraviolet embossing”, *Opt. Express* **16**, p.3041 (2008).

- [21] B.H. Jo, L.M. Van Lerberghe, K.M. Motsegood, D.J. Beebe: “Three-dimensional micro-channel fabrication in polydimethylsiloxane (PDMS) elastomer”, *J. Microelectromech. Syst.* **9**, pp. 76-81 (2000).
- [22] K.H. Jeong, G.L. Liu, N. Chronis, L.P. Lee: “Tunable microdoublet lens array”, *Opt. Express* **12**, p.2494 (2004).
- [23] H.O Jacobs and G.M. Whitesides: “Submicrometer Patterning of Charge in Thin-Film Electrets”, *Science* **291**, p.1763 (2001).
- [24] S.L. Peterson, A. McDonald, P.L. Gourley, D.Y. Sasaki: “Poly (dimethylsiloxane) thin films as biocompatible coatings for microfluidic devices: Cell culture and flow studies with glial cells”, *J. Biomed. Mater. Res. A* **72A**, p.10 (2005).
- [25] H. Andersson and A. van den Berg: “Microfabrication and microfluidics for tissue engineering: state of the art and future opportunities”, *Lab. Chip.* **4**, p.98 (2004).
- [26] C.S. Chen, M. Mrksich, S. Huang, G.M. Whitesides, D.E. Ingber: “Geometric Control of Cell Life and Death”, *Science* **276**, p.1425 (1997).
- [27] E.P. Chan and A.J. Crosby: “Fabricating microlens arrays by surface wrinkling”, *Adv. Mater.* **18**, p.3238 (2006).
- [28] J. Tong, C.A. Simmons and Y. Sun: “Precision patterning of PDMS membranes and applications”, *J. Micromech. Microeng.* **18**, p.037004 (2008).
- [29] S.Y. Lee, H.W. Tung, W.C. Chen and W. Fang: “Thermal actuated solid tunable lens”, *IEEE Phot. Tech. Lett.* **18**, p.2191 (2006).
- [30] D. Chandra, S. Yanga and P.C. Lin: “Strain responsive concave and convex microlens arrays”, *Appl. Phys. Lett.* **91**, p.251912 (2007).
- [31] S. Grilli, V. Vespini and P. Ferraro: “Surface-Charge Lithography for Direct PDMS Micro-Patterning”, *Langmuir* **24**, p.13262 (2008).
- [32] M. Yamada, N. Nada, M. Saitoh, K. Watanabe: “First-order quasi-phase matched LiNbO₃ waveguide periodically poled by applying an external

- field for efficient blue second-harmonic generation”, *Appl. Phys. Lett.* **62**, p.435 (1993).
- [33] S. Grilli, M. Paturzo, L. Miccio, P. Ferraro: “In situ investigation of periodic poling in congruent LiNbO₃ by quantitative interference microscopy”, *Meas. Sci. Technol.* **19**, p.074008 (2008).
- [34] S. Grilli, P. Ferraro, M. Paturzo, D. Alfieri and P. De Natale: “In situ visualization, monitoring and analysis of electric field domain reversal process in ferroelectric crystals by digital holography”, *Opt. Exp.* **12**, p.1832–42 (2004).
- [35] E.M. Bourim, C.-W. Moon, S.-W. Lee, I.K. Yoo: “Investigation of pyroelectric electron emission from monodomain lithium niobate single crystals” *Phys. B: Condens. Matter* **383**, p.171 (2006).
- [36] M.G. Lippmann, *Ann. Chim. Phys.* **5**, p.494 (1875).
- [37] E. Colgate and H. Matsumoto: “An investigation of electrowetting-based microactuation”, *J. Vac. Sci. Technol. A* **8**, p.3625 (1990).
- [38] F. Mugele and J.-C. Baret: “Electrowetting: from basics to applications”, *J. Phys.: Condens. Matter* **17**, p.R705 (2005).
- [39] **F. Merola**, M. Paturzo, S. Coppola, V. Vespini and P. Ferraro: “Self-patterning of a polydimethylsiloxane microlens array on functionalized substrates and characterization by digital holography”, *J. Micromech. Microeng.* **19**, p.125006 (5pp) (2009).
- [40] S. Grilli: *Ferroelectric domain engineering and characterization for photonic applications*, Doctoral Thesis in Physics, Royal Institute of Technology, Stockholm, Sweden (2006).
- [41] W.K. Burns, W. McElhanon, L. Goldberg: “Second harmonic generation in field poled, quasi-phase-matched, bulk LiNbO₃”, *IEEE Photon. Technol. Lett.* **6**, p.252 (1994).
- [42] V. Bermúdez, L. Huang, D. Hui, S. Field, E. Dieguez: “Role of stoichiometric point defect in electric-field-poling lithium niobate”, *Appl. Phys. A* **70**, p.591 (2000).

- [43] L.E. Myers et al.: “Quasi-phase-matched optical parametric oscillators in bulk periodically poled LiNbO₃”, *J. Opt. Soc. Am. B* **12**, p.2102 (1995).
- [44] K. Nassau and H.J. Levinstein: “Ferroelectric behaviour of lithium niobate”, *Appl. Phys. Lett.* **7**, p.69 (1965).
- [45] V. Pruneri, J. Webjörn, P.St.J. Russell, J.R.M. Barr, D.C. Hanna: “Intracavity second harmonic generation of 0.532 μm in bulk periodically poled lithium niobate”, *Opt. Commun.* **116**, p.159 (1995).
- [46] V. Gopalan, Q.X. Jia, T.E. Mitchell: “In situ video observation of 180° domain kinetics in congruent LiNbO₃ crystals”, *Appl. Phys. Lett.* **75**, p.2482 (1999).

General conclusions

In this work different optical properties of lithium niobate compound have been studied and exploited for applications in diverse specific areas of interest, including waveguiding, microscopy imaging and microfluidics.

The work tries on one hand to give a contribution to the deep understanding of some well known phenomena, on the other hand to present novel results either in respect to precedent works or for the novelty of the phenomenon itself.

The preliminary nonlinear characterization, carried out by means of the Maker's fringes technique taking advantage of the second harmonic generation of the medium, has put in evidence the reason why lithium niobate is one of the most used materials for electro-optic devices: a very large value of the second order susceptibility tensor elements (at least one order of magnitude larger than that of quartz, taken as reference), and consequently a large value of the electro-optic coefficients of the material.

This result is very important because the electro-optic effect has been widely exploited for the applications of this crystal.

The applications of lithium niobate, as said many times, are innumerable, but in this thesis I have tried to focus the attention on three particular applications, each of them being interesting for a different reason. Digital holography has been largely employed as characterizing technique in each experiment, as it proved to be very suitable for such purpose, thanks to the flexibility of the numerical reconstruction process.

The first application is the enhancement of resolution in digital holographic microscopy, achieved by means of a bi-dimensional lithium niobate grating. In

fact, super-resolution can be obtained by adopting a diffraction grating that allows one to increase the effective numerical aperture of the optical system. Up to now the proof of principle had been demonstrated only in the one-dimensional case, limiting the resolution improvement to one single direction. In this case a step forward has been presented, demonstrating that the improvement is possible in two dimensions, adopting a lithium niobate diffraction grating having a hexagonal geometry able to increase the numerical aperture along three different directions (i.e. the three directions typical of the hexagonal geometry).

Furthermore, there are two important new aspects in this approach. Firstly, a dynamic phase grating obtained by electro-optic effect has been adopted: the diffraction efficiency can be tuned (simply by varying the applied voltage) allowing one to optimize the recording process of the digital holograms. Moreover, by appropriate handling of the transmission function of the numerical grating in the reconstruction algorithm, it has been possible to further improve the signal/noise ratio in the final super-resolved image.

A second application concerns an accurate amplitude and phase analysis of the photorefractive bright soliton formation process inside an undoped lithium niobate crystal, made possible by the interferometric digital holographic technique.

Thanks to this technique it has been possible to study the optical beam profile at the exit face of the crystal both in a stationary and time evolving situation, discerning, with the analysis of the phase, when and in which writing conditions the solitonic regime was actually achieved, while from an intensity analysis it was not always clear. The long time behavior of the waveguide has been also investigated, in order to estimate the time the solitonic regime was preserved. This time can last up to a couple of months simply keeping the sample in dark, but much longer (almost to infinity) if fixing techniques are used. Moreover, the phase analysis has enabled to monitor and quantify the changes in the refractive

index of the medium and so to characterize the type of solitonic waveguide formed in the diverse situations.

The possible application of solitons in waveguiding is evident, as the soliton shape of the beam can be perfectly symmetrical. Furthermore, being the refractive profile not depending on any physical-chemical process, while being self-written by a undiffracting light beam, it is optimized for single-mode propagation, low dispersion and low losses, and the required writing powers are very low (of the order of μW). Finally, the process is completely reversible, simply by applying an electric field in the opposite direction of that used during the writing procedure.

At the moment are under study the possible interactions among several solitons and the possibility of generating different paths inside the medium.

The last application of the material discussed in this thesis is probably the most amazing: a periodically poled lithium niobate crystal with reversed hexagonal domains has been used as substrate for the fabrication of polymeric microlens arrays through the thermal self-patterning of Polydimethylsiloxane (PDMS) films. This is an electrode-less, quick and relatively simple fabrication technique exploiting the pyroelectric effect at the crystal-polymer interface.

A careful optical analysis of the fabricated microlenses has been performed by means of digital holography, allowing to determine the focal length of each single lens. Three different samples have been fabricated, each with microlenses of micrometric size (diameters of about $100\ \mu\text{m}$) but with little different shape (i.e. curvature). The measured focal lengths range from about $300\ \mu\text{m}$ up to $1000\ \mu\text{m}$, with differences of few microns within the same sample.

One sample has been also detached from the lithium niobate substrate before characterizing it, and it seems that the process of peeling did not cause appreciable deformations in the lenses' shape or aberrations. This could be very important for a realistic application of polymeric microlens arrays.

My research in this field is now being directed to an integration of polymers with other materials such as liquid crystals, as a suitable amount of a liquid

mixed in the polymer host can improve not only the lens flexibility but also the lens performance.

List of abbreviations

Chapter I :

LN = Lithium Niobate

SHG = Second Harmonic Generation

EO = Electro-Optic

SLN = Stoichiometric LN

SFG = Sum Frequency Generation

DFG = Difference Frequency Generation

OR = Optical Rectification

OPA = Optical Parametric Amplification

SH = Second Harmonic

Chapter II :

DH = Digital Holography

CCD = Charge Coupled Device

DHM = Digital Holographic Microscopy

NA = Numerical Aperture

ITO = Indium Tin Oxide

RP = Reconstruction Pixel

Chapter III :

PR = Photorefractive

OW = Optical Waveguide

FWHM = Full Width at Half Maximum

SBN = Strontium Barium Niobate

BTO = Bismuth Titanate

Chapter IV :

PDMS = Polydimethylsiloxane

PEW = Pyro Electro Wetting

PMMA = Polymethylmethacrylate

EFP = Electric Field Poling

SEM = Scanning Electron Microscope

PPLN = Periodically Poled Lithium Niobate

RPM = Revolutions Per Minute

QPM = Quasi Phase Matching

SG = Signal Generator

HVA = High Voltage Amplifier

HVP = High Voltage Probe

Acknowledgements

First of all I would like to thank my supervisors, Prof. Pasqualino Maddalena and Dr. Pietro Ferraro, for their useful suggestions and the constant guide during the whole doctorate course.

Of course I have to thank my lab colleagues Sara Coppola, Simonetta Grilli, Lisa Miccio, Melania Paturzo, Veronica Vespini, Sergio De Nicola and Andrea Finizio: without their help and contribution a great part of the results presented here would have never been obtained.

Last but not least, I'm very grateful to the PhD coordinator Prof. Lorenzo Marrucci. His management of the doctorate course has been friendly and stimulating for our work as PhD students.